UNIVERSITY OF OKLAHOMA

GRADUATE COLLEGE

EFFECTS OF NON-EQUILIBRIUM CHARGE CARRIERS ON PHOTOCATALYTIC REACTIONS OVER HYBRID PLASMONIC CATALYST

A DISSERTATION

SUBMITTED TO THE GRADUATE FACULTY

in partial fulfillment of the requirements for the

Degree of

DOCTOR OF PHILOSOPHY

By

THI THUY TIEN LE

Norman, Oklahoma

2023

Downloaded from SHAREOK. Persistent Handle URL: https://hdl.handle.net/11244/338733

EFFECTS OF NON-EQUILIBRIUM CHARGE CARRIERS ON PHOTOCATALYTIC REACTIONS OVER HYBRID PLASMONIC CATALYST

A DISSERTATION APPROVED FOR THE

SCHOOL OF SUSTAINABLE CHEMICAL, BIOLOGICAL AND MATERIALS ENGINEERING

BY THE COMMITTEE CONSISTING OF

Dr. Bin Wang, Chair

Dr. Yihan Shao

Dr. Daniel Resasco

Dr. Steven Crossley

Dr. Dimitrios Papavassiliou

© Copyright by THI THUY TIEN LE 2023

All Rights Reserved.

This dissertation is dedicated to my parents, my husband, and my son.

(Dành tặng ba mẹ tôi, Lê Quang Tín - Trần Thị Lý, và gia đình nhỏ của tôi)

Acknowledgements

I would like to thank the following people for their support in completing this dissertation.

First and foremost, I would like to extend my deepest gratitude to my advisor, Dr. Bin Wang, for his continuous support for my family and me during my PhD study. I am extremely grateful for his invaluable advice for work as well as in daily life. I am thankful for his understanding of the challenges of an international graduate student, especially during the COVID-19 pandemic. I am particularly grateful for his tremendous flexibility, support, and understanding of my family situation, allowing me to work and complete various collaborative research projects. I cannot make it that far without his sharing, mentorship, and encouragement. I am so honored to be part of his Computational Materials and Chemistry Group (OUCMC Group).

I also could not have undertaken this journey without the support from my defense committee, who generously provided knowledge and expertise. I would like to extend my sincere thanks to Dr. Daniel Resasco for his immense knowledge and tremendous enthusiasm for heterogeneous catalysis and for guiding me to be a critical researcher. I am also thankful to Dr. Steven Crossley for his insightful comments and suggestions in the group meetings. I am thankful to Dr. Yihan Shao for his support and fruitful collaboration on DFT theoretical studies. Special thanks to Dr. Dimitrios Papavassiliou for being on my committee and providing support throughout my study. Many thanks to Dr. Lance Lobban for his encouragement and kind support.

I would like to recognize the fruitful collaborations with Dr. Pedro Camargo at the University of Helsinki, Dr. Marimuthu Andiappan at the Oklahoma State University, Dr. Wenyu Huang and Dr. Jiaqi Yu at the Iowa State University, and Dr. Phillip Christopher at the University of California, Santa Barbara.

I would like to acknowledge the assistance of Dr. Reda Bababrik, Dr. Tong Mou, Dr. Yu Yan, and Dr. Vy Nguyen in my first year with the OUCMC group. I had the pleasure of working with Dr. Taha Salavati-fard, and enjoyed the technical discussion with other OUCMC group members, including Ishaq, Quy, Jacob, Zaheer, and Thy. I am also thankful to my colleagues at OU: Nilson, Gengnan, Malli, Nabihan, Alejandra, Ana, Elton, Ismaeel, Nut, Erich. I would like to extend my sincere thanks to current and past members of OU Catalysis Group. It is their kind support in the research and outside of work that has made my life at OU an unforgettable time.

I would be remiss in not mentioning my Vietnamese and other international friends: chi Vi, anh Vinh, be Thao, anh Tuan, chi Tram, anh Tien, chi Nhung, anh Thang, chi Linh, chi Oanh, Thanh, Phat, chi Vinh, chi Ngoc, 6 anh em group (Thao, Lan, Quoc, Huy), Onyi Igwe, and Mrs. Mary Lawrence. Special thanks to chi Huong, chi Hieu, chi Quy, and chi Thuy for being there when I need the most. Their kindness, understanding, and encourage make me feel cheerful and less lonely when I am far from home.

My appreciation also goes to Terri, Rett, Nicole, Jennifer, and Madena for their support with paperwork, and making my research proceed smoothly.

I would like to acknowledge the U.S. Department of Energy, Basic Energy Sciences, Chemical Sciences, Geosciences, and Biosciences Division, Condensed Phase and Interfacial Molecular Science (Grant DE-SC0020300) for supporting this work. Many thanks to the OU Supercomputing Center for Education & Research (OSCER) and the National Energy Research Scientific Computing Center (NERSC), and the University of Oklahoma for the opportunity to study and perform this research.

Finally, I would like to express my gratitude to my family for their unwavering support and sacrifices. Special thanks to my family in-law for their encouragement and understanding. I

would not have been where I am today without them. I am extremely grateful to my husband Han, who motivated me to pursue higher education in the first place, for his unconditional love and always being by my side. I would never say thank you enough to our little boy, Gift (Quan), for coming and lighting up my life. This endeavor would not have been possible without all of you.

Table of Contents

Acknowledgements v

List of Tables xi

List of Figures xii

List of Publications xix

List of Presentations xx

Abstract xxi

Chapter 1: Introduction 1

1.1. Hybrid plasmonic catalyst 1

1.2. Scope and Outline 6

Chapter 2: Computational method 9

2.1. Density-Functional Theory 9

The Kohn-Sham (KS) Method 10

Density of State 12

Absorption coefficient 14

2.2. Excited states calculation using linear expansion ΔSCF 14

Chapter 3: The hybrid plasmonic catalyst between the plasmonic metal and the semiconductor Cu_2O 18

3.1. Plasmonic Energetic Electrons Drive CO_2 Reduction on the pristine Cu_2O surface 18

Abstract 18

Introduction 19

Computational Method 21

Results and discussion 23

Conclusions 35

Acknowledgements 35

3.2. Plasmonic Energetic Electrons Drive CO_2 Reduction on Defected Cu_2O 36

Abstract 36

Introduction 36

Results and discussion 39

Conclusion 51

Computational method 52

Acknowledgement 55

Chapter 4: The hybrid plasmonic catalyst between the plasmonic metal and zeolite 56

4.1. A first-principles study of the interaction between molecules and Lewis acid zeolites manipulated by injection of energized charge 56

Abstract 56

Introduction 57

Computational Method 60

Results and discussion 62

Conclusion 74

Acknowledgements 75

4.2. Epoxidation reaction on TS-1 76

Introduction 76

Results and discussion 77

Chapter 5: Local enviroment effect induced by solvent on the hybrid plasmonic catalyst 78

Abstract 78

Introduction 78

Computational method 80

Results and discussion 81

Conclusion 88

Chapter 6: Summary and Future Directions 89

6.1 Dissertation Summary 89

6.2. Future directions 91

Appendix A1: Supporting information for Chapter 3.1 93

Appendix A2: Supporting information for Chapter 3.2 99

Appendix A3: Supporting information for Chapter 4.1 104

Appendix A4: Supporting Information for Chapter 5 109

References 112

List of Tables

Table 2.1 Example of center and band width of the molecular orbital: The center and bandwidth of LUMO shown in Figure 2.2. 13

Table A1.1 The difference of the Bader charge between the excited states (which has only an added electron into unoccupied KS orbital) with the ground state 96

Table A1.2 The difference of the Bader charge between the excited states (which has an added electron into unoccupied KS orbital and a hole at Fermi level) with the ground state 97

Table A3.1 The mean square deviation from regular tetrahedron angle (O-M-O angle) of M-BEA at the ground state, at excited states with an energized electron and excited states with an energized hole. 107

Table A3.2 The adsorption energy of NH_3 on the open site of Sn-BEA ($(OSi)_3SnOH$) under the effect of the energized electron or hole. 107

Table A3.3 Bader charge analysis on Sn and OH groups of Sn-BEA shown in Figure 4.1.5 at the ground state, at excited states with an energized electron and excited states with an energized hole. 107

Table A3.4 HSE06 calculation results (unit: eV) 108

Table A4.1 The adsorption energy of NH_3 on the Ru-doped Cu surface ($RuCu_{83}$) vs Cu surface (Cu_{84}). Unit: eV 111

Table A4.2 The excitation energy of an electron from Fermi level to LUMO of NH_3 of the Cu surface (Cu_{84}). Unit: eV 111

List of Figures

Figure 1.1 Schematic diagram of local surface plasmon resonance due to a higher frequency external field (reproduced from reference [2]). 1

Figure 1.2 Mechanism of plasmon-mediated bond activation(reproduced from reference [8]) 2

Figure 1.3 Dielectric function of noble and transition metals. (a) The real part (b) The imaginary part of the dielectric function (reproduced from reference [8]) 4

Figure 2.1 Example of pDOS on adsorbed molecule using VASP: the pDOS on CO when CO adsorbed on Pt surface. 12

Figure 2.2 Example of pDOS on particular molecular orbitals using GPAW: the pDOS on LUMO of CO when it adsorbed on Pt or Pd surface. 13

Figure 2.3 Example of absorption coefficient of CO adsorbed on Pt. Unit: cm^{-1} 14

Figure 2.4 The excitation energy calculated based on vdW-DF or PBE as exchange-correlation functional using GPAW. 17

Figure 3.1.1 The energy diagram of CO_2 dissociation at the ground state calculated in PBE+U calculations with and without spin polarization and by spin-polarized HSE06 calculation. The blue, gray and red balls denote Cu, C and O atoms respectively. 24

Figure 3.1.2 The projected density of state (PDOS) of CO_2 adsorbed on Cu_2O and the total DOS calculated by PBE+U (a) and HSE06 (c). The zoom in areas from Fermi level to 2.5eV of PDOS are shown in b) for PBE+U calculations and in d) for HSE06 calculations. The partial charge of CO_2 adsorbed on Cu_2O (111) surface at initial state: (e) partial charge from 3.0 to 4.0 eV above Fermi level; and (f) partial charge from 0 to 2.5 eV above Fermi level (based on PBE+U calculation) 27

Figure 3.1.3 Ground state and excited state energies (eV) along reaction pathway obtained using the PBE+U calculations combined with the ΔSCF approach. Each colored line represents a reaction profile mapping from the initial state to the final state by manipulating electronic occupation at different electronic states above the Fermi level. Groups of I, II, III correspond to

the groups of states shown in the DOS calculations in Figure 3.2. The excitation at the initial, transition and final states are labelled for some of the vertical transitions. 28

Figure 3.1.4 Ground state and excited state energies (eV) along reaction pathway predicted by the HSE06 functional combined with the ΔSCF approach. Each colored line represents a reaction profile mapping from the initial state to the final state by manipulating electronic occupation at different electronic states above the Fermi level. Groups of I, II, III correspond to the groups of states shown in the density of states calculations. 30

Figure 3.1.5 The energy difference of the total energies between the system with an added electron and a hole at Fermi level of Cu_2O and the system with an added electron only (PBE+U). 31

Figure 3.1.6 Possible charge transfer mechanism. The work function of Al, Ag, and Au taken from literatures [55, 57, 58] 34

Figure 3.2.1 The CO_2 dissociation on 111-Ores-Ovac. (**A**) Configurations of the initial state (image 0), the transition state (image 4), the final state (image 9), and their corresponding schematic sketches. The two oxygen in CO_2 is labeled as a and b for distinguishment. (**B**) Ground-state energy profile calculated over ten images (indexed 0 to 9) with VASP. The C-O^a bond length is marked in green (Unit Å). (**C**) Energy profile at excited states, when an electron is added into the LUMO of CO_2 (blue, E0-CO_2), the first available antibonding state of C-O^a bond (gray, E0-CO^a) or C-O^b bond (orange, E0-CO^b), which are compared with the ground state (black dashed, G0); all calculated by GPAW. The magenta solid line (E0-lumo+1) is included to illustrate the case when the electron is added into the LUMO+1 of CO_2 from image 5 to 9. 39

Figure 3.2.2 The CO_2 dissociation on 111-VCu-Ovac. (A) Configuration of the initial state (image 0), transition state (image 5), final state (image 9) and their corresponding schematic sketch. **(B)** Energy profile at the ground-state calculated in ten images (indexed 0 to 9) with VASP. The C-O^a bond length is marked in green (Unit Å) **(C)** Energy profiles at excited states when an electron is added into the LUMO of CO_2 (blue, E0-CO_2), the first available antibonding state of C-O^a bond (gray, E0-CO^a) or C-O^b bond (orange, E0-CO^b), which are compared with the ground state (red dashed, G0); all calculated by GPAW. The magenta solid line (E0-lumo+1) is included to illustrate the case when the electron is added into the LUMO+1 of CO_2 from image 5 to 9. .. 41

Figure 3.2.3 The CO_2 dissociation on 110-CuO-Ovac. (A) Configuration of the initial state (image 0), the transition state (image d) and the final state (image 9) with their corresponding schematic sketch **(B)** Ground-state energy profile calculated by VASP. The initially selected images (0-9) were further expanded between image 4 and 5 to form additional eight images (a-h). The C-O^a bond length is marked in green (Unit Å) **(C)** Energy profile at excited states when an electron is added into the LUMO of CO_2 (blue, E0-CO_2), the first available antibonding state of C-O^a bond (gray, E0-CO^a) or C-O^b bond (orange, E0-CO^b), which are compared with the ground state (blue dashed, G0); all calculated by GPAW. The magenta solid line (E0-lumo+1) is included to illustrate the case when the electron is added into the LUMO+1 of CO_2 from image d to 9... 42

Figure 3.2.4 Projected density of states onto the CO_2 molecular orbitals at the ground level. The pDOS of CO_2 at the initial states (left) and the transition states (right) on **(A)** (111-Ores-Ovac), **(B)** (111-VCu-Ovac), and **(C)** (110-CuO-Ovac) surface..... 44

Figure 3.2.5 Energy diagram of oxygen vacancy formation by hydrogenation on Cu_2O. (**A**) (111-Ores) and (111-VCu); **(B)** (110-CuO) and (110-CuOH). 49

Figure 4.1.1 Calculations to explore main factors for molecular adsorption. (a) Plot of the adsorption energy of NH_3 on M-BEA together with IP, EA, Bandgap. (b) Plot of the adsorption energy of NH_3 on M-BEA with charge density difference before and after NH_3 adsorption of metal – q(M), of metal and 4 oxygen nearby - q(MO_4) and of NH_3 - q(NH_3). (c) Charge redistribution at the interface between the Lewis acid (M-BEA) and NH_3 in z direction. (d) The illustration of the charge redistribution. The blue, red and white balls denote Si, O and H atoms respectively. The cyan and yellow colors denote the withdrawing and accepting of electrons. 64

Figure 4.1.2 Adsorption of NH_3 in M-BEA with an additional electron or a hole. (a) The heat of adsorption of NH_3 on neutral M-BEA (white) compared with values with an added electron (red) and with one removed electron (blue). The relationship between the change of heat of adsorption and the electron localization on metal when (b) one electron is added into M-BEA, and (c) one electron is removed from M-BEA. 66

Figure 4.1.3 PDOS of M-BEA on metal (pink) and on SiO_2 framework (brown) for a) Si-BEA b) Ti-BEA c) Zr-BEA d) Sn-BEA..... 68

Figure 4.1.4 Charge redistribution at the interface between NH_3 and M-BEA neutral (black), M-BEA with 1 added electron (red), M-BEA with 1 removed electron (blue) for a) Si-BEA b) Ti-BEA c) Zr-BEA d) Sn-BEA. The blue, red and white balls denote Si, O and H atoms respectively. 71

Figure 4.1.5 a) The total DOS and the PDOS of Sn of the open site configuration shown in (b), the charge redistribution when NH_3 adsorbed on the open site of Sn-BEA (c). The grey, blue, red and white balls denote Zn, Si, O and H atoms respectively. 72

Figure 4.1.6 Electron excitation to the conduction band edge and mid-gap states in Si-BEA and Sn-BEA. The work function of pure silica form of BEA is obtained from the work function of SiO_2 polymorph of ZSM-5[124], and the work function of Au is taken from literature[57]. Units are eV. . 74

Figure 4.2.1 Illustration of different doped level of Ti in TS-1 76

Figure 4.2.2 Energy diagram of propylene epoxidation at the ground state and the excited state on TS-1..... 77

Figure 5.1 The effect of H_2O. The excitation energy to excite electron from HOMO of NH_3 to Fermi level (blue), excite electron from Fermi level to LUMO of NH_3 (red), and the HOMO-LUMO gap (black). Optimized configuration of NH_3 only (Base case, black), NH_3 with H_2O (blue) on $RuCu_{83}$. 82

Figure 5.2 Density of states projected on adsorbed NH_3 when only NH_3 adsorbed on $RuCu_{83}$ (and NH_3 with H_2O. The center of the HOMO and LUMO of NH_3 are shown above the main peak. 86

Figure 5.3 The effect of CH_3OH. The excitation energy to excite electron from HOMO of NH_3 to Fermi level (blue), excite electron from Fermi level to LUMO of NH_3 (red), and the HOMO-LUMO gap (black). Optimized configuration of NH_3 only (Base case, black), NH_3 with CH_3OH (Green) on $RuCu_{83}$ are shown in the top channel. 87

Figure 5.4 The effect of C_6H_5OH. The excitation energy to excite electron from HOMO of NH_3 to Fermi level (blue), excite electron from Fermi level to LUMO of NH_3 (red), and the HOMO-

LUMO gap (black). Optimized configuration of NH_3 only (Base case, black), NH_3 with CH_3OH (Green) on $RuCu_{83}$ are shown in the top channel. 87

Figure 5.5 The changing of the excitation energy to excite electron from Fermi level to LUMO of NH_3 and the Ru-N bond length as the number of H_2O/C_6H_5OH molecules increased..... 88

Figure A1.1 The NEB calculation results (A) and the represented configurations along reaction pathway after running about 1,000 steps (B-H). Based on NEB, the transition state and activation energy were calculated further by applying the dimmer method. We also tried to calculate the NEB calculation for breaking the C-O2 bond with O2 remains at unsaturated Cu and the C-O1 travelling to the nearby unsaturated Cu. However, the calculation cannot be converged. 93

Figure A1.2 Crystal orbital Hamilton population (COHP) [140] of absorbed CO_2 on Cu_2O (111) surface at the initial state..... 93

Figure A1.3 Ground state and excited state energies (eV) along reaction pathway predicted by the PBE+U functional combined with the ΔSCF approach. Each colored line represents a reaction profile mapping from the initial state to the final state by manipulating electronic occupation at different electronic states above the Fermi level and a hole at Fermi level..... 94

Figure A1.4 a) The absorption coefficient of Cu_2O (black) and Cu_2O with adsorbed CO_2 (blue); b) The difference of absorption coefficient between the two structures with and without adsorbed CO_2 on Cu_2O. Both calculations were performed using the HSE06 functional. For the Cu_2O result plotted in the figure, we removed the CO_2 while keeping the other atoms fixed at their positions. 94

Figure A1.5 The charge density difference between the excited states (which has an added electron into unoccupied KS orbital and a hole at Fermi level) with the ground state. Cyan color represents for removed electron and yellow color represents for added electron. An isosurface value of 0.00067 e/$Å^3$ is used. 95

Figure A2.1 Optical absorption coefficient of the (111-Ores) surface with and without oxygen vacancy. Unit: cm^{-1}. 99

Figure A2.2 Absorption coefficient of the (111-VCu) surface with and without oxygen vacancy. Unit: cm^{-1}. 99

Figure A2.3 Absorption coefficient of the (110-CuO) surface with and without oxygen vacancy. Unit: cm^{-1}. 100

Figure A2.4 The model of the oxygen-deficient surfaces of Cu_2O. The blue and red balls denote for Cu and O atoms respectively. 100

Figure A2.5 The ground- and excited-state energy profile of the oxygen vacancy formation step when one electron is added into the LUMO of H_2O by GPAW. 101

Figure A2.6 Scheme to illustrate how photo-excited electron is modelled in our study. The model is shown in the red rectangle. **(A)** The model of the neutral system. **(B)** The model of the charged system (one additional electron is added into the neutral system) when an electron is added into the project LUMO of the adsorbed molecule (green area). **(C)** The model of the charged system when an electron is added into the lowest unoccupied states of the system (green area). 101

Figure A2.7 DFT results when one additional electron is added into the lowest unoccupied states of the charged system by VASP. (A) The intrinsic activation energy at the ground- and excited state of the oxygen vacancy formation step. **(B)** The intrinsic activation energy at the ground- and excited-state of the CO_2 dissociation step. **(C)** The charge density difference projected on CO_2 and under-coordinate Cu atoms at the transition state between the ground- and excited-PES. **(D)** The relationship between charge density localized on CO_2 at the initial state and the transition state, and the C-O bond length at the transition state. 102

Figure A2.8 The surface energy of Cu_2O. The O-terminated Cu_2O (111) surface (111-Ores, black), the O-terminated Cu_2O (111) surface with Cu vacancy (111-VCu, red), the mixed CuO-terminated (110) surface (110-CuO, blue) and the Cu-terminated (110) surface (110-Cu, orange). 103

Figure A3.1 Relationship between NH_3 and pyridine adsorption energy on M-BEA. 104

Figure A3.2 Relationship between NH_3 adsorption energy on M-BEA with the mean square deviation from regular tetrahedron angle (O-M-O angle) (theta, θ), the volume of tetrahedral ($VMO4$) and the average bond M-O bond length with the four oxygen nearby metal center. ... 104

Figure A3.3 PDOS of adsorbed NH_3 (green) on M-BEA (black): a) Si-BEA b) Ti-BEA c) Zr-BEA d) Sn-BEA..... 105

Figure A3.4 (duplicated from Figure 4 of the main text): Charge redistribution at the interface between the Lewis acid (M-BEA) and NH_3 in the z direction at the ground state (back color), at excited states with an energized electron (red color) and at excited states with an energized hole (blue color).. 106

Figure A4.1 The changing of wavefunction and the energy difference between core level of Cu 1s with respect to Fermi level as the number of H_2O/C_6H_5OH molecules increased 109

Figure A4.2 Density of states projected on adsorbed NH_3 when it is surrounding by C_6H_5OH. The center of the HOMO and LUMO of NH_3 are shown above the main peak. 110

Figure A4.3 Comparison of the HOMO-LUMO gap when it is directly calculated via GPAW versus when it is indirectly calculated as a sum of E_{elec} and E_{hole}..... 111

List of Publications

1. **Le, T.**; Salavati-fard, T.; Wang, B.; Plasmonic Energetic Electrons Drive CO_2 Reduction on Defective Cu_2O, *ACS Catalysis*, 2023, 13, 9, 6328–6337
2. Peiris, E., Hanauer, S., **Le, T.**, Wang, J., Salavati-fard, T., Brasseur, P., Formo, E. V., Wang, B., Camargo, P. H. C., Controlling Selectivity in Plasmonic Catalysis: Switching Reaction Pathway from Hydrogenation to Homocoupling Under Visible Light Irradiation, *Angew. Chem. Int. Ed*. 2023, 62, e202216398; *Angew. Chem.* 2023, 135, e202216398.
3. **Le, T.**; Shao, Y.; Wang, B.; Plasmon-Induced CO_2 Conversion on Al@Cu_2O: A DFT Study, *J. Phys. Chem. C,* 2021, 125, 11, 6108–6115
4. **Le, T.**; Wang, B.; First-Principles Study of Interaction between Molecules and Lewis Acid Zeolites Manipulated by Injection of Energized Charge Carriers, *Ind. Eng. Chem. Res.,* 2021, 60, 39, 14124-14133
5. Ramakrishnan, S. B.; Tirumala, R. T. A.; Mohammadparast, F.; Mou, T.; **Le, T.**; Wang, B.; Andiappan, M.; Plasmonic photocatalysis, *Catalysis: Volume 33, The Royal Society of Chemistry*, 2021, Vol. 33, pp 38-86
6. Ramakrishnan, S. B., Mohammadparast, F., Dadgar, A. P., Mou, T., **Le, T.**, Wang, B., Jain, P. K., Andiappan, M.; Photoinduced Electron and Energy Transfer Pathways and Photocatalytic Mechanisms in Hybrid Plasmonic Photocatalysis, *Adv. Optical Mater*, 2021, 2101128
7. Yu,J., **Le,T.**, Jing,D., Stavitski,E., Hunter,N., Lalit,K., Leshchev,D., Resasco,D., Sargent,E., Wang,B., Huang,W., Coke-free catalyst design through kinetics balancing in dry reforming of methane (Submitted)

8. **Le, T.**, Wang, B., Local environment effect induced by solvent on the plasmonic catalysis (ready to be submitted)
9. **Le, T.**; Salavati-fard, T.; Wang, B.; Mechanistic insights into plasmonic photocatalysis from electronic structure calculations (ready to be submitted)

List of Presentations

1. "Photo-Excited Electrons Drive the CO_2 Reduction on Cu_2O", Poster presentation, *NAM28 Meeting*, Providence, Rhode Island, June 18-23, 2023
2. "Plasmon-Assisted Direct Charge Transfer Drives Surface Reactions", Oral presentation, *NAM28 Meeting*, Providence, Rhode Island, June 18-23, 2023
3. "Oxygen Vacancies and Hydroxyl Groups Drive Reduction of CO_2 on Cu_2O Via Photocatalytic Hydrogenation", Poster presentation, *NAM27 Meeting,* New York, May 22-27, 2022
4. "Plasmon-induced CO_2 conversion on $Al@Cu_2O$: A DFT study", Oral presentation, *2021 AIChE Annual Meeting*, Boston, November 7-11, 2021
5. "Tuning the interaction between molecules with Lewis acid zeolite by injection of energized carriers", Poster presentation, *2021 AIChE Annual Meeting*, Boston, November 7-11, 2021
6. "Plasmon-induced CO_2 conversion on $Al@Cu_2O$: A DFT study", Oral presentation (virtual), *ACS Spring 2021*, April 5-30, 2021
7. "Tuning the interaction between molecules with Lewis acid zeolite by energized carriers", Oral presentation (virtual), *GPCS Fall Virtual Symposium 2021*
8. "Plasmon-induced CO_2 Conversion on $Al@Cu_2O$: a DFT approach", Oral presentation (virtual), *GPCS Fall 2020 Online Symposium*

Abstract

Fascinated by how nature can directly transfer solar energy into a chemical reaction, several studies on the photocatalyst have been performed and hoped to imitate nature's process to achieve similar conversion. Unfortunately, the ultralow efficiencies of the photocatalyst largely remained. Plasmonic catalyst based on the local surface plasmon resonance of noble metal nanoparticles is then investigated to increase the utilization of the visible wavelength and tailor the reaction selectivity toward a more sustainable future. Particularly, the hybrid plasmonic catalyst between noble metal and other components received a lot of interest due to the prolonged lifetime of the charge carriers or the number of chemical reactions that can be activated. However, on the hybrid plasmonic photocatalyst, the mechanism of how non-equilibrium charge carriers induce reactions remains unclear, especially under the solvent effect. In this dissertation, it is attempted to give an understanding of how non-equilibrium electrons can facilitate reactions on the plasmonic hybrid of copper (I) oxide, a promising oxide in photocatalysis using visible light, and of zeolite, a unique micro porous oxide that has several applications in the energy and fuel field. While the former type, the hybrid between plasmonic nanoparticle and the semiconductor, is expected to extend the lifetime of charge carriers, the latter type is applicable to various reactions.

Using CO_2 conversion as the probe, we found that the non-equilibrium carriers do not change much the intrinsic activation energy of CO_2 dissociation on a Cu_2O pristine surface at the excited states compared to the ground state. In contrast, if the oxygen vacancies are introduced, the intrinsic barrier could be reduced at the ground state, and this remaining barrier could be further eliminated at the excited states because of the non-equilibrium electrons. The regeneration of oxygen vacancies is feasible via the hydrogenation process with low required energy and is not affected by the presence of the non-equilibrium charge carriers.

For the hybrid catalyst between a plasmonic metal and zeolite, it is revealed that the non-equilibrium charge carriers can alter the interaction between ammonia and the Lewis acid site of Beta zeolite. The effect is more significant when there are mid-gap states induced Sn or Ti doped into Si-BEA framework. Apart from the effect on the heat adsorption, it is found that if the doped concentration of Ti into zeolite increases, the intrinsic activation energy of the propylene epoxidation also can be reduced due to the higher population of the non-equilibrium electrons to induce reactions. These studies provide the opportunity to use highly energetic charge carriers, generated in plasmonic metal, to tune the zeolite activity for acid-catalyzed reactions.

Finally, we explored the effect of solvent on the excitation energy and found that the H-bond between solvents and reactants could interfere with the interfacial charge transfer process. Notably, the H-bond between solvent and ammonia can prohibit the excitation energy to trigger an electron from the Fermi level to LUMO of ammonia. At the same time, it can reduce the excitation energy to excite an electron from molecular HOMO to the Fermi level. The stronger acidity of the solvent, the more inhibition effect is observed for the transfer of electrons from the Fermi level to LUMO. In addition, we found that the H-bond also affects the HOMO-LUMO gap of the molecules, which directly influences the energy transfer between plasmonic metal and reactants. The findings of this dissertation could be a valuable guideline for hybrid plasmonic catalyst design for sustainable energy and chemical production.

Keywords: hybrid plasmonic catalyst, photocatalyst, CO_2 conversion, Cu_2O, zeolite, ammonia, solvent effect, excitation energy.

Chapter 1: Introduction

1.1. Hybrid plasmonic catalyst

Why plasmonic catalyst?

As the chemical field moves toward a more sustainable future, the process of utilizing renewable solar energy in chemical transformation has received a lot of interest.[1-5] To mimic the chemical reactions of nature, like plant leaves, photocatalytic materials based on semiconductors such as TiO_2 and ZnO was developed, and successfully set a foundation for several photocatalyst applications.[1, 6, 7] However, these conventional semiconductors usually have a bandgap larger than 3 eV, so UV light is primally utilized in these cases. Since UV light is only ~4% of solar radiation, the efficiency of conventional photocatalysts is low. Plasmonic photocatalyst is then applied to harvest the visible light - which is ~43% of solar radiation - to increase the efficiency of the photocatalyst.[1]

What is local surface plasmon resonance (LSPR)?

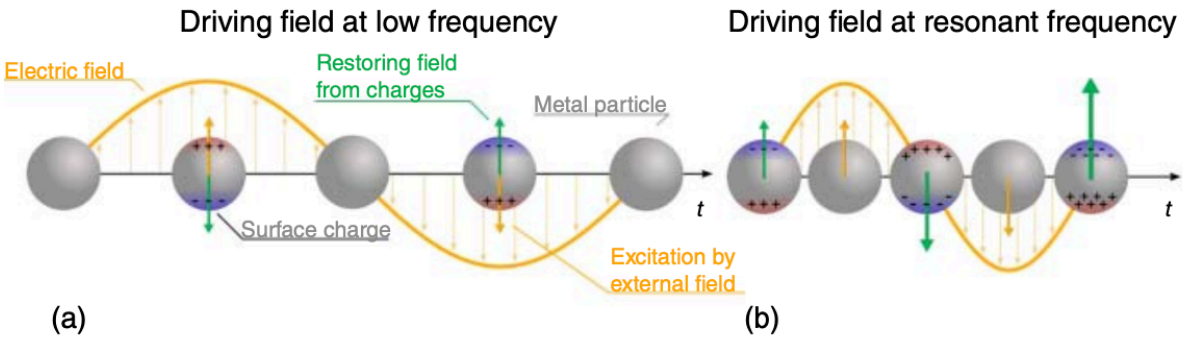


Figure 1.1 *Schematic diagram of local surface plasmon resonance due to a higher frequency external field (reproduced from reference [2]).*

The defining characteristic of plasmonic materials is their large number of mobile carriers. The typical case for this is a metal where the cloud of free electrons moves in a continuous manner following an external electric field. The electric field can then polarize charges and tend to drive free electrons out of the metal surface. At the same time, the Coulombic attraction between the nucleus and electrons tends to pull the electron cloud back to its initial position. The electrons move back and forth to balance with the oscillation of the external field. If the frequency of the external field is high enough (Figure 1.1), the charge oscillation inside the particle will oscillate in resonance with the external field, generating localized and intensified electric fields around the metal nanoparticle surface, namely local surface plasmon resonance (LSPR). The charge polarization inside the metal particle then does not cancel out but is amplified instead.[2] For the visible light, the LSPR can be established on the plasmonic metal nanoparticles since their size is smaller than the wavelength of light.

How plasmonic catalyst can induce reaction?

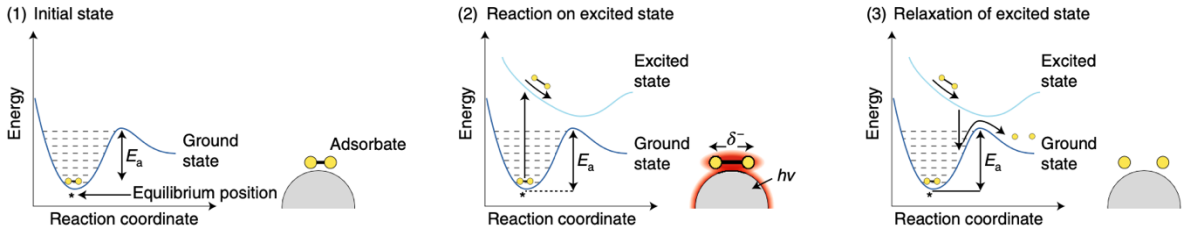


Figure 1.2 *Mechanism of plasmon-mediated bond activation(reproduced from reference [8])*

If the LSPR can dissipate the energy via non-radiative decay, the non-equilibrium charge carriers (electron-hole pairs) can be generated. These initially high-energy non-equilibrium electrons will quickly redistribute their energy via electron-electron scattering, forming the Fermi-Dirac distribution. These energy electrons are then further cooled down by interacting with phonon, resulting in the heating of the lattice. Finally, the energy is lost via transferring to the

surrounding metallic structrure.[3, 8] If there are available electron-accepting orbitals nearby, such as unoccupied orbitals of adsorbed molecules on the metal surface, the electrons with adequate energy can transfer to the adsorbate (the charge transfer mechanism), generate the transient negative ion, and induce chemical transformations.[1-3, 8] Then, the system can travel along the excited state potential energy surface to complete the reaction or decay to the ground state and complete the reaction at the ground level (Figure 1.2). In addition, the LSPR can decay and transfer energy to the molecule (the energy transfer mechanism). In this case, the system is neutral, and the excited molecule then can travel along the excited state or decay to complete the reaction. As a result, by targeting selective orbitals to populate, the plasmonic photocatalyst, in principle, can improve the selectivity of chemical reactions.[8]

The charge transfer process can occur via indirect or direct charge carrier injection. While the indirect charge transfer requires the following step to transfer non-equilibrium electron/hole to the environment after their excitation step, the direct charge transfer process refers to the event that the energy of the plasmon can trigger electron across the material interface to populate the orbitals of adsorbed molecules. Apart from the charge transfer process, there are other proposed mechanisms of plasmonic-mediated reaction, such as plasmon-induced resonance energy transfer (PIRET, due to the plasmonic near-field enhancement), the enhancement of the vibration, and thermal heating. Although the charge/energy transfer is concurrent with the heating, there are properties attributed to the light-driven reaction, such as the transition from linear to superlinear relationship instead of the exponential relationship between light intensity and reaction rate, the varied kinetic isotope effects (KIE) different from the thermal-driven reactions.[9] The shifting of selectivity,[10] or the greater reaction rate than the thermal reaction rate at the same surface

temperature can sometimes be used to recognize the light-driven processes in experimental photocatalytic systems.

Which metal can be plasmonic core?

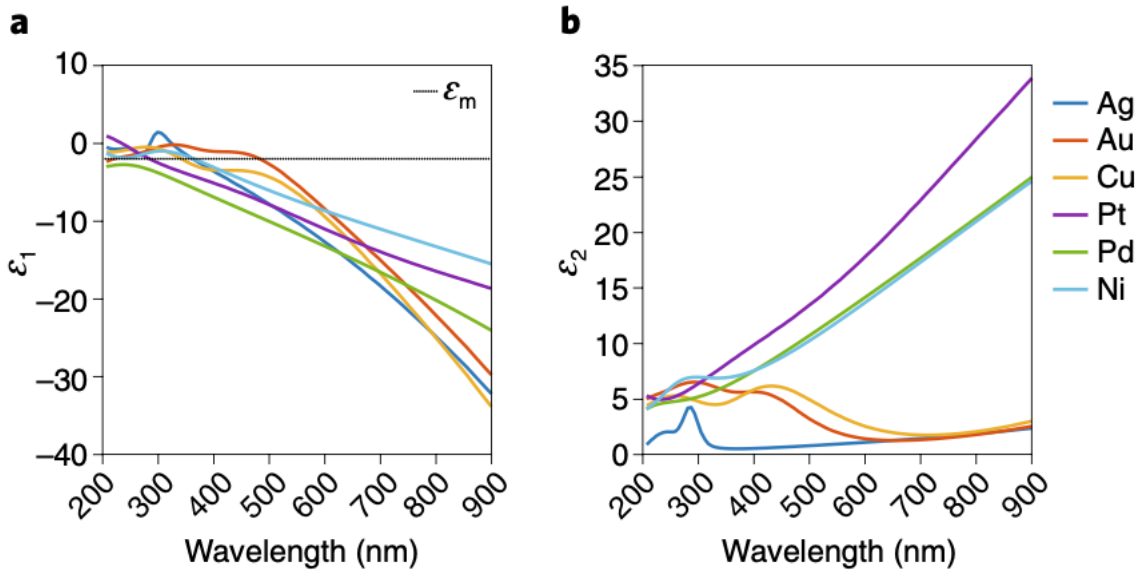


Figure 1.3 *Dielectric function of noble and transition metals. (a) The real part (b) The imaginary part of the dielectric function (reproduced from reference [8])*

The resonant excitation of a large number of carriers is accountable for the large optical extinction cross-sections of plasmonic nanoparticles. The extinction cross-sections (σ_{ext}) can be approximated based on the real part (ε_1), the imaginary part (ε_2) of the dielectric functional of the metal and the dielectric constant of the medium (ε_m) as follows:[8]

$$\sigma_{ext} \sim \frac{\varepsilon_2}{(\varepsilon_1 + 2\varepsilon_m)^2 + \varepsilon_2^2}$$

While the real part (ε_1) represents the polarizability of the metal with respect to wavelength, the imaginary part of the dielectric function (ε_2) illustrates the probability of photon absorption, i.e., the one-electron excitation, which is defined by the property of the electronic

structures of the metal (i.e., filled or unfilled s states and d states). The dielectric properties of some metals are shown in Figure 1.3. Since $\varepsilon_1 \approx -2\varepsilon_m$ in the range of UV-Vis wavelength (the dash back line in Figure 1.3), the extinction cross-sections is larger for those metals with lower ε_2. Due to low ε_2, Au, Ag, Cu, and Al exhibit LSPR in the visible range, and consequently they are commonly used as plasmonic core metal.

Why hybrid plasmonic catalyst?

Although these plasmonic metals can exhibit a strong LSPR under visible light, the lifetime of the excited electrons on these plasmonic metals is relatively short (approximately femtoseconds to nanoseconds). The timescale of a chemical reaction could extend up to microseconds or even seconds.[1] This mismatch in timescale could lead to a low probability of a successfully plasmon-induced reaction, limiting the plasmonic photocatalyst's application. Therefore, the hybrid plasmonic photocatalyst between plasmonic metal and non-zero bandgap material has been studied to extend the average lifetime of charge carriers, enhancing the photocatalyst's photon efficiency. The initial interest in hybrid material was based on the Schottky barrier generated at the metal/semiconductor interface due to the difference in the wave function of the two components. This barrier then delays the traveling back of excited electrons, reducing the recombination of electrons and holes, and consequently increasing the charge carrier's lifetime. In addition, integrating with other catalytic materials can improve the interaction between the adsorbate with the catalyst's surface rather than its relatively inert interaction with noble metals. In principle, by tuning this interaction, we can manipulate the localization of non-equilibrium charge carriers toward the targeted orbitals for desired reactions.

1.2. Scope and Outline

Several types of reactions have been claimed to be induced by the hybrid plasmonic catalyst. However, the complete picture of how non-equilibrium charge carriers affect different types of reactions over the hybrid plasmonic catalyst remains unclear. In addition, how the local environment induced by solvents affects the plasmonic catalysts also remains to be explored. Therefore, this work is aimed to give a fundamental understanding of how non-equilibrium electrons affect reactions on the hybrid plasmonic photocatalyst, especially when the solvent is involved.

To accomplish this task, different types of reactions on hybrid plasmonic catalysts are modeled, including oxide-catalyzed reaction on the hybrid catalyst between plasmonic metals and semiconductor Cu_2O, acid-catalyzed reaction on the hybrid catalyst between plasmonic metals and Lewis acid zeolite (M-BEA or TS-1). The solvent effect is investigated for the ammonia decomposition on the hybrid catalyst between Cu, the plasmonic metal, and Ru, the active center. These probe reactions, including reverse water gas shift, propylene epoxidation, and ammonia decomposition, are selected as the probe reactions due to their application toward a sustainable future.

First, the ground-state and excited-state reaction profiles are investigated for these hybrid materials. The possible reaction pathway under the illumination conditions is then proposed. The probability/feasibility of the targeted reaction is indirectly provided via the charge density analysis or the density of states. The role of defects or doping degrees on integrated materials is also examined to manipulate the localization of electrons on specific orbitals. Finally, the solvent effect is investigated, giving the guidelines for photocatalyst material design and optimum reaction environment.

Before digging into the effect of non-equilibrium charge carriers on the hybrid plasmonic catalyst, a brief introduction of density functional theory is mentioned in Chapter 2. In addition to the ground-state calculation, the linear expansion delta SCF method to perform the excited-states calculations is provided.

In Chapter 3, the effect of non-equilibrium charge carriers on the CO_2 conversion on the hybrid plasmonic catalyst between a plasmonic metal and Cu_2O is investigated. First, the photo-induced CO_2 conversion is examined on the pristine surface of Cu_2O in section 3.1. Then, in section 3.2, the role of the point defects, i.e., the oxygen vacancy on the Cu_2O surface, is studied. The results reveal that without an oxygen vacancy, the intrinsic activation energy of photodissociation of CO_2 on Cu_2O is higher than 3 eV either at the ground state or excited states. However, in the presence of an oxygen vacancy, the intrinsic barrier of this reaction reduces to about 1 eV at the ground state. The remaining barrier can be further reduced or eliminated at the excited states. These oxygen vacancies can be regenerated to complete the catalysis cycle via the hydrogenation reaction to form water. Moreover, this regeneration process is not affected by the non-equilibrium charge carrier.

The effects of non-equilibrium electrons on the acid-catalyzed reaction on the hybrid plasmonic catalyst of Lewis acid zeolite is illustrated in Chapter 4. Particularly, section 4.1 shows the effect of charge carriers on the interaction between molecule and M-BEA, while section 4.2 demonstrates the role of doping level on charge carrier localization via propylene epoxidation reaction on TS-1. We show that introducing photo-excited hot electrons into this hybrid material can tune the interaction between zeolite and molecules when the mid-gap states are available such as in Sn-BEA or Ti-BEA. In addition, using the propylene epoxidation reaction as the probe, our result suggests that the photo-excited electrons can alter the intrinsic activation energy at the

excited state when more electrons are localized at the mid-gap states, which can be obtained by modifying the Ti-doped in TS-1. The higher Ti-doped concentration in TS-1, the higher electron localization at these states.

The solvent effect on the hybrid plasmonic catalyst, i.e., the effect on the excitation energy, is explored in Chapter 5. The H-bond between solvents and ammonia is found to induce the shift of HOMO and LUMO level of ammonia, tailoring the excitation energy of ammonia adsorbed on Ru-doped Cu surface. As a result, it can affect both interfacial charge transfer and the energy transfer process between plasmonic metal and ammonia. The more significant effect on the excitation energy from Fermi level to LUMO is obtained for water and methanol than for phenol due to their higher basicity.

Finally, all main findings in the previous chapters are summarized in Chapter 6. This chapter also gives an outlook for further studies towards a better understanding of the topic.

Chapter 2: Computational method

2.1. Density-Functional Theory

The wave functions and energies of a molecule are found from the Schrödinger equation:

$$\hat{H}\psi = E\psi$$

Since nuclei are much heavier than electrons, the electrons move much faster than the nuclei. Therefore, it can be assumed that the nuclei are fixed during the time of a cycle of electronic motion (The Born–Oppenheimer Approximation). As a result, the purely electronic Hamiltonian is reduced to sum of three terms including electronic kinetic energy of electrons, the attractions between the electrons and the nuclei, and the repulsion between electrons as following:

$$\hat{H} = -\frac{1}{2}\sum_{i=1}^{n} \nabla_i^2 + \sum_{i=1}^{n} v(\mathbf{r}_i) + \sum_{j}\sum_{i>j} \frac{1}{r_{ij}}$$

where $v(\boldsymbol{r}_i)$ is the external potential.

Therefore, if the external potential and the number of the electrons are specified, the wavefunctions and energies can be determined based on the Schrödinger equation.

Hohenberg and Kohn proved that the ground-state electron probability density defines the external potential and the number of electrons. As a result, the ground-state wave function and energy can be determined by the ground-state electron density.

The ground-state energy can be written as the functional of the ground-state electron density as follows:

$$E_0 = E_v[\rho_0] = \overline{T}[\rho_0] + \overline{V}_{Ne}[\rho_0] + \overline{V}_{ee}[\rho_0]$$

$$\overline{V}_{Ne} = \left\langle \psi_0 \middle| \sum_{i=1}^{n} v(\mathbf{r}_i) \middle| \psi_0 \right\rangle = \int \rho_0(\mathbf{r}) v(\mathbf{r})\, d\mathbf{r}$$

Where V_{Ne} is the nuclear-electron attraction, T is the ground-state electronic kinetic energy and V_{ee} is the electronic repulsion energy.

The Kohn-Sham (KS) Method

The Kohn-Sham method considers the noninteracting system of n noninteracting electrons as the reference system, in which:

- The ground-state electron probability density of the reference system equal to the exact ground state electron density of the real molecule

  $\rho_S(r) = \rho_0(r)$
- Each electron experiences the same external potential energy function $v_S(r_i)$

The Hamiltonian of the reference system is

$$\hat{H}_s = \sum_{i=1}^{n} \left[-\tfrac{1}{2}\nabla_i^2 + v_s(\mathbf{r}_i) \right] \equiv \sum_{i=1}^{n} \hat{h}_i^{KS}, \qquad where \quad \hat{h}_i^{KS} \equiv -\tfrac{1}{2}\nabla_i^2 + v_s(\mathbf{r}_i)$$

Kohn and Sham defined the exchange-correlation energy functional, E_{xc} as follows:

$$E_{xc}[\rho] \equiv \Delta\overline{T}[\rho] + \Delta\overline{V}_{ee}[\rho]$$

where

$$\Delta\overline{T}[\rho] \equiv \overline{T}[\rho] - \overline{T}_s[\rho]$$

$$\Delta\overline{V}_{ee}[\rho] \equiv \overline{V}_{ee}[\rho] - \frac{1}{2}\iint \frac{\rho(\mathbf{r}_1)\rho(\mathbf{r}_2)}{r_{12}} d\mathbf{r}_1\, d\mathbf{r}_2$$

Then the ground-state energy can be rewrite as:

$$E_0 = E_v[\rho] = \int \rho(\mathbf{r}) v(\mathbf{r})\, d\mathbf{r} + \overline{T}_s[\rho] + \frac{1}{2}\iint \frac{\rho(\mathbf{r}_1)\rho(\mathbf{r}_2)}{r_{12}} d\mathbf{r}_1\, d\mathbf{r}_2 + E_{xc}[\rho]$$

The first three terms on the right side are the main contribution of the ground state energy, and can be easily obtained based on the ground-state electron density ρ. The fourth term is the exchange-correlation energy, which is not easy to determine exactly but relatively small.

The electron density can be found from the KS orbital as follows:

$$\rho = \rho_s = \sum_{i=1}^{n} \left|\theta_i^{\mathrm{KS}}\right|^2$$

Therefore, if the E_{xc} can be approximated, the Kohn-Sham method can be used to find the electron density and energy.

The Jacob's ladder illustrates five functional categories with more accurate level to approximate the E_{xc}, as follows.

1. LDA functionals: only $\rho(r)$ is involved in the expression for E_{xc}
2. GGA functionals: both ρ and $\nabla\rho$ are involved
3. Meta-GGA: ρ, $\nabla\rho$ and either $\nabla^2\rho$ or τ are involved

4. Hybrid functionals: the exact exchange is added
5. Double hybrid functionals: the dependence on the unoccupied KS orbitals is added

In this work, we use GGA functionals to approximate the E_{xc} to balance the computational cost and the accurate level.

Density of States

The density of states (DOS) is the number of different states which allow electrons to occupy at a particular energy level, i.e., the number of electron states per unit volume per unit energy. In DFT, the total DOS is obtained by integrating related information of atom, orbital or spin at the energy interval, while the project density of state (pDOS) give the projection of particular orbitals or particular atoms on the density of state.

Bellows are the examples for the pDOS of CO when it adsorbed on Pt or Pd. While Figure 2.1 shows the pDOS on particular atoms, in this case is the pDOS on CO; the Figure 2.2 shows the pDOS on particular molecular orbitals, LUMO in this case.

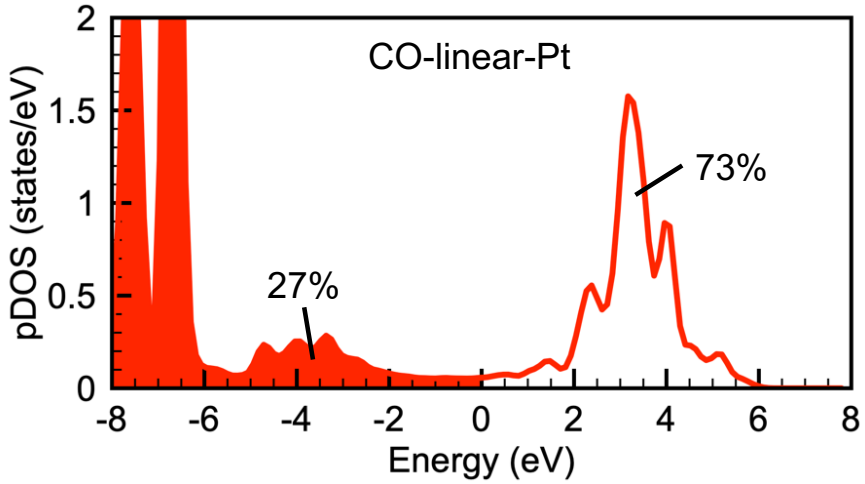


Figure 2.1 *Example of pDOS on adsorbed molecule using VASP: the pDOS on CO adsorbed on a Pt surface.*

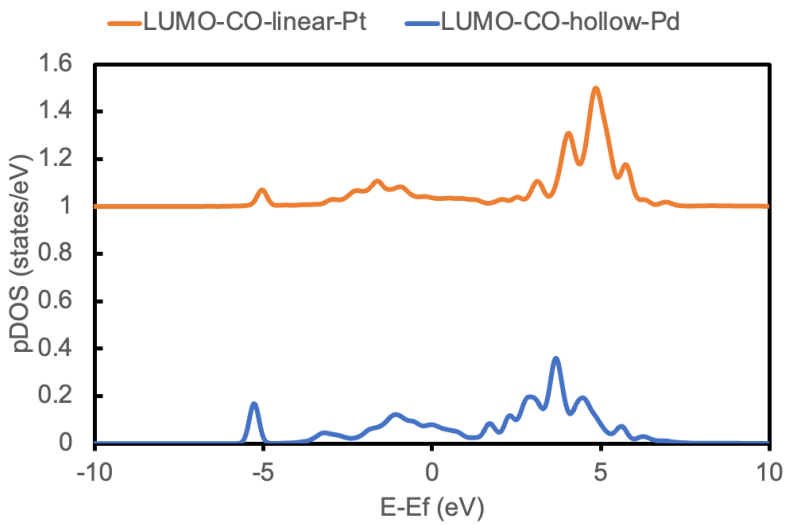


Figure 2.2 *Example of pDOS on particular orbitals using GPAW: the pDOS on the LUMO of CO adsorbed on a Pt or Pd surface.*

Based on DOS and pDOS, other useful information such as the band center or the band width can be calculated. The band center and the band width of molecular orbital are the mean energy and its standard deviation calculated as follows:[11]

$$\bar{E} = \frac{\int \rho(E) E dE}{\int \rho(E) dE} \text{ and } \sigma = \sqrt{\frac{\int \rho(E)(E-\bar{E})^2 dE}{\int \rho(E) dE}}$$

Where $\rho(E)$ represent DOS at corresponding energy E.

Table 2.1 *Example of center and band width of the molecular orbital: The center and bandwidth of LUMO shown in Figure 2.2.*

LUMO	CO-hollow-Pd	CO-linear-Pt
Center (eV)	3.43	4.37
Band width (eV)	1.46	1.36

Absorption coefficient

The absorption coefficient is calculated by the following relation:

$$\alpha = \frac{4\pi\kappa}{\lambda} = \frac{2\sqrt{2}\pi E}{hc}\left((\epsilon_1^2 + \epsilon_2^2)^{\frac{1}{2}} - \epsilon_1\right)^{\frac{1}{2}}$$

where ϵ_1 and ϵ_2 are the calculated real and imaginary parts of the dielectric constant, and E is the corresponding energy.

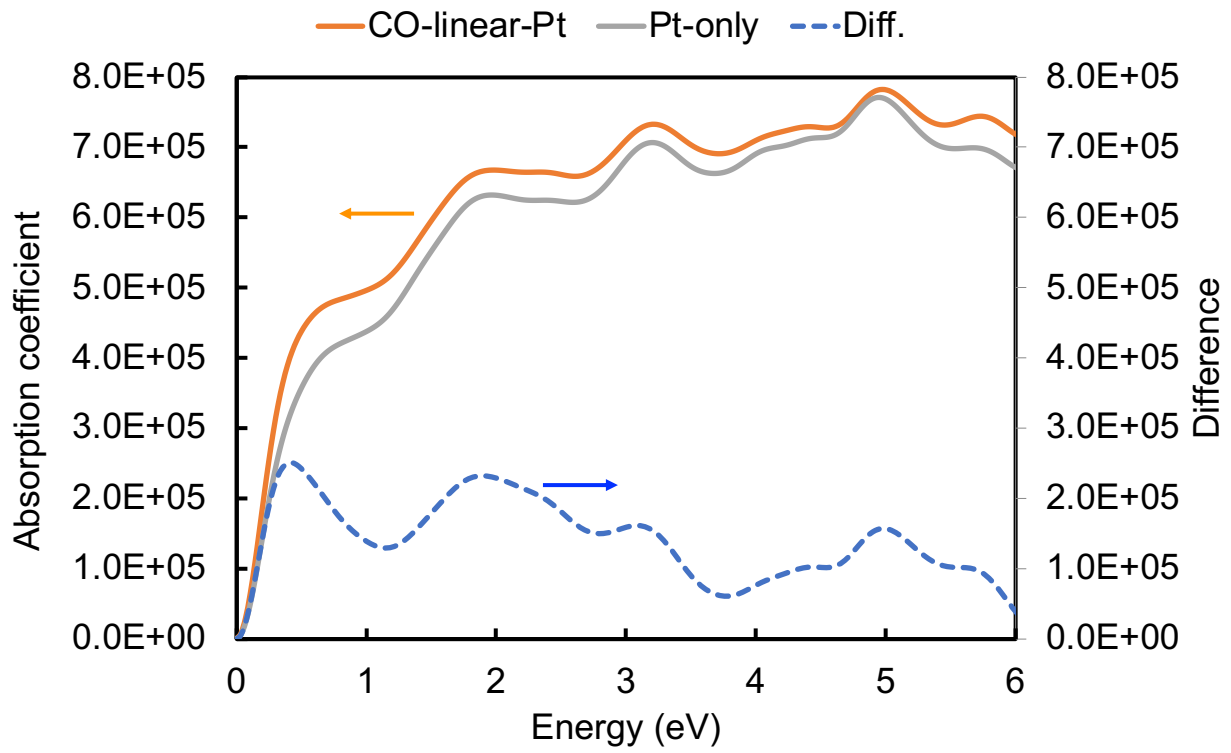


Figure 2.3 *Example of absorption coefficient of CO adsorbed on Pt. Unit: cm^{-1}*

2.2. Excited states calculation using linear expansion ΔSCF

The thermal-driven reaction, in which the vibrational temperatures of system are in equilibrium, can be described by the ground-state DFT calculations based on the approximation that the electron relaxes much faster than the nuclear motion (the Born-Oppenheimer

approximation). Differently, the light-driven reaction involves the excited electron with high kinetic energy, or in other words, the electron temperature and the lattice temperature can be decoupled. Therefore, to calculate the excited potential energy surface, an approach beyond the Born-Oppenheimer approximation is required, either by considering the coupling between electronic states or by an electronic friction model. There are many computational methods have been applied to excited-states calculations such as constrained DFT, Δ self-consistent field (ΔSCF), linear-expansion ΔSCF, time-dependent DFT (TDDFT), and the embedding potential approach. While the TDDFT and embedding potential approach have highly computational cost and complexity, the constrained DFT and ΔSCF can be considered as an extension of the ground-state DFT with similar computational cost. However, the strict constraint in the constrained DFT method may not be a proper approximation for the case when the charge may return to the surface, i.e., the electron back donation. As a result, in this research, the linear expansion delta self-consistent field (ΔSCF) approach[12, 13] are performed to obtain the excited-state energy profiles.

In ΔSCF, the excited state energy can be obtained by controlling the occupation of the Kohn-Sham (KS) states when the system reaches self-consistency as follows:

$$\left[-\frac{\nabla^2}{2} + v_{\mathrm{KS}}[n](\mathbf{r})\right]\psi_i(\mathbf{r}) = \epsilon_i\psi_i(\mathbf{r})$$

$$n(\mathbf{r}) = \sum_{i=1}^{N-1} \psi_i^*(\mathbf{r})\psi_i(\mathbf{r}) + \psi_a^*(\mathbf{r})\psi_a(\mathbf{r})$$

where ϑ_{KS} is the KS potential, and N is the number of electrons.

In the linear-expansion ΔSCF, the excited electron occupy a linear combination of empty KS orbitals, instead of a KS orbital as of the ordinary ΔSCF. This approach gives a much better control on the population of the excited electrons and a good approximation when the molecular orbitals strongly hybridize with the catalyst surface and spread over several KS states.

$$n(\mathbf{r}) = \sum_{i=1}^{N-1} \psi_i^*(\mathbf{r})\psi_i(\mathbf{r}) + \sum_{i,j=N}^{M} a_i^* a_j \psi_i^*(\mathbf{r})\psi_j(\mathbf{r})$$

where the expansion coefficients are chosen based on the molecular orbital (ϕ) as follows:

$$a_i = \frac{\langle \psi_i | \phi \rangle}{\left(\sum_i |\langle \psi_i | \phi \rangle|^2 \right)^{1/2}}$$

In this work, the ground-state calculations were performed using Vienna ab initio simulation package (VASP) version 5.4.1.[14] The optimized structures on the ground state calculated with VASP were utilized to calculate excited states energy profile using GPAW version 22.1.0.[15, 16] The exchange-correlation functional, plane-wave cutoff, U-J value (if any), and k-point grid in GPAW were kept the same as in VASP. The linear expansion delta self-consistent field (ΔSCF) approach[12] was used to calculate the excitation energy. Recent study shown that the linear expansion ΔSCF could provide good agreement with experimental excitation energies, especially for the strong absorption between molecules and catalyst surface as the orbitals are delocalized, and broadened over a range of KS levels.[11] Using CO adsorbed on Pt or Pd as the probe, we also perform the excitation energy calculation for different exchange-correlation over different adsorption configuration of CO and found that the linear expansion ΔSCF also could provide a good agreement with the experimental value of CO excitation energy at the maximum yield.[17]

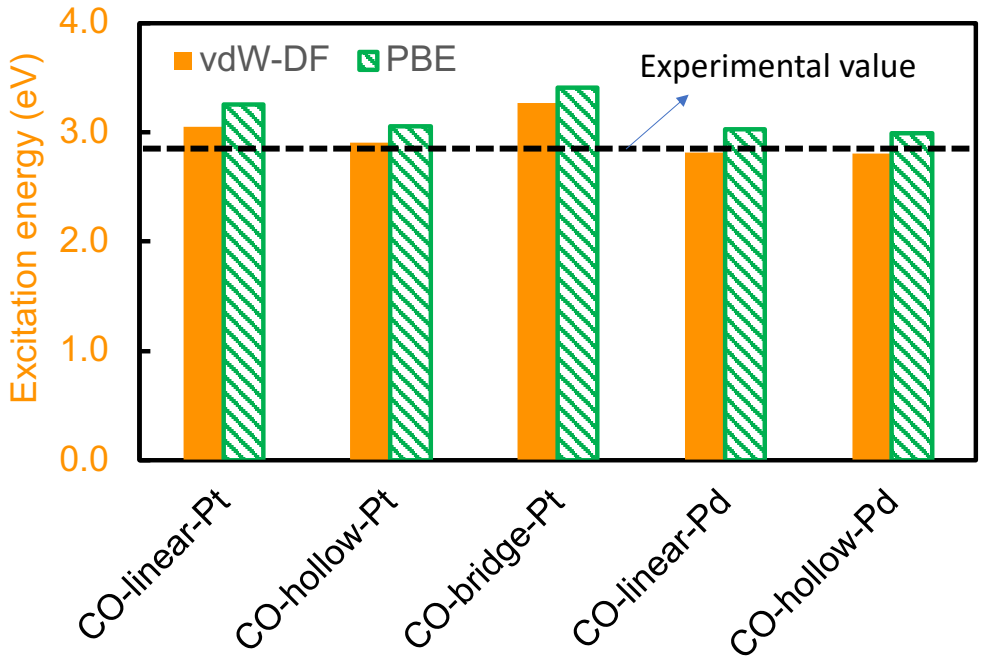


Figure 2.4 *The excitation energy calculated based on vdW-DF or PBE as exchange-correlation functional using GPAW.*

Chapter 3: The hybrid plasmonic catalyst between the plasmonic metal and the semiconductor Cu_2O

3.1. Plasmonic Energetic Electrons Drive CO_2 Reduction on the pristine Cu_2O surface

This chapter is based on a publication in The Journal of Physical Chemistry C. Complete article and supplementary material can be found using the citation: Tien Le, Yihan Shao, Bin Wang, "Plasmon-Induced CO_2 Conversion on Al@Cu_2O: A DFT Study", J. Phys. Chem. C 2021, 125, 6108−6115

Abstract

In plasmonic catalysis, localized surface plasmon was leveraged to drive chemical reactions. This approach is promising for catalyzing many challenging reactions at relatively low temperatures and pressures. We apply density functional calculations to provide the insight for the mechanism of plasmon-induced direct CO_2 dissociation on an Al@Cu_2O core-shell structure, which was observed in a previous experimental study. We show that the interaction of Cu_2O with CO_2 results in the accessible antibonding states of the adsorbed CO_2 in the range of visible light. Though the intrinsic activation barrier for direct CO_2 dissociation is as high as 3.6 eV, we find that an effective reaction barrier of CO_2 dissociation under photon excitation could be reduced by 2 eV. We also show that the charge transfer is more pronounced in the final state of the dissociation due to the strong hybridization of the oxygen with Cu_2O. These results thus provide an explanation for the visible-light-induced direct CO_2 dissociation at relatively low temperature and under ambient pressure. This finding also shows the promising impact of plasmonic catalysis in mitigating carbon emission.

Introduction

Plasmonic catalysis is a promising approach that can alleviate the severity of chemical reactions as well as increase the selectivity of several reactions [9, 18-24]. This photon-driven catalytic process utilizes the local surface plasmon resonance (LSPR) to generate charge carriers when the plasmonic metal nanoparticles absorb light with wavelength longer than their particle sizes. The charge carriers gain high kinetic energy and could enhance molecular motion and chemical transformation[3, 8, 12]. Plasmonic catalysis can thus serve as a new approach to drive reactions at lower temperatures and pressures than those in centralized chemical plants, which is promising for distributed chemical manufacturing[25].

Conventional plasmonic metals, such as gold, silver, aluminum, and copper, have been tested for many reactions, such as oxidation reactions [9, 21], reduction of the nitro group[26, 27], CO_2 reduction[28], and activation of H_2 [18], all showing promising results. A few mechanisms have been proposed for plasmonic catalysis including charge injection into the molecular resonance by charge transfer at the interface, through either Landau damping (LD) or chemical interfacial damping (CID), and plasmon-induced resonance energy transfer (PIRET)[17, 29, 30]. The plasmonic metals can be further integrated with a catalytic material (alloying them with other metals or using a core-shell structure), which could widen the potential application of plasmonic catalysis[31-33]. Several experimental studies and computational simulations have provided insights for different reactions on plasmonic-catalytic-hybrid catalyst such as N_2 dissociation [34, 35], ammonia decomposition [36], methane dry reforming [19], selective hydrogenation[20, 32, 37] and methane dry reforming[19]. More recently, Robatjazi and coworkers investigated the reverse water-gas shift reaction[22] to reduce greenhouse gas CO_2 to CO, a feedstock to produce high-value chemicals via Fischer-Tropsch process. They observed that the reaction could take place under visible light at

low temperature (175 °C) by using a plasmonic antenna-reactor photocatalyst with an Al core and a Cu_2O shell, henceforth denoted as Al@Cu_2O. This hybrid structure is attractive for the following reasons. Cu_2O has been shown as a promising photocatalyst which can absorb the solar light because of its bandgap of 2.2 eV. However, the reaction rate on this semiconductor is relatively low. Therefore, integrating Cu_2O with other metal that has high optical absorption could enhance the efficiency of reactions on Cu_2O. Aluminum was chosen as the plasmonic metal due to its abundancy and outstanding plasmonic optical properties. In fact, the experimental results on Al@Cu_2O have shown a significantly higher reaction rate than pristine Cu_2O or pure Al under same reaction condition[22] . In this reaction, CO_2 dissociation is normally the rate-limiting step[38]. Interestingly, they noticed that, over Al@Cu_2O, CO_2 dissociation could occur even in the absence of H_2 under light illumination, with high selectivity to CO over CH_4; however, the mechanism remains unclear.

Here, we apply density functional theory (DFT) to investigate reaction mechanisms for photocatalytic dissociation of CO_2 on Al@Cu_2O both at the ground state and excited states to provide the insight for (i) the possible reaction pathway of CO_2 dissociation on Cu_2O and (ii) the possible mechanism of charge transfer on Al@Cu_2O antenna-reactor photo-catalyst. Specifically, we find that at ground state, the intrinsic activation energy of CO_2 dissociation is as high as 3.6 eV. We also find that at different excited states, the intrinsic activation energy is almost the same as that at the ground state; however, the effective barrier significantly could be reduced to 1.4 eV. The lowering of the effective barrier enables the CO_2 dissociation to happen at low temperatures. In addition, we notice that the hybrid calculations show a good agreement with PBE+U calculation except higher values of activation energy, which may be caused by the underestimation of the bandgap in PBE+U calculations. The calculations of density of states (DOS) suggest that the

hybridization between CO_2 and Cu_2O orbitals create new low-lying antibonding states under 2.2 eV, which are within excitation range of visible light. Therefore, these new states may be able to be populated by the highly energetic electrons. We further show that the charge transfer is more pronounced in the transition and final state of the dissociation than the initial state due to the strong hybridization of the oxygen with Cu_2O. As a result, the CO_2 dissociation reaction is possible in the range of visible light. The charge transfer mechanisms are possible, and our analysis shows that the highly energetic electrons seems likely to originate from the plasmonic metal and to be transferred to adsorbate molecular orbitals via LD or CID mechanism rather than being excited from the valence band of Cu_2O.

Computational Method

Here we emphasize on the role of electrons and holes in catalysis, so instead of modeling the plasmon generation and its dynamics we focus on the electrons and holes populated at the interface after surface plasmon dephasing. DFT calculations were performed using the VASP package[14]. The exchange-correlation functional PBE[39] combined with DFT+U[40] (henceforth denoted PBE+U) was used. The van der Waals interaction was included by employing the DFT-D3 dispersion model [41]. Although the Cu_2O (111) and Cu_2O (110) surfaces were observed in the experiment [22], the most stable surface, the Cu_2O (111) surface [42], was selected in this study. The model is constructed based on (2 x 2) repeated slabs of Cu_2O (111) with a lattice parameter a = 4.27 Å taken from the optimization of Cu_2O unit cell. The O-terminated Cu_2O (111) surface structure had five O-Cu-O layers. While the top two layers were fully relaxed, the bottom three layers were fixed at their bulk positions. A vacuum of 15 Å was added along the z axis perpendicular to the surface. A U-J value of 6 eV was used for Cu as recommended in literature [43, 44]. The CO_2 molecule was positioned on the reconstructed Cu_2O (111) surface. The total energy

calculations reported in this study used a k-point grid of (1 x 1 x 1). We compared the results with a (3 x 3 x 1) calculation and found that the activation energy and reaction energy only differed by 0.01 eV between these two settings of the k-points. Therefore, the results obtained using a k-point grid of (1 x 1 x 1) was reported in this study to simply the analysis of the Kohn-Sham (KS) orbitals. The energy convergence for electronic relaxation was set to 10^{-6} eV. All atoms were relaxed until the atomic force < 0.02 eV/Å with a kinetic energy cutoff of 400 eV. The nudged elastic band (NEB) method [45] and the dimer method [46] were used to find the transition state and calculate the activation energy barriers. The initial states, transition states and final states were fixed at the optimized structures from the PBE+U-D3 calculations and calculated using HSE (Heyd–Scuseria–Ernzerhof) hybrid functional to reduce the charge delocalization error [47] as we did previously[48].

To calculate the excited state energies, we applied the ΔSCF approach [49, 50]. In this approach we first performed ground state DFT calculations of the initial, transition and final states as described above. Then, to determine where the electron and hole could be positioned, we identify the KS orbitals by analyzing the local density of states and decomposed charge densities. We then chose those KS orbitals within the experimental excitation range and performed a SCF calculation with a new set of occupied and unoccupied KS orbitals, where an additional electron was added to an unoccupied KS orbital. Holes were created by removing electrons from the Fermi level. This practice is in principle challenging for large periodic systems; however, in this study, due to the semiconducting nature of the Cu_2O, there are only about a dozen of states of interests, and such an approach is feasible and provides meaningful results as discussed below. Note in this study the Al metal was not directly included in the model partially because the complexity of the resulting hybrid structure and partially because in the experiments the Al metal is normally covered by a thin film of amorphous Al_2O_3 layer[22]. Here, we adopted two models to simulate the system:

in one model, we used the ΔSCF method to add one additional electron into the Cu_2O/CO_2 to simulate the effect of hot electron generated from excited Al. The hole was assumed to stay within Al; in the other model, an electron and a hole both present in the system, and the hole stays at the Fermi level of Cu_2O.

The Bader charge analysis is applied to analyze the difference in charge density between the excited states and the ground state [51]. We find that, regardless of the spin states of the added electron is assigned up or down, the converged total energies of the system at initial states are the same. In contrast, the calculated total energies of the system at final states are slightly different. However, this difference is negligible and within the calculation errors.

Results and discussion

As mentioned above, CO was observed under the experiment condition without H_2 in the feedstock [22]. Therefore, in this study, we focus on the CO_2 direct dissociation mechanism for the reverse water-gas shift reaction on $Al@Cu_2O$ instead of other possible reaction mechanisms[38]. To simply the discussion, the two oxygen atoms in CO_2 are labelled O1 and O2, respectively (see Figure 3.1.1). At the ground state, CO_2 adsorbs with a tilted configuration in which O2 forms a chemical bond with an unsaturated Cu atom at the equilibrium adsorbate geometry, similar to previous studies [43, 52]. Compared to the initial state, at the transition state, the C-O2 bond is rotated to a position that carbon atom forms a chemical bond with the unsaturated copper atom while C-O1 bond is stretched by copper atoms nearby (Figure A1.1). The C-O1 bond ultimately breaks, so O1 ends up at a hollow site of nearby copper atoms. This dissociation process is highly endothermic, with a reaction energy of 1.6 eV by PBE+U (1.4 eV by HSE06). As a result, significant activation energy is required to break the C-O bond, 3.2 eV in a PBE+U calculation

(3.6 eV in a HSE06 calculation) (Figure 3.1.1). This follows a similar trend with reported values by Mishra et al [38]. Therefore, it is suggested that the direct CO_2 dissociation on a pristine Cu_2O (111) surface cannot happen at low temperatures.

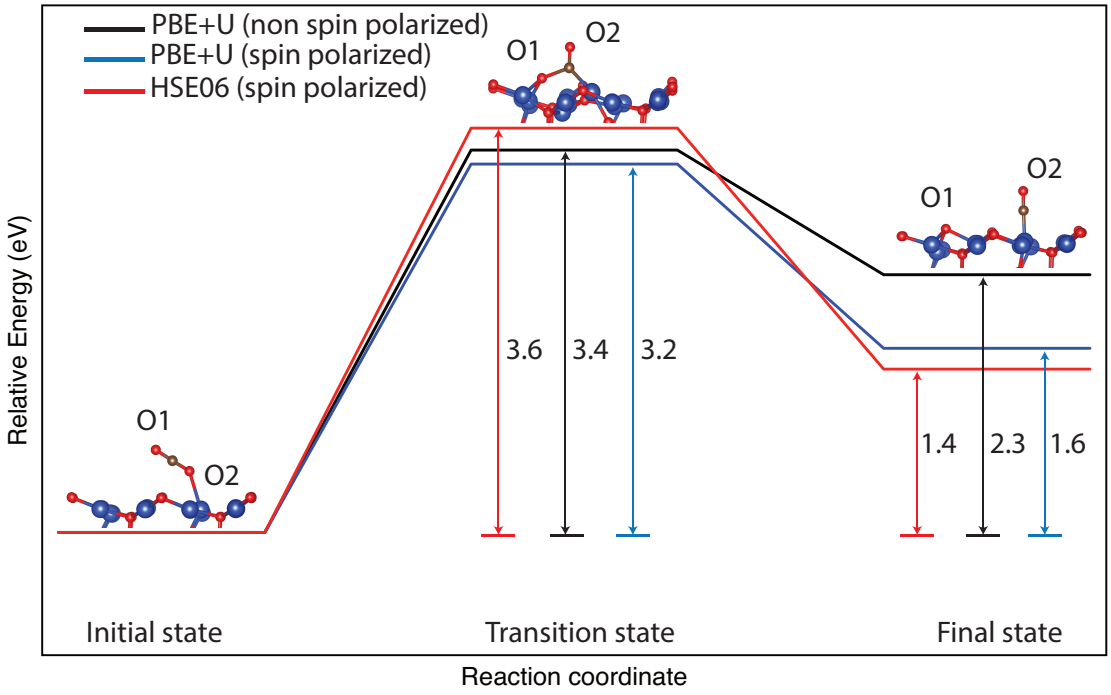


Figure 3.1.1 *The energy diagram of CO_2 dissociation at the ground state calculated in PBE+U calculations with and without spin polarization and by spin-polarized HSE06 calculation. The blue, gray and red balls denote Cu, C and O atoms respectively.*

The initial state of CO_2 adsorption on a Cu_2O (111) surface is spin unpolarized at the ground state; however, the higher spin is more favorable for the adsorbed oxygen atom (dissociated from CO_2) at the final state due to its open shell electronic structure. Therefore, the magnetic moment changes along reaction pathway from 0 at the initial state to 1 μB at the final state. At the PBE+U level, the optimized structure of transition state can have either a singlet or a triplet spin state with degenerate total energies. However, in the HSE06 calculations, when the errors of

fractional electron and fractional spin are reduced [47], the orbital levels are more discrete, and the triplet spin state is favored by 0.6 eV. In addition, the transition state is more likely a late transition state for this endothermic process, so the spin states of transition state are expected to be similar to the final states.

To complete the reaction cycle, the CO desorption energy is around 1.3 eV in PBE+U calculations. The dissociated O atom can then combine with dissociated H atom (from H_2 when it is co-fed) to form OH. This combination is favorable by 0.9 eV in our calculation. There is almost no barrier of H_2O formation from surface OH and H atom on the Cu_2O (111) surface, and the desorption energy of H_2O on Cu_2O (111) surface was reported to 1.2 eV [38]. Thus, the oxygen overage on the surface should be quite low during the reaction due to the facile formation of water and its desorption. The H_2 dissociation, the formation and desorption of H_2O have been investigated previously. The dissociation barrier of H_2 on Cu_2O (111) surface is reported to be very low [38]. These energy barriers are much lower than the activation energy of CO_2 dissociation, suggesting the latter one is the rate-determining step. We thus expect that if the LSPR can reduce the activation barrier of this rate-determining step, the overall reaction rate will increase, assuming other elementary steps retain their minor roles in determining the reaction kinetics.

In the following, we investigate the electronic structure of CO_2 adsorbed on the Cu_2O (111) surface. The high energy of antibonding states of CO_2 in gas phase [53] make it impossible to be excited by the visible light without adsorption on the catalyst surface. The crystal orbital Hamilton population (COHP) analysis is shown in Figure A1.2. When CO_2 is adsorbed on the Cu_2O surface, the major antibonding state of CO_2 is at ~ 3.5 eV above the Fermi level of Cu_2O in the PBE+U calculation (~4.3 eV in HSE06 calculations) (peak III, Figure 3.1.2), which is too high to be excited by visible light. However, there are hybridized states between CO_2 and Cu_2O at ~ 0.7 eV (peak I)

and 1.7 eV (peak II) in PBE+U calculations (Figure 3.1.2b). The bandgap of Cu_2O is underestimated at the PBE+U level, so the HSE06 calculation is applied here to compare. The hybridized states between CO_2 and Cu_2O is now adjusted to ~ 1.2 eV (peak I) and 2.2 eV (peak II) in the HSE calculations (Figure 3.1.2d). Figure 3.1.2 clearly shows that the hybridization of Cu_2O and CO_2 creates new low-lying antibonding states of CO_2 (below 2.2 eV) (see Figure A1.2 for the COHP analysis). Therefore, the energy of excited electrons generated by LPSR and the antibonding level are comparable, so charge transfer can in principle happen and highly energetic electrons may populate the antibonding states of CO_2. In other words, the interaction between Cu_2O and CO_2 makes the antibonding states of CO_2 now accessible in the range of visible light.

The LSPR of antenna plasmonic catalysis for CO_2 direct dissociation over Al@Cu_2O was observed at 2.2 eV [22]. Therefore, the vertical excited states in the range of energy up to 2.2 eV based on HSE06 calculation were selected to investigate in the following study. Despite the fact that the electron excitation can occur at any point along reaction pathway [54], the vertical electron excitation based on initial, transition and final states of the ground state potential energy surface is focused here. It is challenging to reveal the mechanism pathway in excited states via experiments [54], and the DFT calculations presented here suggest that there are possible pathways that help reduce the energy barrier as discussed below.

If an electron is injected into the antibonding states of a molecule through either direct or indirect charge transfer driven by the excitation via LSPR, this process could induce molecular motion due to the shifting of minimum on the excited potential energy surface[12]. Then, the system could cross to lower excited state potential energy surfaces before decaying and returning to the ground state. Since there is a linear relationship between light intensity and the reaction rate

observed in the experiment [22], the single excitation process is considered here instead of multiple excitation process.

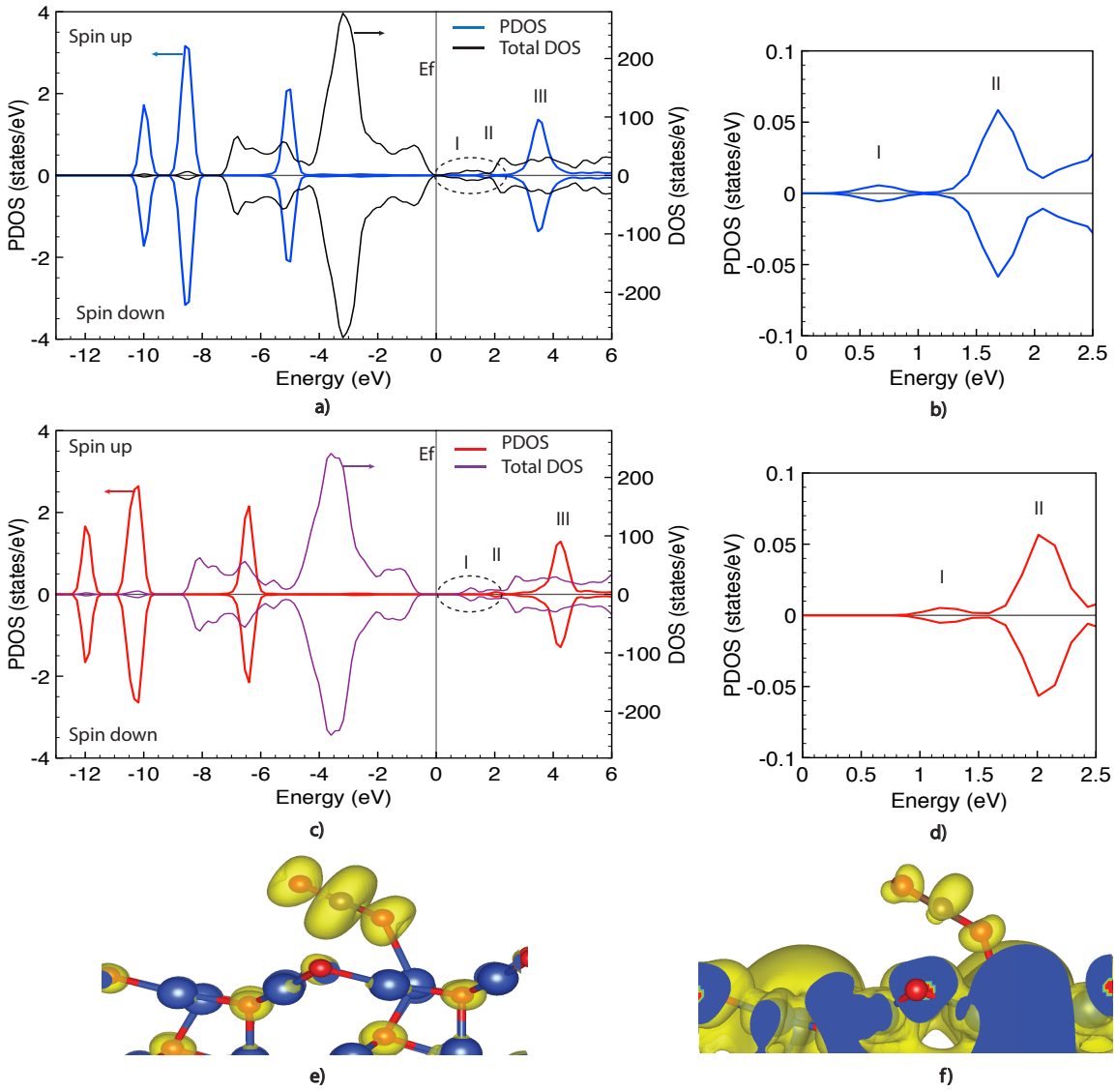


Figure 3.1.2 *The projected density of state (PDOS) of CO_2 adsorbed on Cu_2O and the total DOS calculated by PBE+U (a) and HSE06 (c). The zoom in areas from Fermi level to 2.5eV of PDOS are shown in b) for PBE+U calculations and in d) for HSE06 calculations. The partial charge of CO_2 adsorbed on Cu_2O (111) surface at initial state: (e) partial charge from 3.0 to 4.0 eV above*

Fermi level; and (f) partial charge from 0 to 2.5 eV above Fermi level (based on PBE+U calculation)

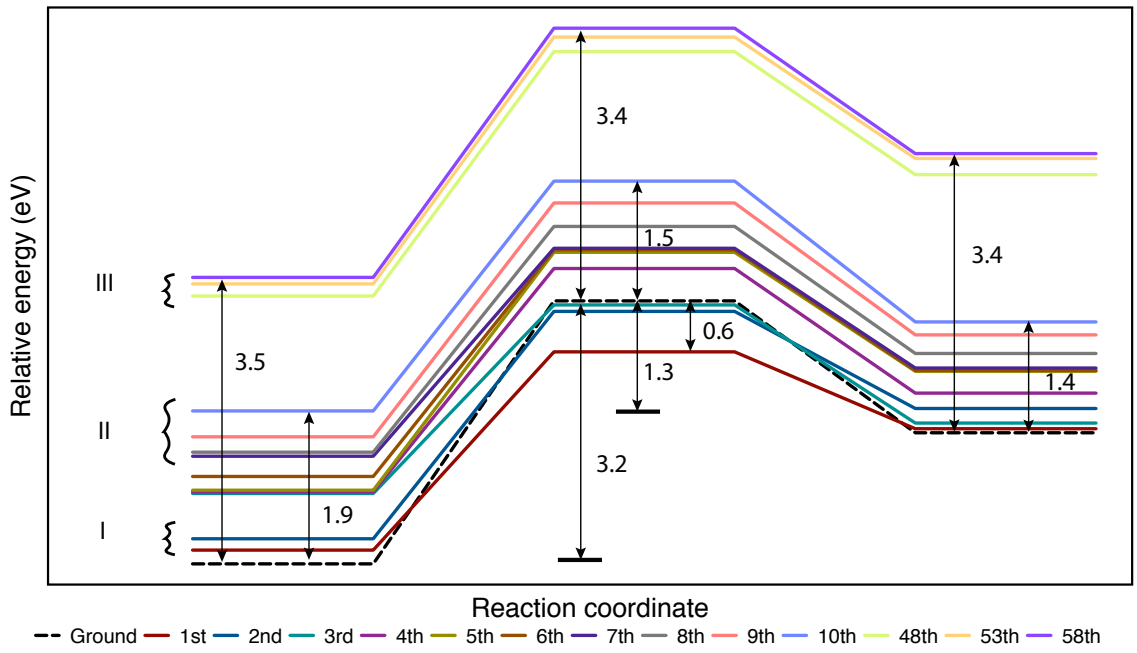


Figure 3.1.3 *Ground state and excited state energies (eV) along reaction pathway obtained using the PBE+U calculations combined with the ΔSCF approach. Each colored line represents a reaction profile mapping from the initial state to the final state by manipulating electronic occupation at different electronic states above the Fermi level. Groups of I, II, III correspond to the groups of states shown in the DOS calculations in Figure 3.2. The excitation at the initial, transition and final states are labelled for some of the vertical transitions.*

As shown in Figure 3.1.3, if the electron is added into the orbital in the peak II using the ΔSCF approach, the system could be excited up to 1.9 eV higher than the ground state. The system can cross to a lower potential energy surface and return to the ground state level at the transition

state to complete the reaction pathway. As a result, the effective activation energy could reduce from 3.2 eV to 1.3 eV (Figure 3.1.3). The first and second excited state levels of the transition state structure are lower than the ground state; this is likely due to the challenge of accurately calculating transition states with similar spin states in the DFT calculations using local and semi-local functionals[47]. This issue is addressed when using a hybrid functional (Figure 3.1.4). At transition state, the energy again when adding an electron into the first unoccupied KS orbital stabilizes the transition state because of its otherwise open-shell electronic structure, leading to a lower energy of the first excited state than the ground state. The hybrid functional calculation shows a similar trend with PBE+U calculation but with higher activation energy. The electronic excitation of 2.2 eV can populate the antibonding state of CO_2 and the system can decay to lower levels or the ground level along different potential energy surfaces similar to the discussion of the PBE+U calculations. Consequently, the effective reaction barrier could reduce from 3.6 eV to 1.4 eV (Figure 3.1.4). Even if the system shifts to a lower potential energy surface rather than the ground state potential energy surface, such as through the first or second excited state at the transition state, the effective barrier could still be significantly reduced by ~ 2 eV. In the next steps, the reaction could follow the lowest excited potential surface and decay to the ground state. Overall these calculations suggest that, if the system is excited by LSPR and returns to the ground state potential energy surface right before crossing the transition state, only 1.4 eV of effective energy barrier is required to dissociate CO_2. Assuming a pre-exponential factor of 10^{14}, the turnover frequencies at 175°C is around 0.02 s^{-1}, which suggests that the direct plasmonic CO_2 dissociation on Cu_2O can happen at low temperature and ambient pressure as observed in the experiment[22].

We also considered the empty states (peak III) that are far above the ground state. We tried to add an electron into this main LUMO peak in both PBE+U and HSE06 level. The results are

similar to adding electron into the hybridized orbitals (peaks I and II). The intrinsic activation energy (between the initial state and transition state) at ground potential surface and excited potential surfaces are still comparable.

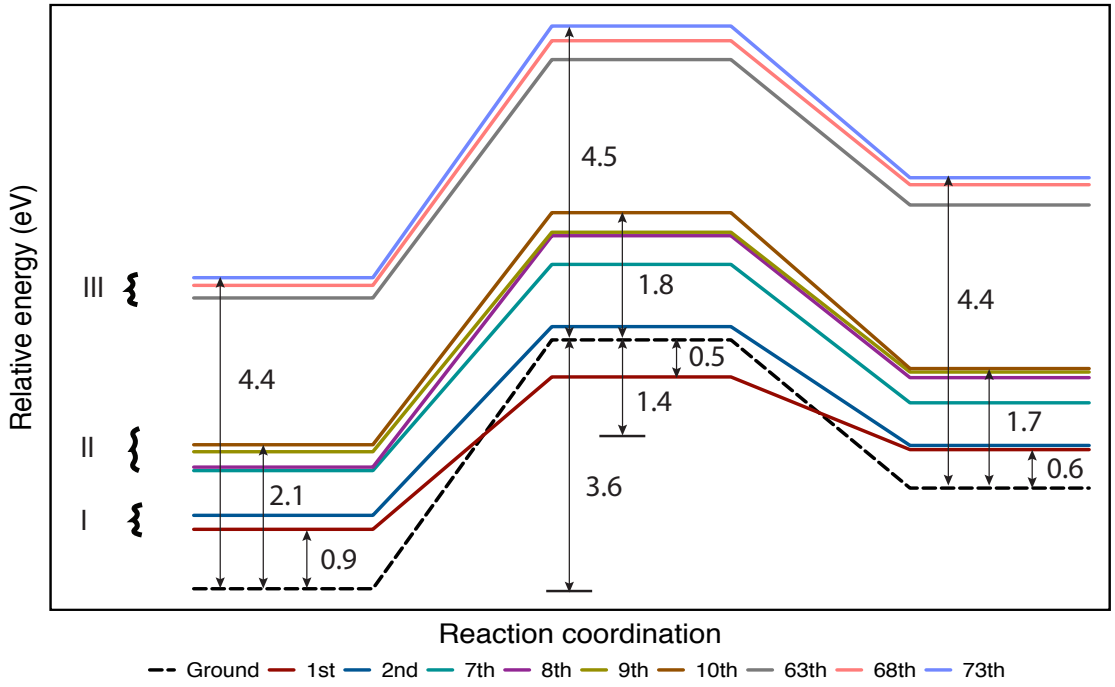


Figure 3.1.4 *Ground state and excited state energies (eV) along reaction pathway predicted by the HSE06 functional combined with the ΔSCF approach. Each colored line represents a reaction profile mapping from the initial state to the final state by manipulating electronic occupation at different electronic states above the Fermi level. Groups of I, II, III correspond to the groups of states shown in the density of states calculations.*

It is worth noting that the results shown in Figure 3.1.3 and Figure 3.1.4 are obtained from calculations with only 1 electron added into the unoccupied KS states. Here we also compare them with the calculations of the vertical excitation energies with both an added electron and a hole at Fermi level. In Figure 3.1.5, we show the energy difference between these two calculations

(calculations with one electron compared with calculation with both an electron and a hole). We find that, in addition to the energy cost to populate an electron into the different antibonding states, an amount of 0.6 to 0.8 eV is required to create a hole at Fermi level of Cu_2O at initial state. For the transition state, this excess energy is ranging between 0.6 and 0.9 eV. This similar increase of energy in both initial state and transition state leads to the insignificant change of the intrinsic barrier (up to 0.3 eV) obtained in these two calculations. The resulting potential energy surface with both an electron at the different KS orbital and a hole at the Fermi level is plotted in Figure A1.3. However, due to higher energy requirement to create a pair of electron and hole, the number of states which could be populated by an excited electron will thus be less when considering a hole remaining at the Fermi level. It is also interesting to notice that in this calculation the hole is positioned at the Cu_2O Fermi level, partially because the plasmonic metal such as Ag and Al are not included in the calculation model. This additional effect will be discussed below.

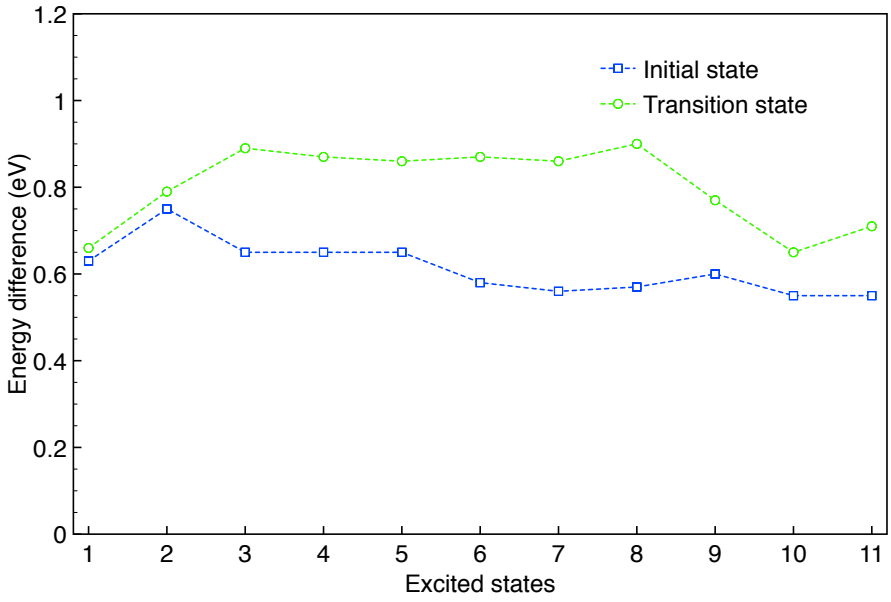


Figure 3.1.5 *The energy difference of the total energies between the system with an added electron and a hole at Fermi level of Cu_2O and the system with an added electron only (PBE+U).*

Here we briefly discuss the potential mechanism for charge and energy transfer at the $CO_2/Cu_2O/Al$ interface to drive the C-O bond cleavage. As discussed above, the charge and energy transfer mechanism for plasmonic catalysis is still unclear and may vary between different systems. The charge transfer mechanism via the LD process has been proposed for many years. The highly energetic carriers generated from LSPR via LD can dissipate their energy via electron-electron and electron-phonon scattering, leading to electron thermalization toward the Fermi–Dirac distribution. During this thermalization, non-equilibrium electrons with high kinetic energy can transfer from the plasmonic substrate to unoccupied states of adsorbed molecule.[3, 8] An alternate charge transfer pathway is the direct electron transfer via CID [29]. This direct charge transfer process often happens when the molecules strongly adsorb on the plasmonic catalyst, adding new electronic states at the interface and offering new plasmon resonance dephasing pathway. This direct mechanism was proposed to be more efficient and bond selective than the indirect charge transfer [8, 29]. The electron-hole pairs can also be generated in the molecules via PIRET driven by dipole-dipole coupling between the molecules and the plasmonic metal [55].

By analyzing the absorption coefficient of Cu_2O with and without adsorbed CO_2 (see Figure A1.4), we saw that the adsorbed CO_2 on Cu_2O surface enhances the absorption coefficient of the system under the range of visible light. Especially, we found that the energy level showing the enhancement of the absorption coefficient closely matches with the energy level of hybridized orbitals between CO_2 and Cu_2O, implying that this chemical interfacial interaction could influence the plasmon dephasing pathway. This calculation also suggests that the charge carrier can be transferred directly via the CID mechanism [29] besides the indirect electron transfer via LD mechanism. Comparing the work function of Al [56], the electron affinity of Cu_2O [57], and the band gap of Cu_2O [44], we find that the Fermi level of Al is comparable with the Fermi level of intrinsic

Cu_2O. Therefore, if the highly energetic electrons are originally generated from Fermi level of plasmonic material, the energy of resonance at 570 nm [22] is sufficient to populate the antibonding states of adsorbed CO_2.

The formation of transient negative ion is normally proposed for the LD and CID mechanisms [9, 18] in which the electron is excited from catalyst by LSPR and then directly or indirectly injected into the hybridized antibonding orbital of molecule, leading to bond breaking (Figure 3.1.6). We thus conducted Bader charge analysis to compare the charge density difference between the ground state and excited states of CO_2 (Table A1.1 and A1.2). The corresponding charge density difference is plotted in Figure A1.5. In the presence of just an additional electron, assuming the hole remains in the Al (not included in this calculation), we find that the electron transfer to CO_2 is more pronounced at the transition and the final state because the hybridization of Cu_2O with dissociated species (CO and O) is much stronger than with CO_2 at the initial state. However, about 20% at most of this negative charge can be localized on the CO_2 or its dissociated species. This finding holds true if one hole is introduced at the Fermi level; the hole is localized mostly within Cu_2O. The charge transfer overall is thus small but also visible particularly at the transition and the final states.

Alternatively, if the plasmonic metal Al absorbs light and transfers this photon energy to semiconductor Cu_2O via dipole-dipole coupling, the pair of a hole and an electron can in principle be generated in Cu_2O via PIRET mechanism. The LSPR energy (up to 2.2 eV) harvested in the experiment is just similar to the band gap of Cu_2O, so the PIRET scenario only allows transfer of charge carriers near conduction band edge of Cu_2O[55]. Therefore, there is only few numbers of antibonding states that could be populated in case the PIRET scenario on Cu_2O. As a result, it is challenging for the excited electrons in Cu_2O to reach the CO_2 antibonding orbital level from Cu_2O.

The energy can also transfer to adsorbed molecule via dipole-dipole coupling following the PIRET mechanism. However, our calculations suggest that the HOMO of adsorbed CO_2 is too deep below the Fermi level, so the visible light does not have enough energy to generate the hole-electron pairs within CO_2. The PIRET mechanism is claimed to be less efficient than direct absorption due to the high dependence on distance between the donor and acceptor ($1/R^6$) and their spectra overlap [55]. In this particular system studied in this calculation, it seems likely that the highly energetic electron is originated from Al via LD or CID mechanism rather than being excited through resonant energy transfer. The minor difference between charge density of the ground state and excited states could result from the strong electronic overlap between CO_2 and Cu_2O leading to ambiguous assignment of the electrons (Figure 3.1.2 and A1.5). We summarize this discussion in Figure 3.1.6 and note that, due to the similar work function of Ag and Al, Ag could be an alternative candidate for the plasmonic metal for the same chemistry.

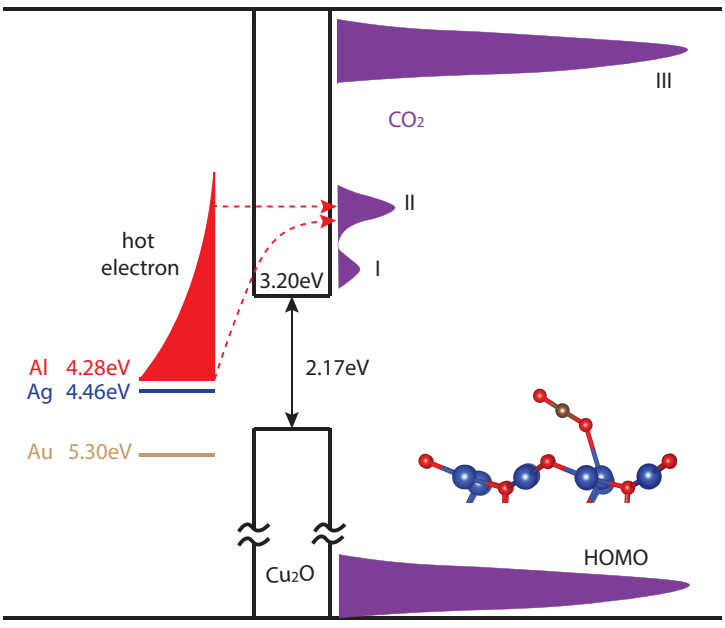


Figure 3.1.6 *Possible charge transfer mechanism. The work function of Al, Ag, and Au taken from literatures* [56, 58, 59]

Conclusions

We performed DFT calculations to provide the insight for the mechanism of plasmon-induced direct CO_2 dissociation on an Al@Cu_2O core-shell structure. By examining the density of states, we show that the interaction of Cu_2O with CO_2 results in accessible antibonding states of the adsorbed CO_2 in the range of visible light. By analyzing vertical excited states along the reaction pathway, we suggest that an effective reaction barrier of CO_2 dissociation under photon excitation could reduce to a third of its intrinsic activation barrier at the ground state. These findings provide an explanation for the visible-light-induced direct CO_2 dissociation at low temperature and under ambient pressure, even in the absence of H_2. This finding shows the promising impact of plasmonic catalysis in mitigating carbon emission. The calculation also suggests that, in addition to aluminum, silver may also work as the plasmonic core for the reduction of CO_2 over Cu_2O. It is worth noting that we don't include structural defects in the current calculations. We anticipate that the presence of defects, such as oxygen vacancies, will not only change the reaction profile at the ground state but also the vertical excitation energy due to the modified interfacial hybridization and presence of mid-gap states.

Acknowledgements

This work was financially supported by the Department of Energy (Grant No. DE-SC0020300). The DFT calculations were performed using computational resources at the OU Supercomputing Center for Education & Research (OSCER) at the University of Oklahoma and the National Energy Research Scientific Computing Center (NERSC), a U.S. Department of Energy Office of Science User Facility. The authors acknowledge Dr. Marimuthu Andiappan for the valuable discussions.

3.2. Plasmonic Energetic Electrons Drive CO_2 Reduction on Defected Cu_2O

This chapter is based on a publication in ACS Catalyst. Complete article and supplementary material can be found using the citation: Tien Le, Taha Salavati-fard, and Bin Wang, ACS Catal. 2023, 13, 9, 6328–6337.

Abstract

Plasmonic photoreduction of CO_2 is valuable for decarbonization and producing value-added chemicals. However, insights into mechanisms of this reaction remain elusive particularly regarding the roles of structural defects and their interplay with the non-equilibrium charge carriers. Here, we report density functional theory (DFT) calculations on Cu_2O, a prototype photocatalyst, through which we investigate CO_2 reduction over three defected facets to reveal the interfacial charge transfer and bond dynamics under plasmonic excitation. We find that the activation barrier of C-O bond cleavage decreases from 3.2 to about 1 eV assisted by oxygen vacancies, and that the remaining barrier can be further reduced or eliminated at the plasmon-excited states when Cu_2O is integrated with plasmonic metals. The regeneration of oxygen vacancies (by H_2 to form water) on Cu_2O to complete the catalysis cycle is feasible and not affected by the energetic electrons. Our calculations thus show the important synergistic effect of energetic electrons and point defects to promote CO_2 reduction.

Introduction

The capture, storage, and conversion of CO_2 has received a lot of interest as key components of a decarbonized economy. On the industrial front production of value-added chemicals using CO_2 as a feedstock is desirable, yet very challenging due to the high stability of CO_2 associated with strong molecular bonds. Photocatalytic CO_2 transformation, utilizing light

irradiation to facilitate CO_2 activation, are in prime position to address the related energy and environmental concerns[5, 53, 60-64]. Among the extensively studied photocatalysts, cuprous oxide (Cu_2O) is a promising candidate due to its earth-abundant elemental composition, intrinsic p-type conductivity, and suitable energy bandgap for electronic excitations by visible light (~2.1 eV).[65] Cu_2O-based photocatalysts have been widely studied experimentally for CO_2 reduction, and several approaches have been proposed to enhance the catalytic activity and stability. These notable approaches include the Z-scheme system to couple Cu_2O with TiO_2 or ZnO and the 'antenna-reactor' photocatalysis with plasmonic nanoparticles such as Au, Ag, Cu, and Al as an antenna.[22, 65-74] For example, a Al-Cu_2O core-shell plasmonic photocatalyst showed higher and more selective reverse water-gas shift reaction ($CO_2 + H_2 = CO + H_2O$) than the individual counterparts of Cu_2O and Al, which was attributed to energetic charge carriers in Al and enhanced optical absorption in Cu_2O.[22]

It is generally agreed that this reduction reaction starts with bond cleavage C-O in CO_2 to form CO;[71] however, the CO_2 photoreduction over Cu_2O is challenging because the direct dissociation of CO_2 on the defect-free surface is kinetically unfavorable manifested by a high intrinsic activation energy.[75] Defect engineering (e.g., surface vacancies) and crystal facet engineering have thus been investigated to improve the activity and stability of CO_2 photoreduction.[65] The photocatalytic performance of Cu_2O highly depends on the catalyst facet.[74, 76-78] Because of diverse atomic arrangements, each facet has distinct electronic structures, optical properties, and molecular adsorption energy, which result in different reaction kinetics. In addition, surface defects, such as copper and oxygen vacancies and atomic impurities, can change electronic band structure, introducing additional degrees of freedom to manipulate light absorption and charge carrier dynamics.[79] Indeed, lattice imperfection can elevate photocatalytic activities of

Cu_2O; a recent study proposed that excited electrons, in the presence of oxygen vacancies, could significantly enhance the performance of Cu_2O for CO_2 reduction.[73] Oxygen vacancies have also been found capable for facilitating the photo-activation of CO_2 on TiO_2.[53, 80] However, how photo-excited charge carriers work together with structural defects on different facets to promote the CO_2 photocatalytic reduction still remains unclear.

Here, we report density functional theory (DFT) calculations, through which we investigate the effects of energetic electrons, generated by plasmonic excitation, and their interplay with oxygen vacancies, on CO_2 photoreduction. We focus on the oxygen vacancies generated on the three most stable Cu_2O facets, namely, the (111) facet, the (111) facet with Cu vacancies, and the (110) facet. We find that oxygen vacancies can reduce the reaction energy of CO_2 reduction to much less endothermic values than the pristine (111) surface. This reduction in reaction energy also results in a significant decrease of the reaction activation barrier (i.e., from 3.2 eV on the pristine surface to 0.9-1.1 eV on oxygen-deficient surfaces). This remaining barrier can be eliminated by plasmonic energetic electrons. The extent of reduction in the activation energy on oxygen-deficient surfaces with and without the energetic electrons can be attributed to the different population of the antibonding states in CO_2. That is, only a few low-lying antibonding states of CO_2 can be occupied through interfacial transfer of the excess electrons associated with oxygen vacancies, leading to a limited level for decreasing the activation energy under purely thermal-driven conditions. Instead, the highly energetic electrons generated by light irradiation can populate antibonding states of CO_2 more extensively, leading to further reduction of the activation barriers. We find that after excitation, the system will likely travel on an excited energy profile and then return to the ground state to complete the reaction. Moreover, we find that formation of oxygen vacancies on Cu_2O is feasible via hydrogenation as the intrinsic activation energy for this

formation ranges from 0.9 to 1.1 eV. The energetic electrons however have no impact on the intrinsic barrier of this vacancy formation step. Our studies thus reveal that the major impact of plasmon-induced energetic electrons is to drive the CO_2 dissociation at the oxygen vacancies.

Results and discussion

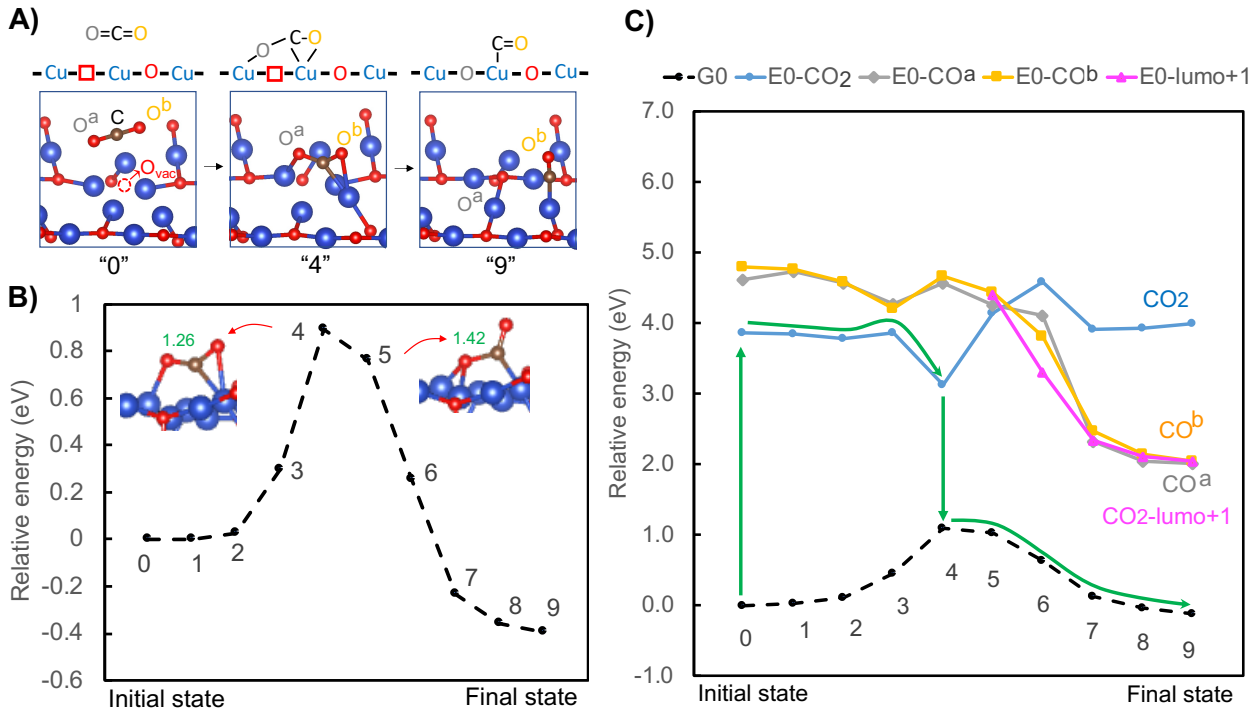


Figure 3.2.1 The CO_2 dissociation on 111-Ores-Ovac. *(**A**) Configurations of the initial state (image 0), the transition state (image 4), the final state (image 9), and their corresponding schematic sketches. The two oxygen in CO_2 is labeled as a and b for distinguishment. (**B**) Ground-state energy profile calculated over ten images (indexed 0 to 9) with VASP. The C-O^a bond length is marked in green (Unit Å). (**C**) Energy profile at excited states, when an electron is added into the LUMO of CO_2 (blue, E0-CO_2), the first available antibonding state of C-O^a bond (gray, E0-CO^a) or C-O^b bond (orange, E0-CO^b), which are compared with the ground state (black dashed, G0); all calculated by GPAW. The magenta solid line (E0-lumo+1) is included to illustrate the case when the electron is added into the LUMO+1 of CO_2 from image 5 to 9.*

First, we investigate the ground-state energy profile of CO_2 dissociation on oxygen-deficient surfaces. The configurations at the initial, the transition, and the final state of CO_2 dissociation on oxygen-deficient surfaces are shown in Figure 3.2.1A. The adsorption energy of CO_2 on these oxygen-deficient surfaces ranges from -0.2 to -0.3 eV, lower than that on the ideal (111) surface by 0.3 to 0.4 eV[38]. Upon adsorption on an oxygen-deficient surface, CO_2 can form a radical anion owing to the excess electrons carried by the oxygen vacancy as suggested in the literature.[43, 81] The oxygen vacancy also increases the optical absorption coefficient of Cu_2O in the range of visible light (Figure A2.1 to A2.3 of the Supplementary Information). Specifically, the presence of the oxygen vacancy increases the absorption coefficient of Cu_2O at low wavelength range on the (111-Ores) surface, at high wavelength range on the (111-VCu) surface, and the whole wavelength range of visible light on the (110) surface. The pristine (111) surface has unsaturated Cu atoms, namely Cu_{us}, the number of which increases when oxygen vacancies are formed. These Cu atoms associated with an oxygen vacancy are denoted as Cu_{Ovac} (Figure A2.4). When CO_2 adsorbs on the (111-Ores-Ovac) surface, CO_2 is stretched by these Cu_{Ovac} atoms, and then dissociates to fill the oxygen vacancy and forms CO (Figure 3.2.1A). Since there are no Cu_{us} atoms on the (111-VCu-Ovac) surface, CO_2 can only be stretched by Cu_{Ovac} atoms on this surface (Figure 3.2.2A). At the final state, CO absorbs at the Cu vacancy on the (111-VCu-Ovac). Similarly, oxygen generated through CO_2 dissociation can heal the oxygen vacancy of the (110-CuO) surface as shown in Figure 3.2.3A.

The energy diagrams along the reaction pathway of CO_2 dissociation on the oxygen-deficient surfaces are shown in Figure 3.2.1B, 2B, and 3B. Despite CO_2 dissociation being endothermic by 1.4 eV on the pristine (111) facet, we find that oxygen vacancies can reduce this reaction energy and render a value of -0.8 eV on the (111-Ores-Ovac) surface. On the (110-CuO-

Ovac) and (111-VCu-Ovac) facets the reaction is endothermic by 0.4 and 0.9 eV, respectively. As a result, a much lower intrinsic activation energy for CO_2 dissociation (*i.e.,* 1.1 to 1.3 eV) was obtained on these oxygen-deficient surfaces, compared to 3.2 eV reported on the pristine surfaces.[75] The presence of oxygen vacancies can thus promote CO_2 dissociation on the Cu_2O surfaces.

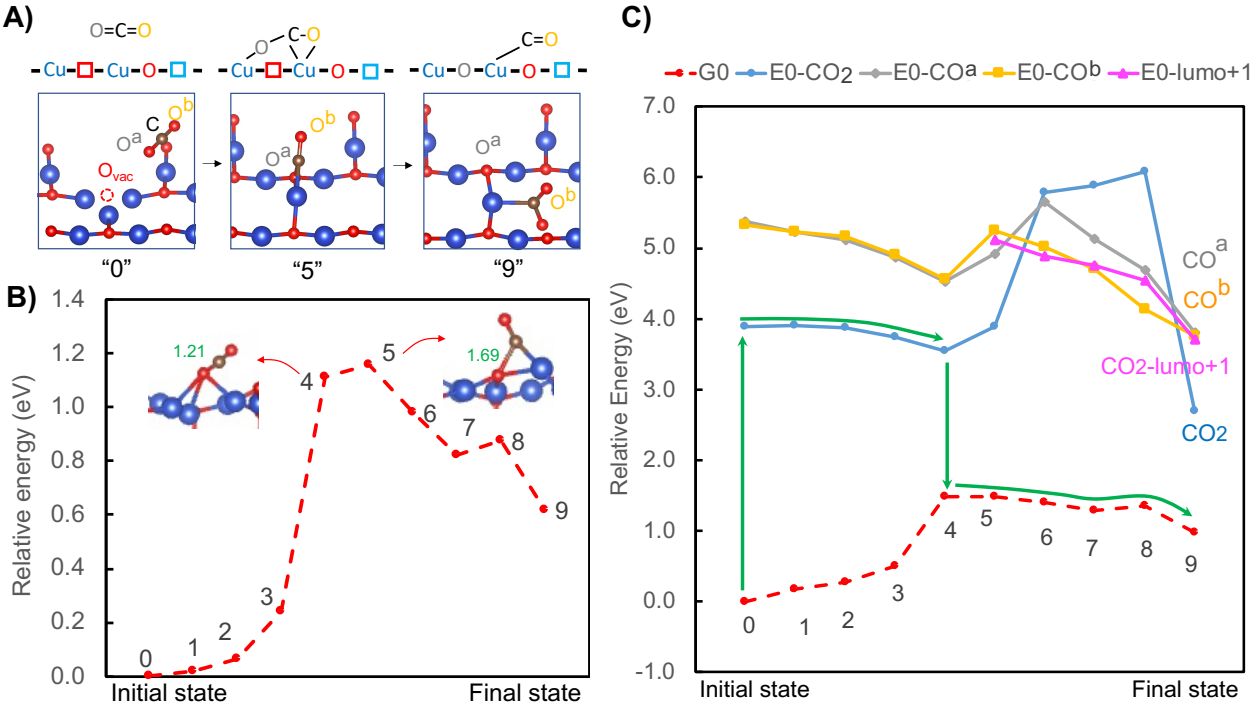


Figure 3.2.2 The CO_2 dissociation on 111-VCu-Ovac. ***(A)*** *Configuration of the initial state (image 0), transition state (image 5), final state (image 9) and their corresponding schematic sketch.* ***(B)*** *Energy profile at the ground-state calculated in ten images (indexed 0 to 9) with VASP. The C-O^a bond length is marked in green (Unit Å)* ***(C)*** *Energy profiles at excited states when an electron is added into the LUMO of CO_2 (blue, E0-CO_2), the first available antibonding state of C-O^a bond (gray, E0-CO^a) or C-O^b bond (orange, E0-CO^b), which are compared with the ground state (red dashed, G0); all calculated by GPAW. The magenta solid line (E0-lumo+1) is included to illustrate the case when the electron is added into the LUMO+1 of CO_2 from image 5 to 9.*

The corresponding excited-state reaction energy profiles are then investigated as shown in Figure 3.2.1C, 2C, and 3C. Prior to CO_2 adsorption, the two excess electrons at the oxygen vacancy occupy states which resonant with the valence band of Cu_2O and create an empty localized defect state about 1.6 eV above the valence band maximum.[82] Upon adsorption, the CO_2 accepts one of the two excess electrons from the oxygen vacancy, as a result of the hybridization between CO_2 and the Cu_2O surfaces evidenced by the broadened orbitals in Figure 3.2.4. This excess electron is transferred to the lowest unoccupied molecular orbital (LUMO) of CO_2, destabilizing the C-O bond. Therefore, the barrier of CO_2 dissociation decreases at the ground state.

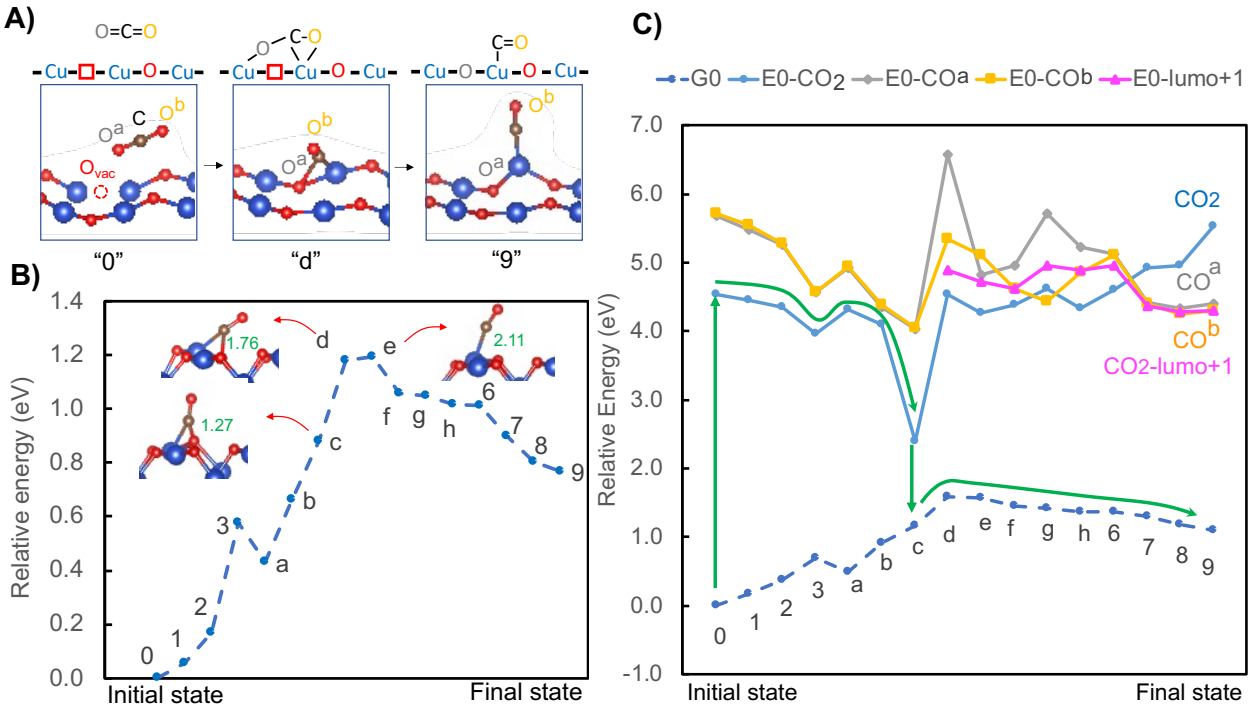


Figure 3.2.3 The CO_2 dissociation on 110-CuO-Ovac. ***(A)*** *Configuration of the initial state (image 0), the transition state (image d) and the final state (image 9) with their corresponding schematic sketch* ***(B)*** *Ground-state energy profile calculated by VASP. The initially selected images (0-9) were further expanded between image 4 and 5 to form additional eight images (a-h). The C-O^a bond length is marked in green (Unit Å)* ***(C)*** *Energy profile at excited states when an*

electron is added into the LUMO of CO_2 (blue, E0-CO_2), the first available antibonding state of C-O^a bond (gray, E0-CO^a) or C-O^b bond (orange, E0-CO^b), which are compared with the ground state (blue dashed, G0); all calculated by GPAW. The magenta solid line (E0-lumo+1) is included to illustrate the case when the electron is added into the LUMO+1 of CO_2 from image d to 9.

Under the illumination condition, photo-excited electrons with high kinetic energy can populate more available antibonding states of CO_2 (Scheme 1). These highly energetic electrons together with the electron originally from oxygen vacancies can occupy a significant portion of the antibonding states of CO_2 and completely eliminate the barrier of its dissociation over (111-Ores-Ovac) or only require energy of 0.1 to 0.3 eV in case of other two facets.

Specifically, over the (111-Ores-Ovac) facet (Figure 3.2.1C), the excited-state energy profile is downhill toward an energy minimum (image 4) when an electron is excited from the Fermi level into the partially occupied LUMO of the adsorbed CO_2. At the transition state (image 4) on the (111-Ores-Ovac) surface the C-O^a bond is stretched to 1.26 Å and the LUMO of CO_2 is still partially unoccupied (Figure 3.2.1B and Figure 3.2.4A). Consequently, electron excitation into the LUMO of CO_2 at this stage is still favorable following the reaction path until the transition state, manifested by a downhill energy profile at this excited state. Similarly, in the case of the (111-VCu-Ovac) and the (110-CuO-Ovac) surface, the excited-state energy profile generated through electron excitation to the LUMO of CO_2 reaches minimum when the C-O bond is stretched to ~1.3 Å. Due to the stronger hybridization between CO_2 and the catalyst surface along reaction pathway, the LUMO approaches closer to the Fermi level of the system (Figure 3.2.4). A lower excitation energy is thus required at these intermediate images compared to the initial state. A downhill excited-state energy profile is obtained in the calculations.

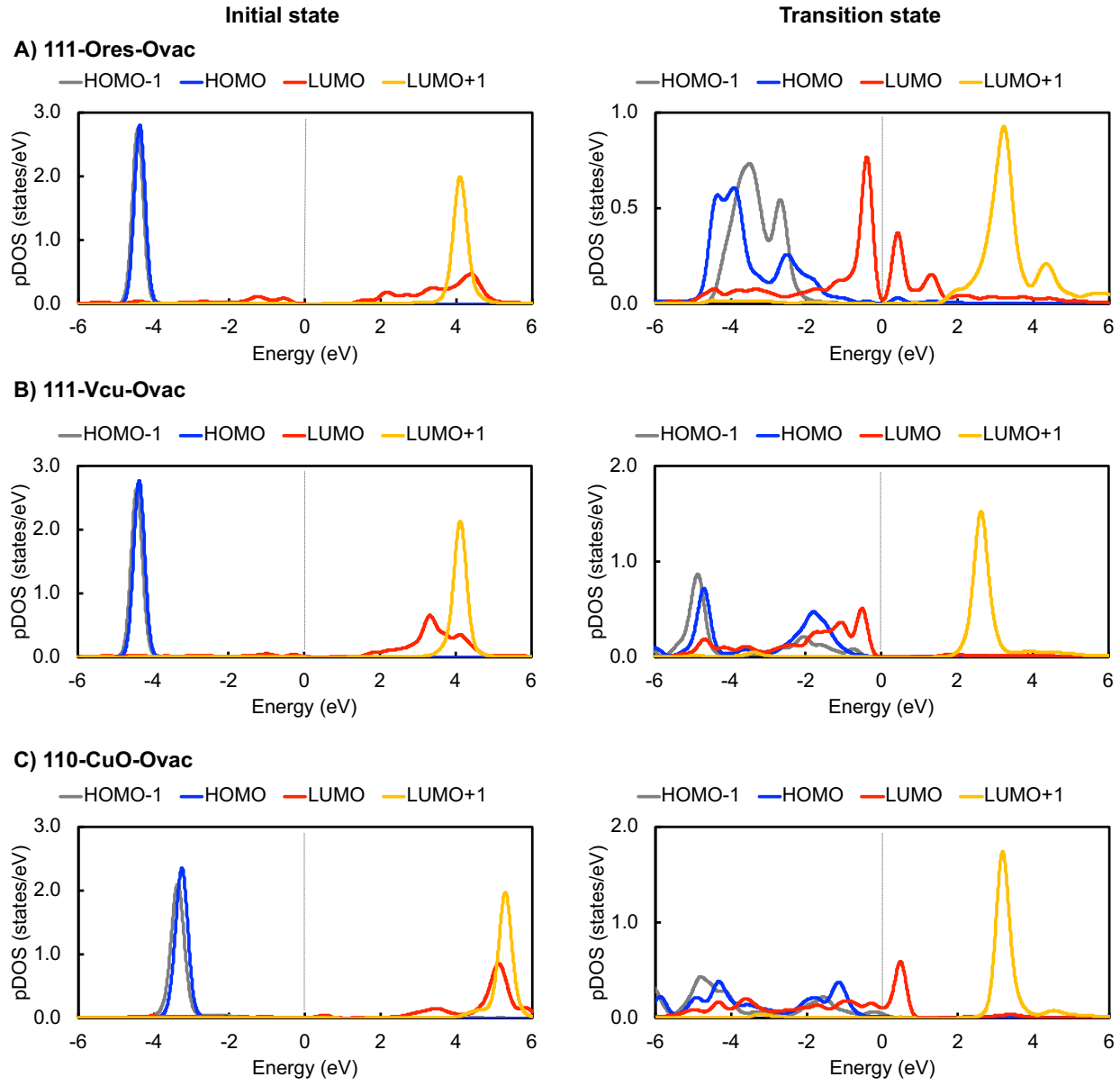


Figure 3.2.4 Projected density of states onto the CO_2 molecular orbitals at the ground level. *The pDOS of CO_2 at the initial states (left) and the transition states (right) on* ***(A)*** *(111-Ores-Ovac),* ***(B)*** *(111-VCu-Ovac), and* ***(C)*** *(110-CuO-Ovac) surface.*

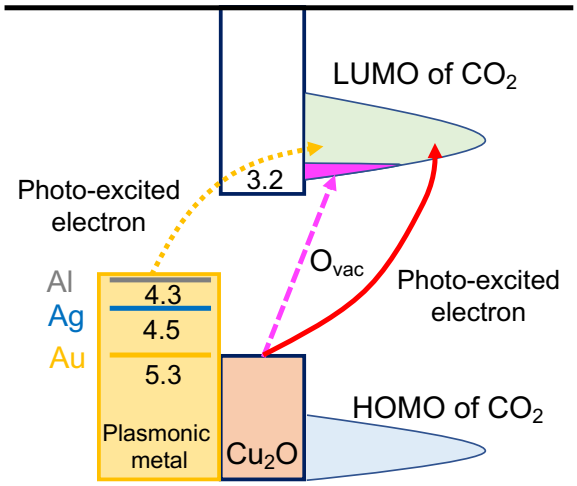
The excited energy profile changed the landscape on all three facets after passing the energy minimum close to the images where the C-O bond is stretched to ~1.3 Å. That is, when the C-O bond is further elongated, the energy along the excited profile increases because it is

unfavorable to add an electron into a fully (Figure 3.2.4B, right panel) or mostly occupied "LUMO" (Figure 3.2.4C, right panel), resulting from a more pronounced interfacial electron transfer from the oxygen vacancy to the molecule (particularly O^a that fills the vacancy as O^{2-}). The C-O bond length at the minimum of the excited-state energy profile (*i.e.,* around 1.21 Å to 1.27 Å) is larger than it at the ground-state minimum (*i.e.,* 1.18 Å). Once the system travels from the initial configuration (image 0) to the bond-breaking configuration (image 4 in Figure 3.2.1 and Figure 3.2.2 or image c in Figure 3.2.3) on the excited-state energy profile (profile of excitation to the LUMO), the system has two options: returning to the ground-state energy profile or staying on the excited-state energy profile. In the latter case, it will most likely move along the profile of excitation to the LUMO+1 since the LUMO is fully occupied and no longer available to accept electrons when the C-O bond breaks. However, to shift from the profile of the LUMO to the LUMO+1, an additional energy of at least 1 eV is required (from image 4 to image 5 in Figure 3.2.1 and Figure 3.2.2 or from image c to image d in Figure 3.2.3). Because further travel along the excited profile needs additional energy, the system can instead return to the ground state at the transition state in the case of the (111-Ores-Ovac) surface or right before crossing the transition state in the case of (111-VCu-Ovac) and (110-CuO-Ovac) surfaces, to complete the reaction indicated by the green arrow in Figure 3.2.1C, 2C, and 3C. Note after passing the transition state and the C-O bond cleavage, it is ambiguous to define the frontier orbital of CO_2 as the original LUMO is now mostly occupied (Figure 3.2.4) due to the transfer of two electrons from the oxygen vacancies to the partially dissociated molecule.

Instead of considering the CO_2 as a whole molecule as it dissociates along the reaction path, we consider excitation within the C-O moiety in the molecule. A lower activation barrier for CO_2 dissociation is observed if an excited electron populates the antibonding state of the C-O

bond; however, the required energy is higher than the excitation to the LUMO of CO_2. This higher energy requirement is not surprising as these antibonding states are above the LUMO of CO_2.

We also find that the excitation energy on the (111) surfaces is lower than the (110) surface (i.e., 3.9 eV compared to 4.5 eV for exciting an electron to LUMO of CO_2). Meanwhile, the CO desorption energy from the surface of (111-Ores) is 1.2 eV, which is 0.8 eV higher than it from the (111-VCu) and (110) surfaces. Therefore, the (111-VCu) facet is probably more favorable for photoreduction of CO_2 due to its lower excitation energy and facile desorption of CO.



Scheme 1*: Illustration of how combination of the excess electrons localized at the oxygen vacancy and photo-excited energetic electrons can populate the unoccupied molecular states and promote the CO_2 dissociation. The mean energy of LUMO with respect to the Cu_2O valence band maximum is 3.6, 3.4 and 4.8 eV for (111-Ores-Ovac), (111-VCu-Ovac) and (110-CuO-Ovac), respectively.*

It is worth to note that the required photo-excitation energy should be lower than the calculated values here that assume excitation within Cu_2O, as the energetic electrons can be generated from a plasmonic metal (Scheme 1). The hybrid plasmonic catalyst has been shown to be a selective and an effective way to drive photo-catalyzed reactions.[1, 3, 4, 10, 21, 62] The required

energy to excite electrons from the plasmonic metal to the CO_2/Cu_2O system can be in the range of visible light by changing the plasmonic metals. Considering the band edges of Cu_2O and the work function of plasmonic metals, the energy of excitation from the metal Fermi level to LUMO of CO_2 adsorbed on the (111) facet can be reduced to ~2.8 or ~ 3.0 eV if Al or Ag is used as the plasmonic metal, respectively (Scheme 1), which is about 1 eV lower than the excitation within Cu_2O because of the higher energy of the Al (and Ag) Fermi level than the valence band edge of Cu_2O.

While the oxygen vacancy can reduce the CO_2 dissociation barrier, the remaining question is if the formation of oxygen vacancy is feasible and how photoexcitation may impact the vacancy formation. Therefore, next we analyze the hydrogen-assisted oxygen vacancy formation in the reverse water-gas shift reaction by investigating the dissociation of H_2 and vacancy formation on the Cu_2O (110) and (111) surfaces (Figure 3.2.5).

Although H_2 weakly adsorbs on the studied surfaces (*i.e.*, 0.2-0.4 eV) as reported in literature[83], we find that the hydrogen molecule can easily dissociate to form two adsorbed H* on both facets of Cu_2O. The energy cost for H_2 dissociation is 0.3 and 0.5 eV on the Cu_2O (110) and (111) surface, respectively. Then, a lattice oxygen reacts with the two H* to form water and creates an oxygen vacancy. The intrinsic activation energy required for the oxygen vacancy formation ranges from 0.9 to 1.1 eV, comparable or slightly lower than the values for CO_2 dissociation at the ground state as discussed above. The desorption of H_2O from the oxygen-deficient surface costs energy in the range of 0.9 to 1.0 eV. However, we notice that, to form water, the surface hydrogen on the (110) surface needs to overcome a barrier, as high as 1.6 eV, to migrate from a lattice oxygen site to a hollow site to interact with a lattice oxygen and another surface H* (Figure 3.2.5B); this diffusion barrier makes the oxygen vacancy formation less favorable on the (110) surface than it

on the (111) surface. Alternatively, the dissociated H* can form surface hydroxyl groups on Cu_2O (110), which can reduce the available oxygen sites for hydrogen binding, resulting in hydrogen dissociation at the hollow sites in the proximity to OH groups (Fig. 5B) and reaction with a lattice oxygen atom to form water and a vacancy. As a result, the availability of hydroxyl groups on the Cu_2O (110) can enhance the oxygen vacancy formation, in agreement with literature[73].

We also investigated the excited-state energy profile of this step by adding an electron into the LUMO of H_2O along the reversed reaction pathway of the oxygen vacancy formation (Figure A2.5 in the Supplementary Information) to examine the role of photo-excited electrons in this step. Our results suggest that the photo-excited electrons do not show any significant impact on the intrinsic activation energy of this reaction (Figure A2.5). However, we cannot exclude the photothermal effects that can help H_2O desorption, which may lead to further enhancement of the photocatalytic performance reported experimentally[73].

It is worth noting that, as an alternate reaction path, the H-assisted CO_2 dissociation on the perfect (111) Cu_2O facet was previously studied[38] and was shown that it required more than 3.2 eV to form a carbonyl group (COOH*) on the Cu_2O (111) surface, while it was easier to form a formate group (HCOO*) and formic acid (HCOOH*). The formic acid formation was also observed in experiments via photoreduction of CO_2 on a core-shell $Cu@Cu_2O$ catalyst.[84] However, in our calculations to decompose formic acid to CO and H_2O, we found that the reaction barrier was close to 4.0 eV; similarly, decomposing the formate group to CO and OH is also very unfavorable. Our calculations thus suggest that H-assisted CO_2 dissociation to CO on Cu_2O is less likely via the formation of formate or carbonyl. Instead, the H-assisted CO_2 dissociation to CO observed in the experiment[22, 73] can be driven by oxygen vacancy formation as discussed above.

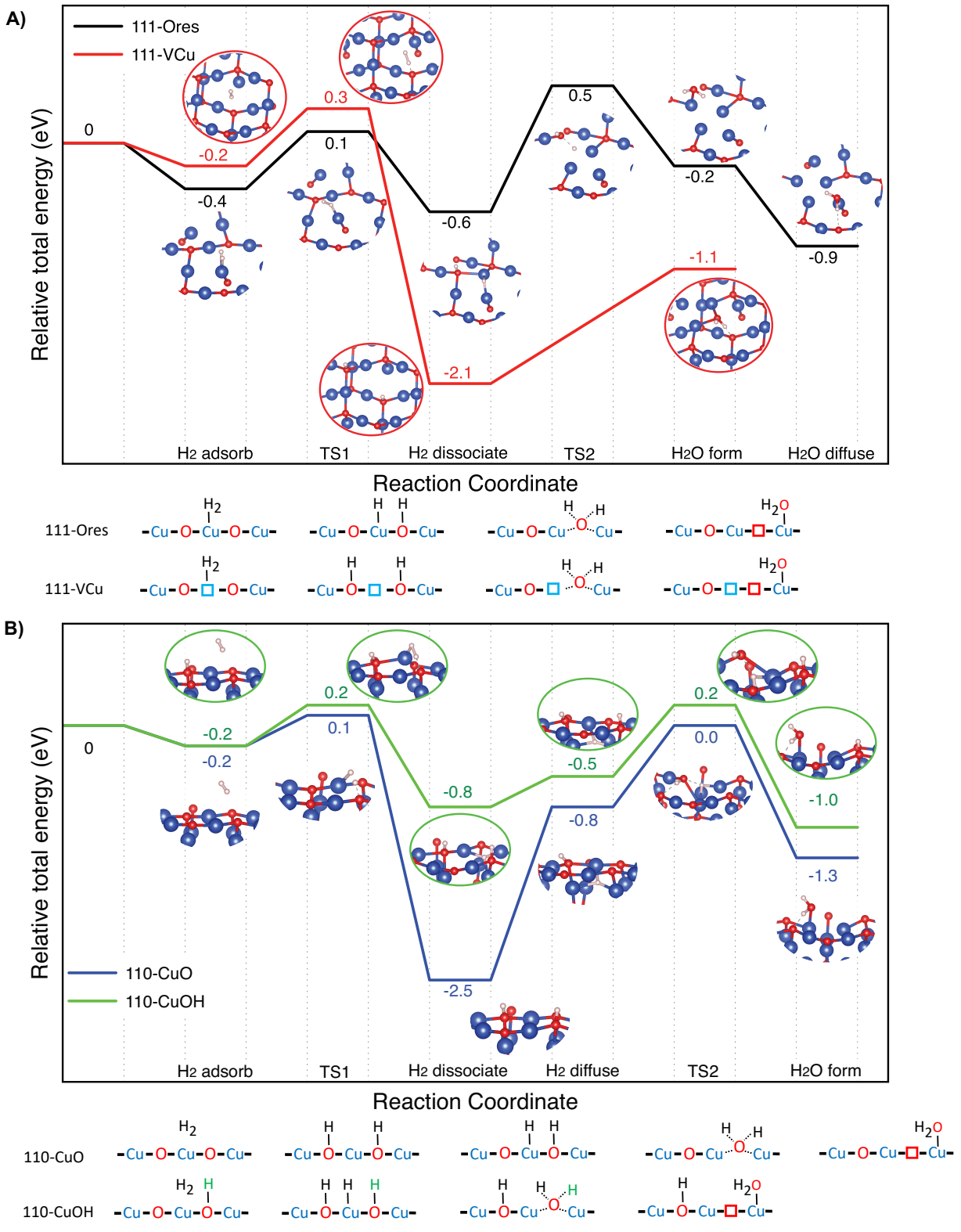


Figure 3.2.5 Energy diagram of oxygen vacancy formation by hydrogenation on Cu_2O. *(A) (111-Ores) and (111-VCu);* ***(B)*** *(110-CuO) and (110-CuOH).*

The Cu_2O surface undergoes reduction by H_2 and oxidation by CO_2, and their balance determines the stability of the catalysts. Previous works on plasmonic and photocatalytic reverse water-gas shift reaction suggested that the Cu_2O catalyst could be stable shown by XPS analysis before and after illumination under reaction conditions[22] and by prolonged catalyst tests.[73] We find in this study that the energetic electrons selectively promote CO_2 reduction to CO at oxygen vacancies, re-oxidizing the catalyst and stabilizing Cu^+ cations. This effect is valuable not only for promoting the reaction kinetics but also stabilizing the catalyst oxidation state.

All calculations reported above are based on a neutral system in which an electron is removed from the Fermi level and introduced into the unoccupied orbital of CO_2 (Figure A2.6A). However, in hybrid systems where a plasmonic metal is coupled with Cu_2O, the photo-generated holes may stay in the plasmonic metal while the energetic electron is positioned into Cu_2O/CO_2. As our calculations only include Cu_2O and the molecule, this scenario essentially means the Cu_2O/molecule system could be temporally charged. We thus calculated the energy profile in the presence of a transient negative charge (i.e., no hole introduced at the Fermi level of Cu_2O).

If an electron is added to the Fermi level, which is dominated by Cu_2O (Figure A2.6C), rather than the LUMO of CO_2, the landscape of the energy profile is similar to the ground-state one with slightly lower intrinsic barriers by less than 0.3 eV (Figure A2.7B). This additional electron is delocalized within Cu_2O and doesn't impact formation of oxygen vacancy (Figure A2.7A). Alternatively, when the additional electron is added into the unoccupied CO_2 orbital (Figure A2.6B), the excited-state energy profile of the charged system is the same as the excited states of the neutral system. Therefore, the discussion above on the role of energetic electrons to eliminate the activation barrier of CO_2 dissociation remains valid, independent on the location of the hole (within Cu_2O or the plasmonic metal). The major difference is the excitation energy;

plasmonic interfacial charge transfer between Ag (or Al) and Cu_2O has a lower excitation energy than excitation within Cu_2O. In addition, the presence of the plasmonic metal/Cu_2O interface provides new channels for charge and energy transfer,[30] and the lifetime of the excited states is determined by the dephasing time in the metal and the dipole-dipole coupling at the interface, the latter of which can be engineered to extend the average lifetime of charge carriers for plasmonic photocatalysis.[55] This similarity of excited-state energy profiles between the charged and neutral system suggests that the chemistry is driven by the energetic electron and that the location of the hole, either in the metal or Cu_2O, is less relevant; however, due to the lack of explicit description of the hole in the plasmonic metal, we cannot capture the role of the hole in determining the dynamics of the electron due to their interaction, which can only be described in time-dependent calculations. A future study to perform real time TDDFT simulations is thus valuable for describing the dynamics of the excited states.

Furthermore, our calculations show that the C-O bond cleavage determines the rate on the pristine Cu_2O surfaces and that, on defective Cu_2O, the activation barriers for CO_2 dissociation are reduced and the reaction is likely limited by generation of surface oxygen vacancy. It will be valuable to compare with experimentally measured reaction order with and without light illumination to determine reaction kinetics under this non-equilibrium condition.

Conclusion

Photoexcited direct dissociation of CO_2 on Cu_2O in the presence of oxygen vacancy were calculated using the linear expansion ΔSCF method. Analysis of the ground-state reaction profile suggests that presence of oxygen vacancy can decrease the reaction energy and activation barrier, but to a limited level. The excited-state calculations show that the plasmonic energetic electron can drive this reaction without overcoming a kinetic barrier by allowing the system to travel on

the excited state to an energy minimum and then decay to the ground-state potential energy surface to finish the transformation. The results also suggest that the (111-VCu) surface is more active for photocatalytic CO_2 conversion than the other two surfaces due to lower excitation energy and CO desorption. We further show that the oxygen vacancy formation on Cu_2O is feasible, especially within the proximity of OH on the surface, independent on the presence of energetic electrons. This result may also indicate a changed reaction order with respect to H_2 and CO_2, corresponding to different rate-determining steps, with and without plasmonic excitation. This work provides a fundamental understanding of how excited electrons together with oxygen vacancy drive the CO_2 reduction on defected Cu_2O and a valuable guideline for photocatalyst design for CO_2 conversion.

Computational method

DFT calculations were performed using the Vienna ab initio simulation package (VASP) version 5.4.1.[14] The exchange-correlation energy was represented using the Perdew-Burke-Ernzerhof (PBE) functional combined with DFT + U.[39, 40] A U−J value of 6.0 eV was used for Cu.[75, 85] The van der Waals (vdW) interaction was included by employing the DFT-D3 dispersion model.[41] We included two types of point defects - oxygen and copper vacancies.[86] The three most stable surfaces including the Cu_2O (111) surface with and without Cu vacancies and the Cu_2O (110) surface were selected to investigate the effect of the catalyst facet. The energies of these surfaces are in good agreement with literature[42] and can be found in Figure A2.8 of the Supplementary Information.

The O-terminated Cu_2O (111) surface, denoted as (111-Ores), was constructed based on a (2 × 2) repeated slab composed of five O-Cu-O layers of Cu_2O (111), same as our previous work.[75] The unsaturated Cu atoms were deleted to form O-terminated Cu_2O (111) with Cu vacancies, denoted as (111-VCu). The CuO-terminated Cu_2O (110), denoted as (110-CuO), was constructed

based on a (2 × 2) repeated slab of 11 layers for the mixed CuO-terminated (110) surface (with five Cu layers and six mixed CuO layers). One oxygen atom was removed from these three surfaces to form the oxygen-deficient surfaces, namely (111-Ores-Ovac), (111-VCu-Ovac), and (110-CuO-Ovac), respectively. The details of surface structures are shown in Figure A2.4 of the Supplementary Information. A 15 Å vacuum was added to separate slabs from their periodic images. Since the difference of the activation energy and reaction energy between the k-points grid of (3×3×1) and (1×1×1) was only around 0.01 eV as reported in our previous work,[75] the k-point grid of (1×1×1) was selected in this study to reduce the computation cost for the excitation energy. The k-point grid of (6×6×1) was selected for calculating the density of states. The energy convergence for electronic relaxation was set to 10^{-6} eV. All atoms were relaxed until the atomic force was less than 0.02 eV/Å with a kinetic energy cutoff of 400 eV. Spin polarization was considered in all calculations. The total energy was extrapolated to 0 K. The transition states were obtained using the nudged elastic band (NEB) and the dimer methods[45, 46] and were further verified by calculating the vibrational frequencies.

The optimized structures along the reaction pathway on the ground state calculated with VASP were adopted to calculate excited states using GPAW version 22.1.0.[15, 16] The exchange-correlation functional, plane-wave cutoff, U-J value, and k-point grid in GPAW were kept the same as in VASP. The linear expansion delta self-consistent field (ΔSCF) approach[12, 13] was used to calculate the energy of the system at excited states instead of the ordinary ΔSCF because it was shown recently that the former could provide very good agreement with experimental excitation energies.[11] The excited electron was modeled to populate the lowest unoccupied molecular orbital (LUMO) of the adsorbate. We also added the excited electron to the lowest unoccupied states of the system instead of the LUMO of the adsorbate (Figure A2.6 in the Supplementary Information).

In addition to the neutral system, one additional electron was manually added into the system to model the charged system (Figure A2.6).[87]

The hybrid structure containing plasmonic metal/Cu_2O provides new channels for charge and energy transfer at the interface, enhancing optical absorption in the Cu_2O layer.[30] Upon photoexcitation, the energetic electrons may populate the Cu_2O layer and the adsorbed molecule through direct or indirect charge transfer or plasmonic resonance energy transfer.[62] Note that in this study we did not model explicitly a photoexcited state in a hybrid structure of metal/Cu_2O/molecules. Because of the complexity of this hybrid structure, the metal was not directly included in the model. Instead, the effect of hot electron generated from the excited metal was simulated by including an additional electron into the semiconductor/adsorbate (Cu_2O/CO_2) system, which is thus negatively charged, assuming the hole staying within the metal (Figure A2.6B, 6C). Alternatively, in the case that the hole remains in Cu_2O, we investigated the excited state by removing an electron from the Fermi level of the Cu_2O/CO_2 system (neutral system) and position it into the antibonding states of the absorbed CO_2 as schematically shown in Figure A2.6A. In both scenarios, the population of an electron in the molecular antibonding state is considered to model the chemistry. Since the excitation energy of the Cu_2O/CO_2 system is directly calculated using ΔSCF method, the excitation energy of the metal/Cu_2O/CO_2 system can be estimated based on the alignment between metal Fermi level and valence band maximum of Cu_2O.

The absorption coefficient is calculated by the following relation:[88]

$$\alpha = \frac{4\pi\kappa}{\lambda} = \frac{2\sqrt{2}\pi E}{hc}\left((\epsilon_1^2 + \epsilon_2^2)^{\frac{1}{2}} - \epsilon_1\right)^{\frac{1}{2}}$$

where ϵ_1 and ϵ_2 are the calculated real and imaginary parts of the dielectric constant, and E is the corresponding energy calculated by the PBE+U functional.

Acknowledgement

The computations were performed at the OU Supercomputing Center for Education & Research and the National Energy Research Scientific Computing Center (NERSC), a U.S. Department of Energy Office of Science User Facility, and were supported by the U.S. Department of Energy, Basic Energy Sciences, Chemical Sciences, Geosciences, and Biosciences Division, Condensed Phase and Interfacial Molecular Science (Grant DE-SC0020300).

Chapter 4: The hybrid plasmonic catalyst between the plasmonic metal and zeolite

4.1. A first-principles study of the interaction between molecules and Lewis acid zeolites manipulated by injection of energized charge

This chapter is based on a publication in Industrial & Engineering Research. Complete article and supplementary material can be found using the citation: Tien Le, Bin Wang, First-Principles Study of Interaction between Molecules and Lewis Acid Zeolites Manipulated by Injection of Energized Charge Carriers, Ind. Eng. Chem. Res. 2021, 60, 14124−14133.

Abstract

Metal dopants in Lewis acid zeolites can be applied to manipulate the interaction between the active sites and molecular reactants. However, only few elements can be introduced into the zeolite framework to generate strong Lewis acid sites. In this study, we propose an alternative approach to tune the interaction between zeolite and molecules by introducing energized charge carriers that are photo-excited in a complex of plasmonic metal and zeolites. Through density functional theory (DFT) calculations, we show that, while the energized electrons do not impact adsorption of ammonia, which is used as a probe molecule, on Zr- and Si-BEA, its heat of adsorption can be reduced up to 60% on Sn-BEA and 20% on Ti-BEA, respectively, because of the localized population of the electrons at the Sn and Ti center. This most pronounced effect in Sn-BEA is attributed to the Sn-induced mid-gap states and the strong electronegativity of Sn atoms. In contrast, the energized holes can strengthen the interaction between zeolites and ammonia by at least 10%. Particularly, if an energized hole is present in the system, the heat of adsorption of ammonia within Si-BEA can increase three-fold, shifting from weak to moderate interaction. We find that, similar to closed sites, the effect of energized charge carriers can also be

extended to open sites of Lewis acid zeolites. Our study provides the fundamental insights for unlocking the potentials of integrating plasmonic metals with zeolites and brings an additional degree of control to tune the interfacial interaction.

Introduction

Lewis acid zeolites have received considerable interest in catalysis, particularly in the field of biomass conversion.[89-93] They can catalyze a variety of reactions such as the oxidation reaction, isomerization, hydride transfer, aldol condensation, dehydration, esterification, and Diels-Alder reaction of biomass-derived molecules.[89, 92] Lewis acid zeolites show a high capability to activate the hydroxyl and carbonyl groups and high resistance to deactivation in the presence of acids compared to solid base catalysts.[94] If the nature of zeolite is modified to be more hydrophobic, thereby reducing the competing adsorption of water with reactants for active sites, the Lewis acid zeolites can effectively catalyze reactions even in an aqueous phase.[90, 93-95] This type of zeolite is normally synthesized by substituting Si by other tetravalent metal heteroatoms (M^{4+}). Despite the neutrality of the total system, the differences in the electronegativities of T-atoms create the electron deficiency at the active metal centers, allowing them to act as Lewis acid sites.[89]

In acid-catalyzed reactions, the reaction kinetics is determined by the strength of the acid sites where reactants/intermediates adsorb.[96, 97] In these reactions, the Lewis acid sites, acting as an electron acceptor, activate the reactants by accepting electrons and polarizing the molecules. It is also well known that the Sabatier principle is normally applied in heterogeneous catalysis.[89] According to this principle, generally, the stronger the acid site, the lower the reaction barrier for activating the reactants. However, if the desorption of products/intermediates determines the reaction kinetics, the strong binding could instead inhibit the reaction.[89, 98] Tuning the interaction

of the reactants, intermediates, and products with the Lewis acid site is thus valuable for enhancing the catalyst activity. One of the common strategies in acid catalysis is to introduce different metal dopants into the zeolite framework to manipulate the electronegativity of the T-sites, the local coordination, the flexibility of active sites in the zeolite lattice, and the charge transfer process with molecules.[89, 99, 100] For example, instead of Ti and Zr, using Sn as a metal dopant could significantly increase the catalyst activity in Baeyer–Villiger oxidation (BVO) or Meerwein–Ponndorf–Verley (MPV) reduction.[101-103] Compared to Ti and Zr, the higher acidity of Sn enhances the interaction between the carbonyl group and the Lewis acid site, favoring the polarization to activate the carbonyl group over competed adsorption of other species such as H_2O_2. In contrast, in epoxidation reactions, H_2O_2 adsorbs first,[104] and its interaction with the Lewis acid site is important for promoting the charge transfer from occupied orbitals of H_2O_2 to unoccupied orbitals of the Lewis acid site. Thus, with suitable energy of the lowest unoccupied molecular orbital (LUMO), Ti-BEA shows an outstanding performance, better than Sn- or Zr-BEA, for epoxidation reactions.[89, 102] Based on Mulliken electronegativity and pyridine ^{15}N MAS NMR chemical shift, Román and co-workers reported the trend of the Lewis acid strength as Sn > Ta > Nb > Zr ≥Hf > Ti.[105] Bregante and co-workers investigated epoxidation of cyclohexene in BEA and have shown that the activation barriers is strongly correlated to the adsorption energy of a probing molecule (CD_3CN) and depends on the capability of the metal center to pull electron density from the oxygen intermediates manifested by the ligand to metal charge transfer energies; the trend was reported to be the following order: Ti > Nb > Ta > Zr > Hf.[97, 106] The exact activity and selectivity may depend on the type of reactions and should be determined collectively by the acid strength and the local reaction environment.[89, 92, 97] Many Lewis acid zeolites with different framework and heteroatoms have been synthesized and tested, but only a handful of elements such as Ti, Hf, Zr, Nb, Ta, W

and Sn can be incorporated into zeolite to create strong Lewis acid sites,[89, 92, 97] limiting the versatility of the Lewis acid catalysis.

Here, we propose an alternate approach to manipulate the interaction of reactants with zeolite by integrating plasmonic nanoparticles with zeolite to form a hybrid plasmonic complex. Comparing to other non-porous materials, such as transition metals that are normally used in plasmonic catalysis, this combination can utilize the exceptional catalytic properties of the microporous zeolite such as the shape and size selectivity, the confinement effect to stabilize the intermediates and the transition state, and its dielectric properties. Different from a conventional heterogeneous catalyst, this combination takes advantage of the local surface plasmon resonance (LSPR) of plasmonic nanoparticles as a driving source for reactions.[3, 4, 8, 107-111] Some studies have reported that the confined environment of zeolite can enhance the luminesce of metal-clusters embedded in zeolite[112-114] and the metal active sites in zeolites can facilitate the thermal-driven epoxidation reaction.[115, 116] However, the possibility of applying this metal-zeolite complex to catalyze photo-included reactions remains to be explored. In principle, if the photoexcited carriers can efficiently populate the catalyst and the molecule, they can induce molecular motion and accelerate the chemical reactions.[3, 4, 8, 12, 20, 75] Population of the highly energic carriers into the Lewis acid sites can also vary the chemical nature of the metal dopants and their chemical environment, altering the interaction between molecules and the catalyst. Integrating the plasmonic nanoparticle with zeolite can thus bring a new degree of control to manipulate the catalyst activity.

Specifically, in this study, we apply DFT calculations to test this hypothesis by investigating the interaction between molecules and zeolites in the presence of highly energetic

charge carriers. Our study was conducted on three widely used Lewis acid zeolites (Sn-, Zr-, and Ti-BEA) and the pure Si-BEA, using NH_3 as the probe molecule. We find that Sn-BEA can be a promising candidate for tuning the interaction between molecules and zeolites by the energetic electrons, followed by Ti-BEA. The injected electron can significantly reduce the heat of adsorption of NH_3 on Sn-BEA by more than 60% and by 17% on Ti-BEA, respectively, while there is no remarkable change observed on Zr-and Si-BEA. The mid-gap states on Sn- and Ti-BEA help to localize electrons on the active sites; this electron localization decreases the interaction between molecules and zeolites by reducing the ligand to metal charge transfer. Unlike the significant impact of adding the energized electrons into M-BEA, we find that adding holes into Lewis acid zeolite only produces a moderate increase of the heat of adsorption, around 10% for Zr- and Sn-BEA and 30% for Ti-BEA, respectively. However, a much stronger effect could be observed if the highest occupied molecular orbital (HOMO) of adsorbed molecules is close to the Fermi level as in the case of Si-BEA. In addition, we find that, besides the effect of electrons/holes in altering the interaction between molecules and the closed sites in M-BEA, the energized charge carriers can also manipulate the interaction between molecules and open sites. In terms of the practical aspects of how to integrate the plasmonic metal with the zeolite and drive the charge localization, we show that it is feasible with a required photon energy in the range from visible to near UV.

Computational Method

DFT calculations were performed using the VASP package[14]. The exchange-correlation functional PBE (Perdew-Burke-Ernzerhof)[39] was used. The DFT-D3[41] dispersion model was employed to include the van der Waals (VDW) interactions. The model was constructed based on a beta unit cell including 64 Si and 128 O atoms (Si-BEA). One of Si atoms was substituted by

one Sn, Zr or Ti atom to form Sn-, Zr- and Ti-BEA, respectively. The lattice constants of the unit cell were fixed using the experimental lattice parameters (a = 17.829Å, b = 17.828 Å and c = 14.671 Å [117]) in all calculations. The energy convergence for electronic relaxation was set to 10^{-6} eV. All atoms were relaxed until the atomic force was < 0.02 eV/Å with a kinetic energy cutoff of 400 eV. The optimized configuration from PBE-D3 was then used in the HSE (Heyd–Scuseria–Ernzerhof)[47] hybrid functional calculations, without further structural relaxation, to correct the bandgap.

Here, we model the electrons and holes populated into the zeolite system after surface-plasmon dephasing. We manually added one electron into the systems to model the energized electron; similarly, one electron was removed from the systems to investigate the effect of the hole on the Lewis acid sites. The Bader charge analysis[51] was applied to analyze the charge density difference before and after adsorption or before and after charge injection.

The adsorption energies were calculated as the difference in the energy between adsorbed state and isolated species:

$$E_{ads} = E_{Z-NH_3} - E_Z - E_{NH_3} \quad (1)$$

Where the three terms on the right side of the equation are the total energies of the NH_3 adsorbed on zeolite (Z-NH_3), zeolite (Z), and NH_3, respectively. The relative electron affinities were calculated as the difference in the energy between the neutral state of zeolite and the anion state (Z^-):

$$EA = E_Z - E_{(Z^-)} \quad (2)$$

The relative ionization energies were calculated as the difference in the energy between the cation state (Z^+) and the neutral state of zeolite:

$$IP = E_{(Z^+)} - E_Z \quad (3)$$

The bandgaps E_g were obtained as follows:

$$E_g = IP - EA \tag{4}$$

The electron density difference was calculated using following formula:

$$\Delta\rho = \rho_{Z-NH_3}^{(+/-)} - \rho_{Z^{(+/-)}} - \rho_{NH_3} \tag{5}$$

Where the sign (+/-) is the corresponding state of the system with a positive and negative charge, respectively; zeolite and NH_3 are fixed in their optimized positions in Z-$NH_3^{(+/-)}$ for the charge analysis.

The electrophilic Fukui functions f_i^+ and nucleophilic Fukui functions f_i^- [103, 118] were calculated as follows:

$$f_i^+ = q_i^{N+1} - q_i^N \tag{6}$$

$$f_i^- = q_i^{N-1} - q_i^N \tag{7}$$

Where q is obtained through the Bader charge analysis and N is the total number of electrons in the zeolite at the neutral state.

The mean square deviation from regular tetrahedron angle (O-M-O angle) of M-BEA was calculated as follows[119]:

$$\theta = \sqrt{\frac{1}{6}\sum_{i=1}^{6}(\alpha_i - \bar{\alpha})^2} \tag{8}$$

Where α_i is the ith (O-M-O) angle and $\bar{\alpha}$ is the average of the (O-M-O) angles.

Results and discussion

The electron-hole pair in the plasmonic nanoparticles can be generated via different mechanisms such as intraband or interband excitation.[8] Nonetheless, the decay rate is ultrafast, ~10 femtoseconds on metallic nanoparticles,[4] or < 300 femtoseconds if the highly energetic charge carriers are injected into semiconductors.[120] Despite the short lifetime, the energized carriers can

trigger electronic or vibrational excitation of adsorbed molecules, leading to the change of the interaction between molecules and catalysts, thereby accelerating the chemical transformation.[3, 8, 110] Here, to investigate the interaction between molecules and reactants, the heat of adsorption is selected as the measure to capture the change of the charge state of the zeolite. Both NH_3 and pyridine have been frequently used in experiments to quantify the acid properties in zeolites.[92] Our calculations show that the heat of adsorption of NH_3 and pyridine on M-BEA has a linear correlation (Figure A3.1). Therefore, only the adsorption of NH_3 was selected as the probe molecule in the following discussion.

At a neutral charge state, the order of adsorption energy of M-BEA increases from Si-BEA to Sn-BEA (Si < Ti < Zr < Sn) as shown in Figure 4.1.1, which agrees with a previous study.[118] We investigated several factors to identify the main factor affecting the adsorption of molecules on M-BEA. In the literature, many properties of M-BEA such as the LUMO energy, absolute hardness, absolute electronegativity, and Fukui functions have been studied to predict the catalyst activities.[102, 118] However, none of them can be the single descriptor for the heat of adsorption of M-BEA due to the complexity of other variables such as the coordination number, the electron back-donation, and the change of electronic level upon interaction with reactants. Recently, the chemical shift of an acid-base pair[105] and the ligand to metal charge transfer energy[106] have been reported as efficient ways to evaluate the Lewis acid character in zeolites. These finding implied the importance of the charge transfer in determining the binding between reactants and zeolites which is also the focus in this study. Considering that the Lewis acid site is normally characterized by the capability of accepting electrons from the Lewis base, we investigated if the electron affinity of the zeolite has correlation with the adsorption energy of NH_3. Figure 4.1.1a shows the relative electron affinity when one electron was added into the system. The relative electron affinity of Sn-

BEA is higher than Zr-BEA, and the relative electron affinity of Ti-BEA is higher than Si-BEA (Figure 4.1.1a). However, the relative electron affinity of Zr- and Si-BEA is similar despite the large difference in the heat of adsorption of NH_3 in these two zeolites, suggesting that the relative electron affinity cannot be the main factor to determine the adsorption energy. We also tried to calculate the electron affinity when adding one pair of electrons into the system, and the observed trend is similar. We find that the relative ionization energy is similar for all four types of M-BEA, suggesting that the valence band maximum of M-BEA is not influenced much by the metal dopant. Neither does the bandgap correlate with the NH_3 adsorption as shown in Figure 4.1.1a.

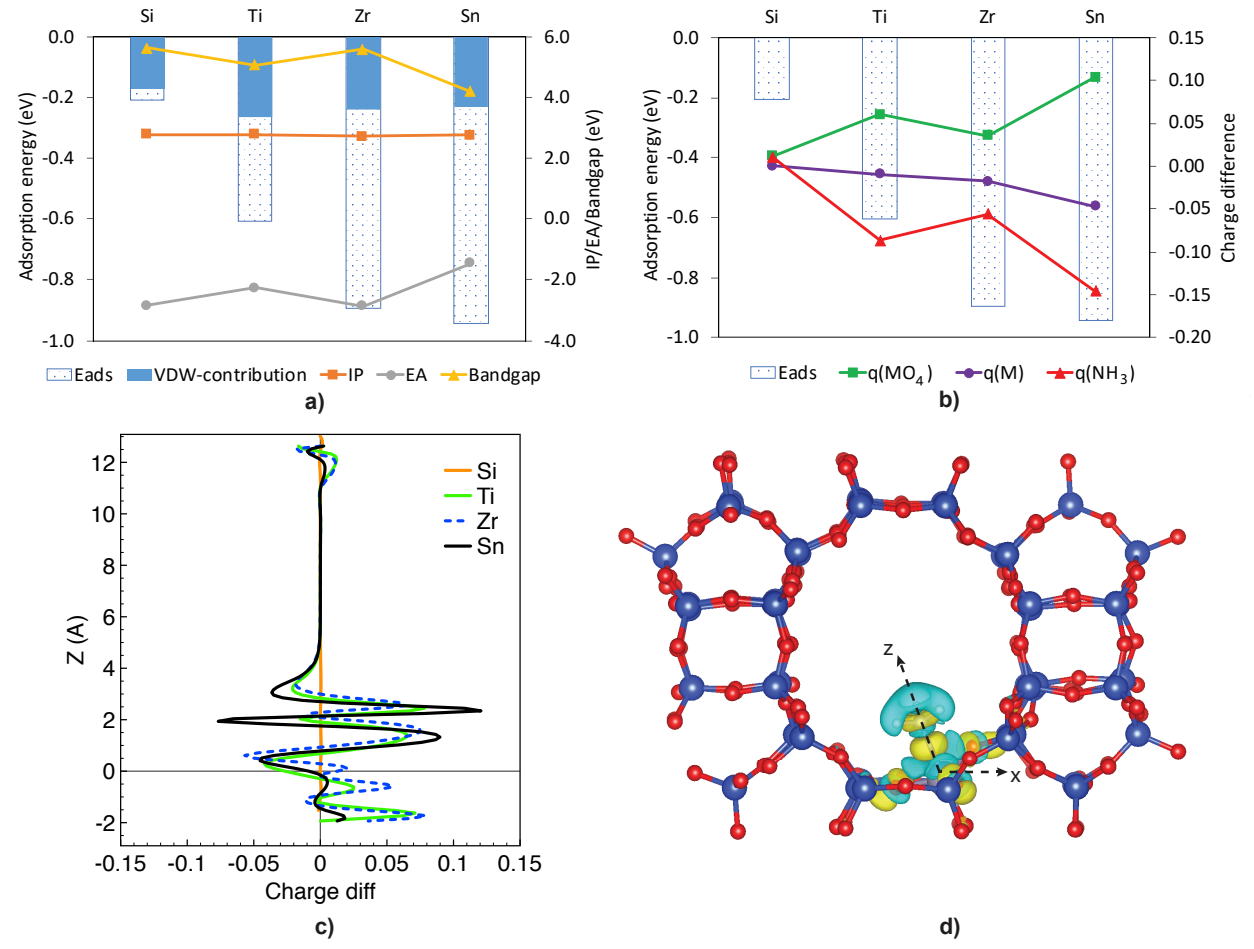


Figure 4.1.1 *Calculations to explore main factors for molecular adsorption. (a) Plot of the adsorption energy of NH_3 on M-BEA together with IP, EA, Bandgap. (b) Plot of the adsorption*

energy of NH_3 on M-BEA with charge density difference before and after NH_3 adsorption of metal – q(M), of metal and 4 oxygen nearby - q(MO_4) and of NH_3 - q(NH_3). (c) Charge redistribution at the interface between the Lewis acid (M-BEA) and NH_3 in z direction. (d) The illustration of the charge redistribution. The blue, red and white balls denote Si, O and H atoms respectively. The cyan and yellow colors denote the withdrawing and accepting of electrons.

Besides the electronic energy, we also investigate the VDW contribution, which is found similar for all four types of M-BEA (Figure 4.1.1a), confirming that VDW interaction is not the main reason for the difference in adsorption energy. It is worth noting that local metal-O_4 tetrahedron is distorted because of the difference in the radius of the metal dopant. We find that neither the volume of metal-O_4 tetrahedron or the average of M-O bond length correlates with the adsorption energy (Figure A3.2). However, we show that the increase of the adsorption energy correlates with increasing of the mean square deviation from a regular tetrahedron angle (O-M-O angle) of M-BEA (Figure A3.2), in agreement with previous reports.[92, 119] Such a correlation may result from the inhomogeneous charge in the metal-O_4 tetrahedron as discussed below.

The analysis of the charge redistribution at the interface between the Lewis acid center and the adsorbate was conducted (Figure 4.1.1c) to reveal the charge transfer upon NH_3 adsorption. We find that the largest charge redistribution occurs on Sn-BEA, followed by Zr- and Ti-BEA, while no charge redistribution is observed on Si-BEA. This is consistent with the order of their heat of adsorption. This charge redistribution is also manifested by the stronger hybridization of NH_3 orbitals with Sn-, Zr-, and Ti-BEA than Si-BEA (Figure A3.3).

The Lewis acid character of zeolite is attributed to the partial positive charge at the metal when it forms 4 covalent bonds with oxygen nearby.[92] The absolute charge density difference in NH_3 (q(NH_3)) and the charge density difference in the metal and the four oxygens nearby (q(MO_4))

before and after NH_3 adsorption are closely matched, as expected. This analysis supports that if electrons are transferred from the Lewis base cannot be fully received by the metal center; the electrons can be delocalized onto the oxygens nearby. However, either $q(NH_3)$ or $q(MO_4)$ does not show a good correlation with the adsorption energy. The Bader charge was then analyzed to investigate the charge density difference on metal dopants before and after NH_3 adsorption (q(M)). Even though the change in charge density of metal centers is small, we find that the greater the change of the charge density of metal centers, the stronger the adsorption energy (Figure 4.1.1b). The adsorption of NH_3 is thus sensitive to the charge carried by the metal dopants (q(M)) in M-BEA; it is, therefore, possible to manipulate the molecular interaction by energized charge carriers that can tune the charge localization at the metal dopants.

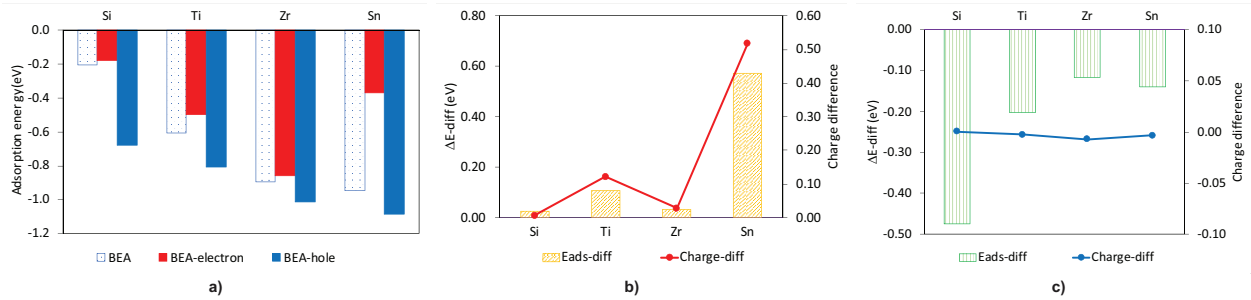


Figure 4.1.2 *Adsorption of NH_3 in M-BEA with an additional electron or a hole. (a) The heat of adsorption of NH_3 on neutral M-BEA (white) compared with values with an added electron (red) and with one removed electron (blue). The relationship between the change of heat of adsorption and the electron localization on metal when (b) one electron is added into M-BEA, and (c) one electron is removed from M-BEA.*

In the following, we investigate the effect of high energetic carriers on NH_3 adsorption, starting with the effect of an additional electron in M-BEA. Figure 4.1.2a shows that when one additional electron is added into the system, the heat of adsorption of NH_3 on M-BEA decreases.

The most significant change is observed on Sn-BEA, with ~60% of the heat of adsorption reduced, followed by Ti-BEA with ~17% reduction of the heat of adsorption, while there is only marginal change on Si- and Zr-BEA. Therefore, the order of the heat of adsorption now changes to Zr > Ti > Sn > Si. We find that the decrease of the heat of adsorption of NH_3 has a good relationship with the localization of the energized electron at the metal site shown by the electrophilic Fukui functions of the metal center (Figure 4.1.2b). More than 50% and 10% of the added electron is localized on the metal center of Sn- and Ti-BEA, respectively. In contrast, almost no change of the charge density is observed on the metal center of Zr- and Si-BEA. The localization of the energized electron can be explained by the projected density of states (PDOS) of metal and SiO_2 at the neutral state. The conduction band of pure SiO_2 form of BEA can be seen from Figure 4.1.3a (starting from ~ 4.5 eV). The mid-gap states below the conduction band of the parent zeolite (from ~ 3.0 eV to ~ 4.5 eV) are featured only on Ti- and Sn-BEA (Figure 4.1.3b and 3d), while the Zr-associated states are merged in this conduction band (Figure 4.1.3c). These mid-gap states introduced by the metal site of Sn- and Ti-BEA can thus host the energized electron, while it tends to be delocalized with the SiO_2 framework in the cases of Zr- and Si-BEA. This larger portion of electron localization at the metal center of Sn-BEA compared to Ti-BEA is attributed to the higher electronegativity of Sn than Ti. With the more electron localized at the metal site, the latter's capability to accept electrons from the Lewis base is reduced; the interaction between the Lewis acid zeolite and the Lewis base (NH_3 in this case) is thus weakened. This argument is supported by the charge redistribution analysis as shown in Figure 4.1.4 and Figure A3.4. We find that the charge redistribution at the ground state (black) and the excited states with the additional electron (red) for Si- and Zr-BEA remain almost unchanged. On the contrary, the charge redistribution for Sn-BEA upon NH_3 adsorption at the excited state with an energized electron (red) decreases

significantly, corresponding to a weakened adsorption. The charge redistribution at the interface between Ti-BEA and NH_3 in the z direction also slightly decreases (Figure A3.4). We also notice that the distortion degree of the MO_4 tetrahedron also alters in the presence of the additional electron. The largest change is again observed in Sn-BEA, followed by Ti-BEA (Table A3.1). Different from the correlation between the heat of adsorption and mean square deviation from the regular tetrahedron angle at the ground states, this structural distortion cannot explain the Ti- and Zr-BEA with an additional electron. This observation suggests that in the presence of an energized electron, the localized charge – an electronic factor – rather than the structural distortion, determines the molecular adsorption.

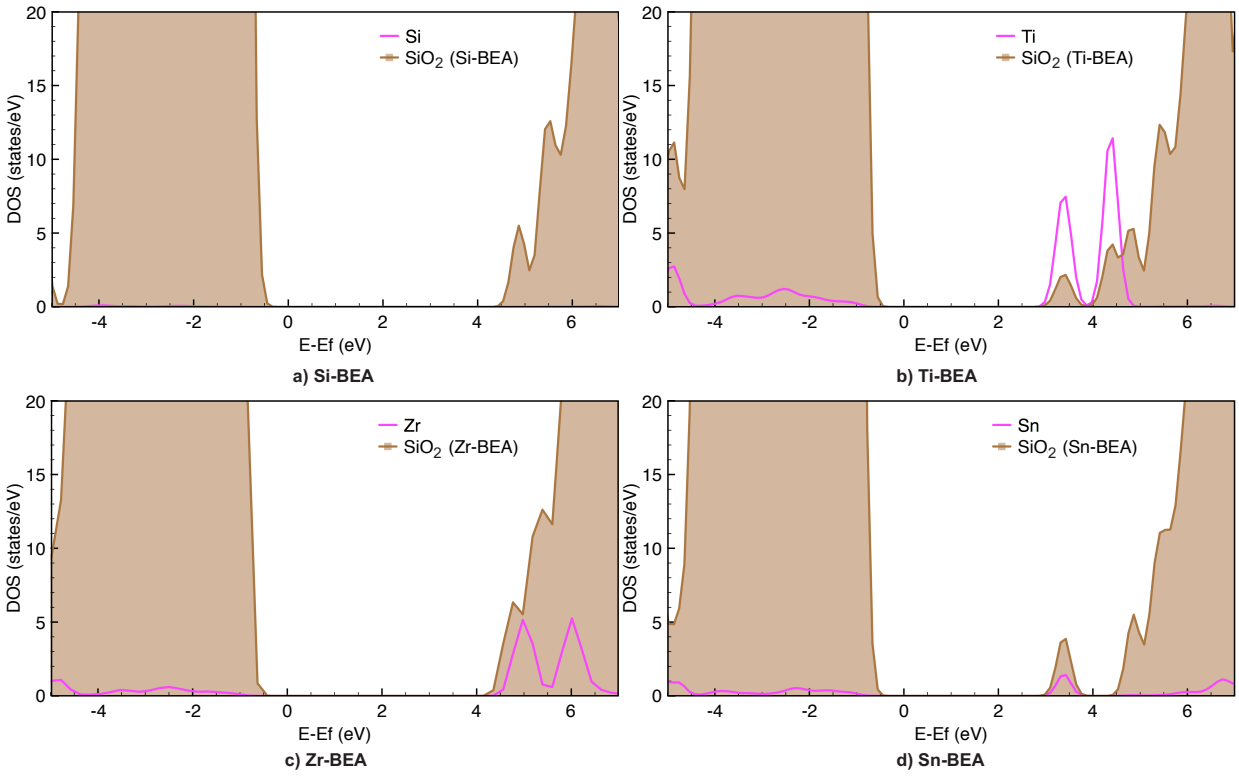


Figure 4.1.3 *PDOS of M-BEA on metal (pink) and on SiO_2 framework (brown) for a) Si-BEA b) Ti-BEA c) Zr-BEA d) Sn-BEA.*

We further investigate the effect of a hole in M-BEA and find that the heat of adsorption of NH_3 on M-BEA can increase by at least 10% under the effect of the hole generated by removing one electron from the system (Figure 4.1.2a). The trend is expected as the hole should in principle increase the Lewis acidity; however, unlike the cases of an injected electron, the increase in the heat of adsorption of NH_3 has a minor relationship with the charge density difference on the metal, shown by the nucleophilic Fukui functions of metal center (Figure 4.1.2c). In fact, the charge density on the metal remains almost unchanged suggesting that the hole does not localize at the metal site; instead, the hole is delocalized within the SiO_2 framework, especially on the four oxygen nearby metal center. It means that introducing the hole into M-BEA creates more capacity to accept electrons at the 4 oxygen nearby, rather than the metal itself. As a result, the interaction between the Lewis base and the Lewis acid zeolite is strengthened to a very limited extent.

The charge redistribution analysis (Figure 4.1.4 and Figure A3.4) was conducted to compare the interaction between zeolite and the probe molecule with and without the effect of the hole. We observed higher charge redistribution on all four types of M-BEA, suggesting stronger interaction between the probe molecule and zeolite. Only a slight increase was observed in the heat of adsorption of Sn-, Zr- and Ti-BEA, but a notable change of the adsorption energy (more than three times) was observed on Si-BEA (Figure 4.1.2c). The weak interaction between NH_3 and Si-BEA leads to this different hole-effect in adsorption. That is, while the electron is mostly withdrawn from the zeolite framework due to the strong hybridization between NH_3 and Sn-, Zr- and Ti-BEA, the weak interaction between NH_3 and Si-BEA and the high HOMO level of NH_3 drives the hole to be localized at the probe molecule NH_3. As a result, NH_3 appears to act more like an NH_3 radical, leading to the increase of the charge redistribution at the interface and the noticeable increase of the heat of adsorption. This noteworthy increase of NH_3 adsorption in Si-

BEA does not change the order of adsorption energy (Si < Ti < Zr < Sn) among the four M-BEA in the presence of an energized hole. However, the hole can increase the interaction between NH_3 with Si-BEA under excitation to be higher than the interaction between NH_3 and Ti-BEA at a neutral condition. In other words, a nearly inert interaction of molecules with Si-BEA can be shifted to a moderate interaction under the effect of a highly energetic hole. This finding also suggests that introducing the highly energetic hole into M-BEA could be beneficial to enhance the weak interaction between reactants and the zeolite if the HOMO of the reactant is close to the Fermi level.

In Lewis acid zeolites, apart from solvents and confining voids, the local configuration of the active sites (i.e., a closed site or an open site) significantly affects the catalyst reactivity.[89] The results shown in Figure 4.1.2 are obtained from calculations of a closed site of M-BEA, which is the Lewis acid before hydration. However, the open site, which is the Lewis acid after hydration, is reported to more active for some reactions such as the glucose isomerization, BVO, and MPVO.[89, 121-123] This enhancement of reactivity is mainly attributed to the higher flexibility of the open site compared to the closed site, the stabilization of kinetic relevant transition states by the open site or even the cooperative participation of the open site in the reaction pathway.[89, 121-123] Here, using Sn-BEA as an example, we also compared the effect of the additional electron and hole on the open site of M-BEA (Figure 4.1.5,Table A3.2 and A3.3). The PDOS analysis reveals the mid-gap states, and the charge density difference analysis show that an additional electron can be localized at the Sn-OH open site. As can be seen from Table A3.2, introducing highly energetic electrons into the open site of Sn-BEA also significantly decreases the heat of adsorption of the zeolite from -0.9 eV to -0.3 eV, and increases the bond length between Sn and N in NH_3 by 0.33 Å. In contrast, the hole only slightly increases of its adsorption energy from -0.9 eV to -1.0 eV,

and the bond length between Sn and N slightly decreases by 0.03 Å. This same conclusion for the effect of charge carriers on the closed sites and open sites of Sn-BEA thus suggests that the interaction between molecules and both an open site and a closed site of M-BEA can be tuned by the highly energetic carriers.

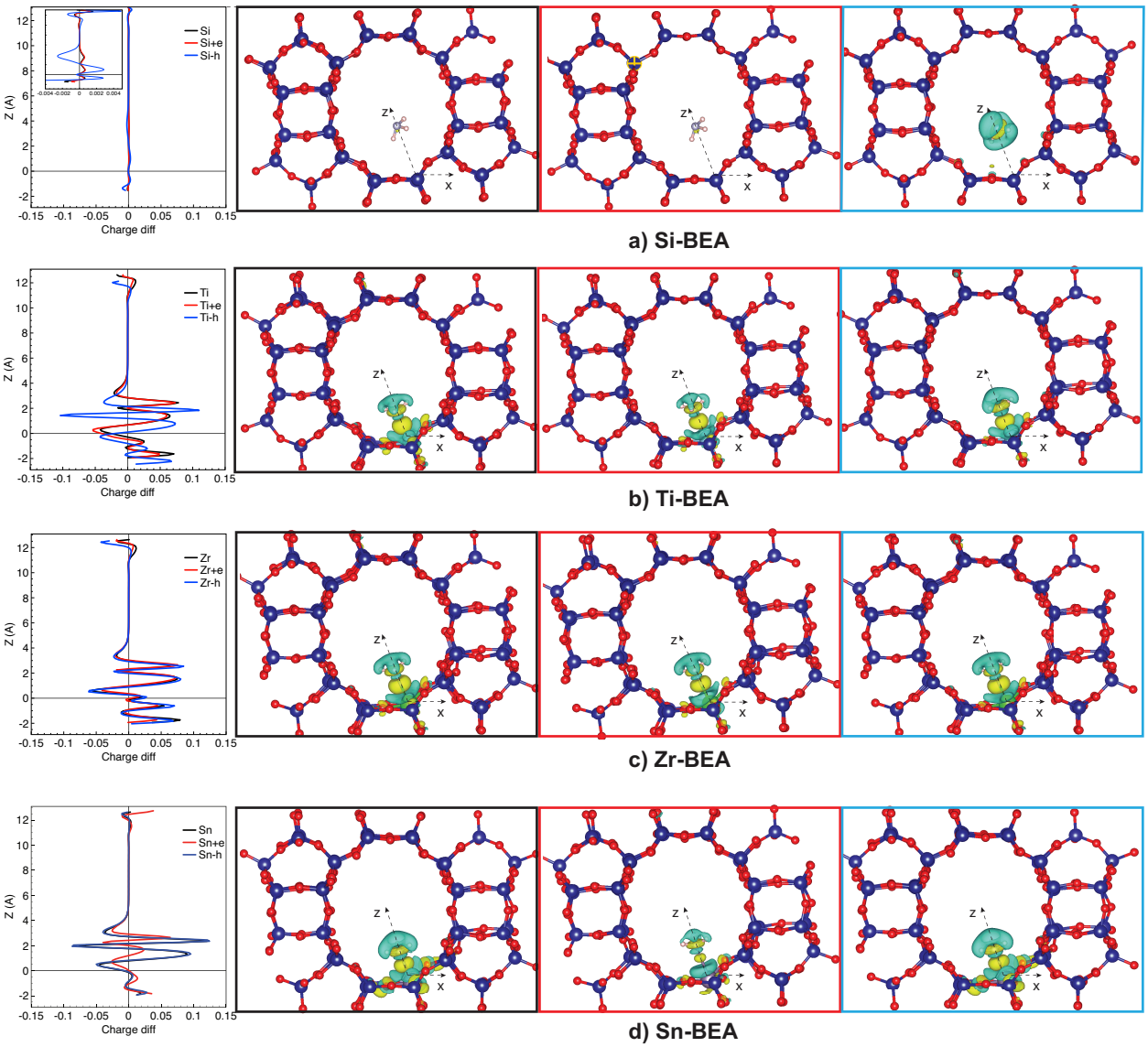


Figure 4.1.4 *Charge redistribution at the interface between NH_3 and M-BEA neutral (black), M-BEA with 1 added electron (red), M-BEA with 1 removed electron (blue) for a) Si-BEA b) Ti-BEA c) Zr-BEA d) Sn-BEA. The blue, red and white balls denote Si, O and H atoms respectively.*

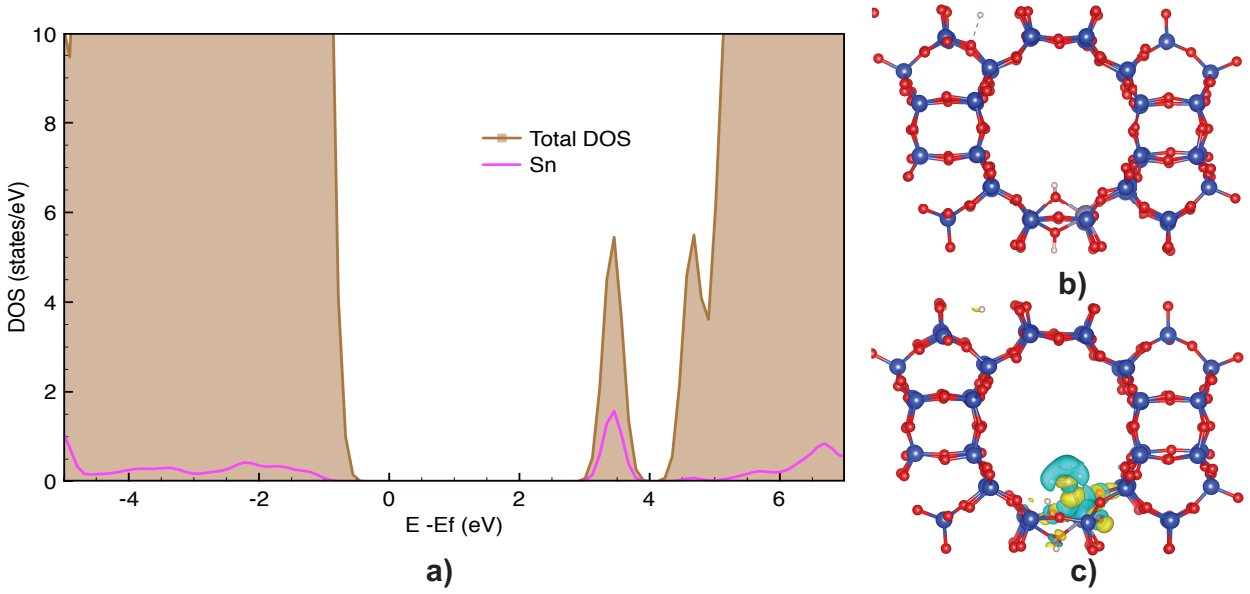


Figure 4.1.5 *a) The total DOS and the PDOS of Sn of the open site configuration shown in (b), the charge redistribution when NH_3 adsorbed on the open site of Sn-BEA (c). The grey, blue, red and white balls denote Zn, Si, O and H atoms respectively.*

The effect of the energized hole and electron on Si-BEA and Sn-BEA were also calculated using the HSE06 hybrid functional to reduce the error of delocalization of electron and correct the bandgap. As shown in Table A3.4, the effect of the injected carriers on the adsorption energy of M-BEA predicted by HSE06 is similar to results from the PBE functional. The bandgap for Si-BEA is 7.4 eV in the hybrid functional calculations, agreeing with reported values in the literature.[124] The corrected bandgap of Sn-BEA is 6.2 eV (Figure 4.1.6). While the valence band maximum of Lewis acid zeolite is composed of the p-orbitals of oxygen and does not strongly rely on the dopant metal, its conduction band minimum depends on the hybridization between unoccupied states of oxygen and the metal.[124] Therefore, the energy cost to introduce a hole into Sn-BEA is similar to that required for Si-BEA, both in the UV regime. Among widely used

plasmonic metals, Au has a higher work function which is expected to have a lower energy cost to induce the energized hole into zeolite compared to Ag, Cu or Al, but the energy cost is still as high as 4.1 eV. Different from the high energy cost to introduce holes, our calculations suggest that the energy of visible light is enough to excite electrons from the plasmonic metal to Sn-BEA due to the presence of the mid-gap states. The required energy for Au to introduce electrons is expected as low as 2.1 eV only, and this value is expected to be further lower if using Ag, Cu or Al as the plasmonic component. In this study, we calculated the bandgap for Sn-BEA with the Sn/Si ratio is 1:64. However, it is shown in the literature[124] that if all Si atoms are replaced by Sn atoms, even if the valence band maximum remain unchanged, the bandgap could be lowered to approximately 3.6 eV by the dominance of the mid-gap states of Sn. This finding thus suggests that increasing the ratio of Sn/Si can reduce the bandgap of Sn-BEA, leading to a lower energy cost for adding an electron into Sn-BEA. We understand there are some challenges that need to be overcome to incorporate a high metal ratio into the zeolite framework in experiments[125]; its success could be a driving force for applying zeolites in plasmon-modulated Lewis acid catalysis.

Finally, we want to mention that introducing the coinage metal cluster into zeolite is feasible. Indeed, there are several experiments successfully integrating the coinage metal cluster with a zeolitic framework such as Au/TS-1 for epoxidation reaction[115, 116] and Ag/FAU or Ag/LTA for high photoluminescent materials.[112-114] With a large bandgap, zeolites are transparent in the range of visible to near UV light. Therefore, the light could access embedded metal particles. This has been demonstrated in the photoluminescence measurement of Ag clusters in commercial parent zeolites.[112, 113] The near-field electromagnetic on plasmonic metal could enhance the energy transfer and density of hot carriers as well.[110, 126] Therefore, the reactivity of the hybrid plasmonic-zeolite complex could be improved if the active site and the molecules are placed within the near

field of the metal cluster. As a result, the shapes and size of both metal clusters and zeolites shall be optimized to ensure the light can reach the plasmonic metal and drive the highly energetic electrons into the molecule/zeolite system.

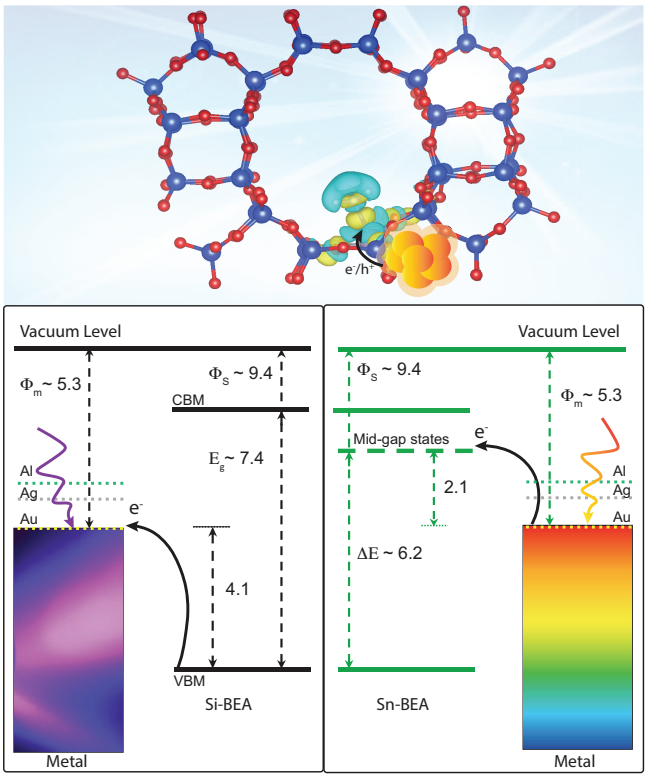


Figure 4.1.6 *Electron excitation to the conduction band edge and mid-gap states in Si-BEA and Sn-BEA. The work function of pure silica form of BEA is obtained from the work function of SiO_2 polymorph of ZSM-5[124], and the work function of Au is taken from literature[58]. Units are eV.*

Conclusion

We perform DFT calculations to investigate the effects of energized carriers on the interaction between molecules and the Lewis acid zeolite. We find that replacing Si atoms in the zeolite framework with Ti and Sn could enable the visible light to excite electrons from plasmonic metal into zeolites. Our results also reveal the significant impact of the energized electrons on the

molecules/catalyst interaction when the mid-gap states can be generated in zeolites. This concept of plasmon-modulated Lewis acid catalysis (PLAC) is thus valuable for tuning the interfacial reaction by either enhancing the molecular adsorption or product desorption. This study offers the opportunity to use highly energetic carriers, generated in plasmonic metal, to tune the zeolite activity for acid-catalyzed reactions.

Acknowledgements

This invited contribution is part of the I&EC Research special issue for the 2021 Class of Influential Researchers. This work was supported by the Department of Energy (Grant No. DE-SC0020300). The DFT calculations were performed using computational resources at the OU Supercomputing Center for Education & Research (OSCER) at the University of Oklahoma and the National Energy Research Scientific Computing Center (NERSC), a U.S. Department of Energy Office of Science User Facility.

4.2. Epoxidation reaction on TS-1

Introduction

Propylene epoxidation is an essential step in industrial polyurethane production. TS-1 has appeared to be a highly effective and stable heterogeneous catalyst for selective oxidations of propylene.[104] Among oxidants, using hydrogen peroxide aqueous is a green option as it produces water as the only byproduct. However, the structure of the active Ti (IV) site for the epoxidation of propylene on TS-1 is still under debate. A previously proposed active site is the defective site in the framework,[127] while recent work claims that the active site is the dinuclear site.[104] By using different types of active sites (Figure 4.2.1), we can test the effect of doping level on charge carrier localization via propylene epoxidation reaction on Lewis acid zeolite.

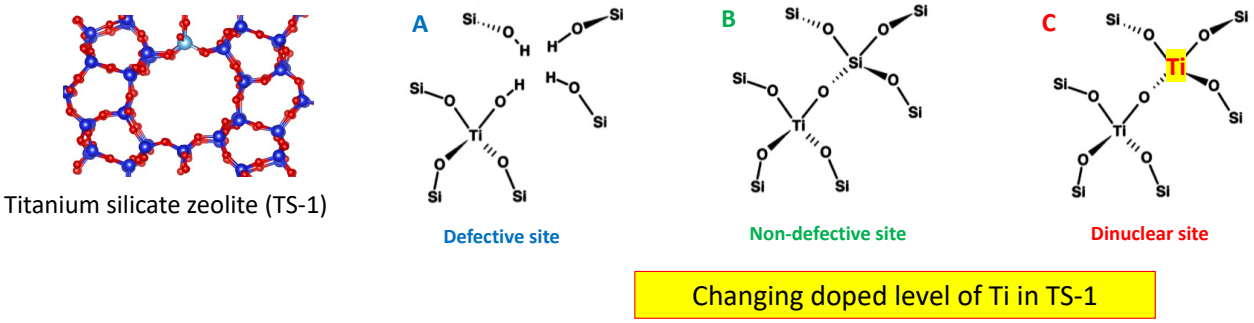


Figure 4.2.1 *Illustration of different doped level of Ti in TS-1*

Results and discussion

As can be seen from Figure 4.2.2, the excited electron easers the barrier of the epoxidation step on the dinuclear site and reduces half of the proton transfer barrier. In contrast, it has a negligible impact on the barrier of epoxidation on the defective site. This difference can be attributed to the charge carrier localization at transition state: only ~6% of the excited electron localized at HOOH in the low doping case, while ~19% the excited electron localized at OOH in the high doping case. As a result, the higher the charge localization, the more significant the impact.

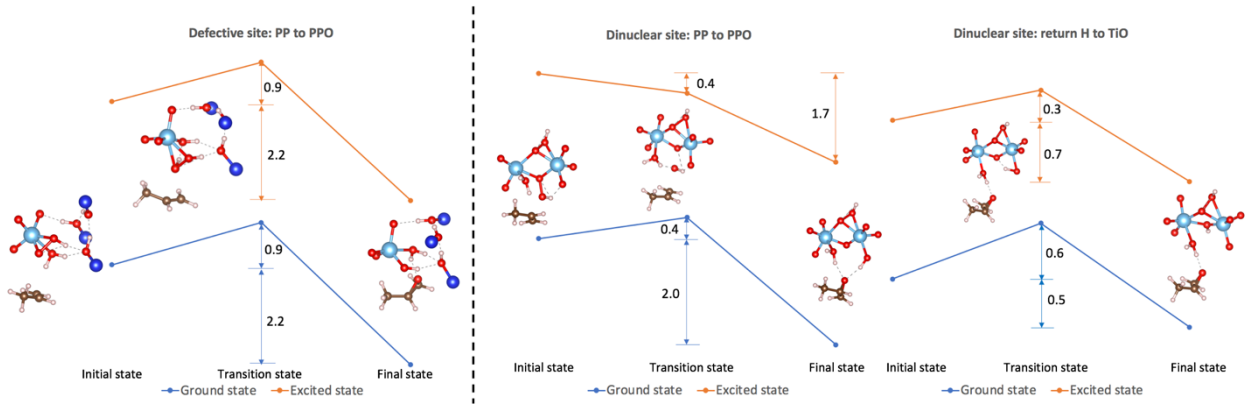


Figure 4.2.2 *Energy diagram of propylene epoxidation at the ground state and the excited state on TS-1.*

Chapter 5: Local enviroment effect induced by solvent on the hybrid plasmonic catalyst

Abstract

Solvent has been shown the effect to the local surface plasmon resonance on metal; however, how solvent affect the interfacial charge transfer on plasmonic catalysis remain to explore. Here, using NH_3 decomposition on Ru-doped Cu surface as an example, we report density functional theory (DFT) calculations, through which we investigate the effect of solvent on the interfacial charge transfer via calculated excitation energy of an electron from HOMO to Fermi level and from Fermi level to LUMO. We found that the H-bond between water and NH_3 can alter the excitation energy, i.e., increasing the excitation energy of the former process while decreasing the excitation energy of the later process due to the shift of HOMO and LUMO level. These effects also observer when the H-bond formed between methanol or phenol and water, but the solvent which has stronger basicity is found to induce larger effect on the excitation energy. In addition, the HOMO-LUMO excitation energy is affected due to the unidentical shift of HOMO compared to LUMO.

Introduction

Plasmonic catalysis has received a lot of interest over last decade due to the potential to active chemical bonds on metal surface by alternative mechanism via non-equilibrium charge carrier instead of traditional heat-induced mechanism.[1, 3, 5, 8, 62, 128] This potential motivates researchers to design a catalyst system that can control the product selectivity than in purely thermal-driven reactions, especially for processes that are typically performed at relatively high temperatures such as dehydrogenations, ammonia synthesis, CO_2 or N_2 reduction, hydrocarbon reforming.[2]

The plasmonic catalysis based on the intensive charge polarization and the amplified near field due to local surface plasmon resonance (LSPR) of the metal nanoparticle. When LSPR dissipate the energy via non-radiative decay, the non-equilibrium charge carriers (electron-hole pair) can be generated. If there are available electron-accepting orbitals nearby, such as unoccupied orbitals of adsorbed molecules on the metal surface, these high energetic electrons with adequate energy can transfer to the adsorbate and induce chemical reaction. Therefore, defining the required excitation energy to excite electron from metal nanoparticle to adsorbate unoccupied orbitals is essential to take the advantage of plasmonic catalyst and its application. In addition, if the reaction is hole-driven reaction, the excitation energy of an electron from occupied state of adsorbate to metal's Fermi level is critical. Moreover, if the reaction follows the energy transfer mechanism instead of the charge transfer mechanism, the excitation energy between HOMO and LUMO is important. However, the excitation energy highly depends on several factors such as the element choice of the metal nanoparticles, and the electronic structure of the reactants adsorbed on the active centers since these factors define the interaction between reactants and the catalyst surface. In other words, modifying the interaction between reactants and the catalyst surface can change the required excitation energy of electrons. In heterogenous catalyst, solvent also can alter the interaction between reactants and the catalyst surface and play a significant role on the chemical reaction. In plasmonic catalysis, the effect of solvent also studied, but mostly focusing on the effect of solvent on the LSPR of the metal nanoparticle.[129-134] Recent study shown the enhancement of the charge transfer between metal and semiconductor due to the decrease of the Schottky barrier generated by the image force of ionic layer of molecules on the metal when the reaction occur in the liquid phase instead of in the gas phase.[135] However, the effect of solvent on the plasmonic reaction, i.e., on the excitation energy, remains to explore.

In this study, we applied DFT and used the linear expansion ΔSCF to investigate the effect included by solvent on the excitation energy to induce the interfacial charge transfer between metal and adsorbed molecules, or the excitation energy within reactants due to the energy transfer. We used the NH_3 decomposition on Ru-doped Cu as the probe reaction since NH_3 is a promising medium for COx-free hydrogen storage.[36, 136, 137] The common solvents such as water, methanol and phenol were selected to study the effect of the local environment induced by solvent. We found that H-bond between these solvents and NH_3 could increase the excitation energy of an electron from the Fermi level of the system to LUMO of NH_3, while these bonds could reduce the excitation energy of an electron from HOMO of NH_3 to the Fermi level. We also found that changing the basicity of solvents can alter the LUMO level of adsorbates, resulting the change in the excitation energy to LUMO, i.e., the higher the ß of the solvent, the higher required energy to populate the LUMO of NH_3. The HOMO-LUMO gap also could be affected by the presence of solvent; but with less extensive than the increase of excitation energy from the Fermi level to LUMO. As a result, the H-bond between solvent and reactant can modify the excitation energy in both interfacial charge transfer and energy transfer mechanisms (Scheme 1).

Computational method

The DFT calculation with PBE exchange-correlation functional were performed using VASP version 5.4.1.[14, 39] The van der Waals (vdW) interaction was included by employing the DFT-D3 dispersion model.[41] A plane wave basis set with a kinetic energy cutoff of 500 eV was used for structure optimization in which the criteria of atomic force were set ≤ 0.02 eV/ Å. A four-layer $\sqrt{21} \times \sqrt{21}$ Ru-doped Cu(111) ($RuCu_{83}$) slab were constructed to model the surface of the Ru-doped Cu nanoparticle. While two top layers are fully relaxed, the two bottom layers are fixed. A 15 Å vacuum was added to separate slabs from their periodic images. The k-points grid of

(4×4×1) were used to converge the total energy. The energy convergence for electronic relaxation was set to 10^{-4} eV. The total energy was extrapolated to 0 K.

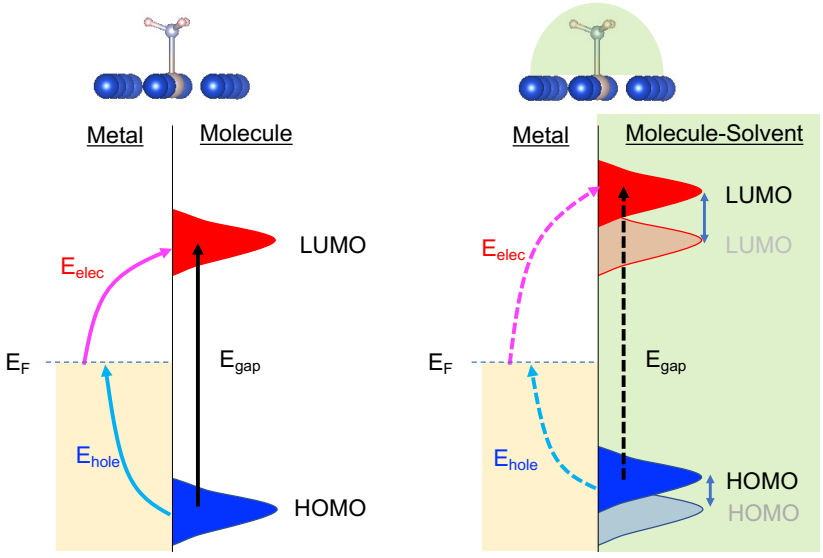
The optimized structures on the ground state calculated with VASP were adopted to calculate excited states using GPAW version 22.1.0.[15, 16] The exchange-correlation functional, plane-wave cutoff, and k-point grid in GPAW were kept the same as in VASP. The linear expansion delta self-consistent field (ΔSCF)[12] approach was used to calculate the energy of the system at excited states.

The band center of molecular orbital is the mean energy calculated as follows:

$$\bar{E} = \frac{\int \rho(E) E dE}{\int \rho(E) dE}$$

Where $\rho(E)$ represent DOS at corresponding energy E.

Results and discussion



Scheme 5.1 *Illustration of the effect of solvent on the excitation energy*

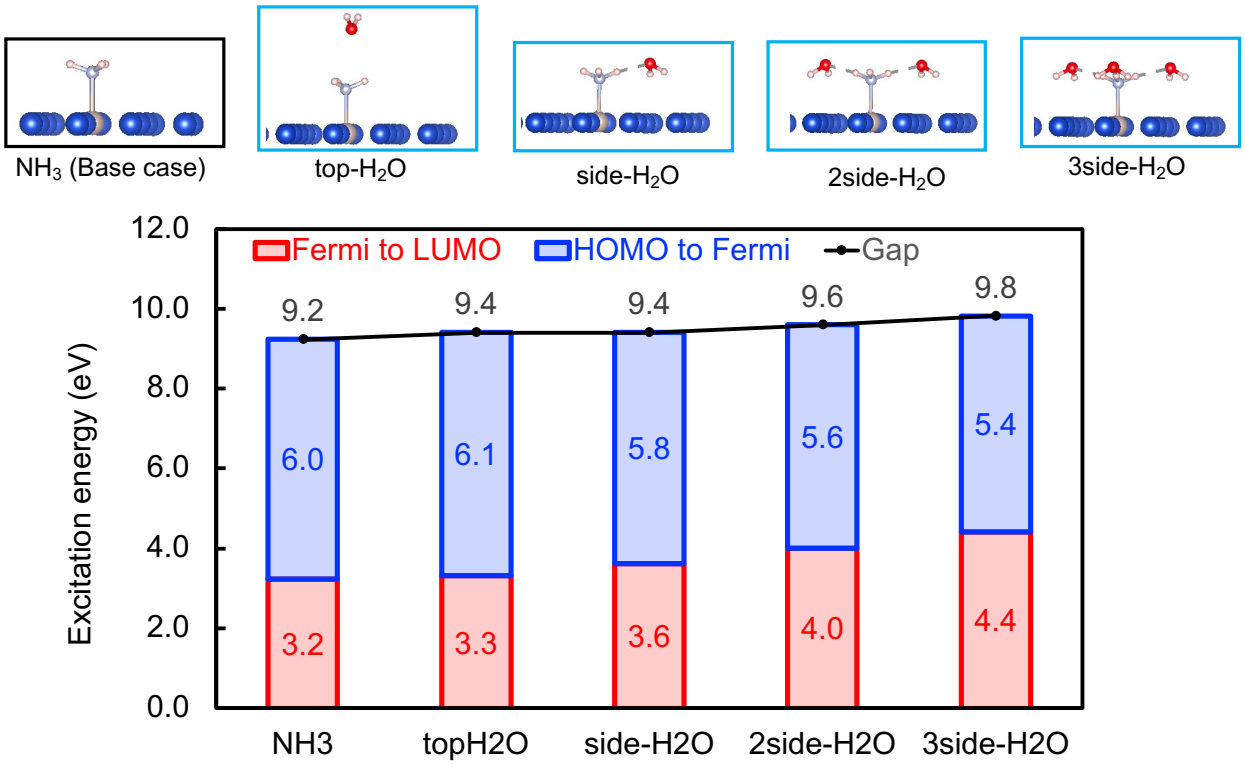


Figure 5.1 *The effect of H_2O. The excitation energy to excite electron from HOMO of NH_3 to Fermi level (blue), excite electron from Fermi level to LUMO of NH_3 (red), and the HOMO-LUMO gap (black). Optimized configuration of NH_3 only (Base case, black), NH_3 with H_2O (blue) on $RuCu_{83}$.*

As shown in literature[36, 136, 137], at low coverage, the first N−H bond dissociation in NH_3 is the rate limiting step for light-driven NH3 decomposition on Ru-doped Cu surface. Therefore, to investigate how solvent could affect the interfacial charge transfer between metal and adsorbed reactant, we first study the base case when only NH_3 adsorbs on Ru-doped Cu surface without solvents. The optimized structure of the base case is shown in top channel of Figure 5.1 (black). In this study, the interfacial charge transfer in this study is analyzed via the hole transfer process, which is represented by the excitation energy of an electron from HOMO of NH_3 to Fermi level

(denoted as E_{hole}), and the electron transfer process, which is reported via the excitation energy of an electron from Fermi level to LUMO of NH_3 (denoted as E_{elec}). For the base case, E_{hole} and E_{elec} are 6.0 eV and 3.2 eV respectively. In experiment, the photocatalysis reaction rate reach maximum at 2.6 eV,[137] which is lower by 0.6 eV compared to the calculated E_{elec} of the base case. This difference could result from the fact that the real catalyst surface of Ru-dopped Cu could has a complex geometry than the single atom model. The adsorption energy of NH_3 for the base case is ~ -1.4 eV, which is comparable with literature values[137].

The effect of local environment induced by solvent to the interfacial charge transfer is then studied by surrounding NH_3 with H_2O. We found that the adsorption energy of NH_3 increases when there is an interaction between H_2O and NH_3 (Table A4.1); however, the more significant impact is observed when H-bond is formed between NH_3 and H_2O at side adsorption configuration compared to the on-top adsorption of H_2O on NH_3. As a result, the top side adsorption of H_2O on NH_3 does not alter much the interaction between NH_3 and metal surface, leading to the similar excitation energy compared to the base case (Figure 5.1). Differently, the side adsorption of H_2O increased the required excitation energy for both electron and hole transfer process. The more H-bond formed between H_2O and NH_3 as the number of surrounding H_2O increase, the higher excitation energy. We observed that the E_{elec} increases by 0.4 eV per H-bond between H_2O and NH_3, while the value of E_{hole} decrease by 0.2 eV per H-bond (Figure 5.1). This change of the excitation energy can be attributed to the strong electronegativity of oxygen atom which enhance the electron withdrawal from NH_3, resulting in the shift up of the HOMO and LUMO center as shown in Figure 5.2. The more remarkable effect in E_{elec} than E_{hole} could be related to the fact that the LUMO of NH_3 is mainly located on H atoms, which can be directly influenced by the H-bond. Whereas most part of HOMO are located on N atom. As can be seen from Figure 5.2, the center

of the HOMO shifts from -4.43 eV of the base case to -4.20 eV, -3.98 eV and then to -3.80 eV with respect to Fermi level of the system when one, two and three H_2O molecules are added around NH_3. The center of the LUMO also move to higher energy, from 3.73 eV to 4.07eV, 4.38 eV and 4.68 eV with respect to Fermi level as the number of surrounding H_2O increases from 0 to 3 molecules. As a result, the local environment induced by H_2O, i.e., via H-bond with reactant, can enhance the hole transfer process or inhibit the electron transfer process between NH_3 and Ru-doped Cu surface. It is worth to note that we also examine the change in work function of catalyst surface with and without surrounding H_2O. We found that there is only a slightly change in the work function of the catalyst surface (Figure A4.1). In addition, there is no difference between the calculated core level energy of 1s orbital of Cu and the Fermi level among system without and without H_2O. These factors imply that the changing of E_{hole} and E_{elec} obtained in Figure 5.1 is related to the adjustment of HOMO and LUMO level due to the H-bond formation between NH_3 and H_2O. We also investigated the effect of H_2O on Cu surface instead of Ru-doped Cu surface, and found a similar trend between these two catalyst surface (Table A4.1 and Table A4.2).

The effect of local environment induced by solvent on the interfacial charge transfer is extended to 2 other solvents which are methanol and phenol (Figure 5.3 and Figure 5.4). Since the top adsorption configuration of water does not affect much the interfacial charge transfer, only the side adsorption of methanol and phenol are considered in this study. As expected for a solvent with slightly higher ß than water, the methanol induces an increase by ~ 0.5 eV of E_{elec} per H-bond between it and NH_3, which is higher by 0.1eV per H-bond compared to water. In contrast, the H-bond between phenol and NH_3 only causes an increase ≤ 0.2 eV of E_{elec} per H-bond, which is lower than that value of water. A comparison on E_{elec} when water or phenol is introduced nearby NH_3 is displayed in Figure 5.5. As can be seen from Figure 5.5, when the number of solvent molecules

increase, the bond length between N and Ru decrease due to the stronger interaction between NH_3 and catalyst surface. Despite the similar trend of the bond length and the excitation energy, the calculated values suggested that the impact of water is significant than that of phenol. This difference could be attributed to the lower ß of phenol than water. On the other hand, there is only a negligible change of E_{hole} when NH_3 forms H-bond with surrounding phenol molecules despite of the shift up of HOMO when more phenol molecules were introduced (Figure 5.4 and Figure A4.2). The changing of E_{hole} is similar for both case of water and methanol, i.e, decreasing by 0.2 eV per H-bond, imply that the slightly difference of ß is not impactful enough to cause the difference on the effect of methanol compared to water.

In plasmonic catalysis, apart from the interfacial charge transfer mechanism between the catalyst and adsorbed molecules, the energy transfer mechanism has been reported as the main mechanism in literature. The latter mechanism depends on the excitation of the electron within reactant's orbital, i.e., the excitation from HOMO to LUMO. In other word, the energy transfer mechanism relies on the HOMO-LUMO gap. We then analyzed the HOMO-LUMO gap as the sum of the E_{elec} and E_{hole} (indirect calculated value). We found that the effect of solvent on the E_{elec} is stronger than their effect on the HOMO-LUMO gap for three mentioned solvents (Figure 5.2), i.e., a change of 0.6 eV, 0.9 eV and 0.4 eV of E_{elec} compared to a change of 1.2 eV, 1.4 eV and 0.6 eV of HOMO-LUMO gap for the case of water, methanol and phenol respectively. As a result, the effect of local environment induced by solvent on the plasmonic catalysis could be considerable depending on the mechanism that the chemical reaction is followed. It is worth to note that the direct calculated excitation energy from HOMO to LUMO via GPAW is shown in Figure A4.3; the indirect and direct calculated value show the same trend for all studied solvent.

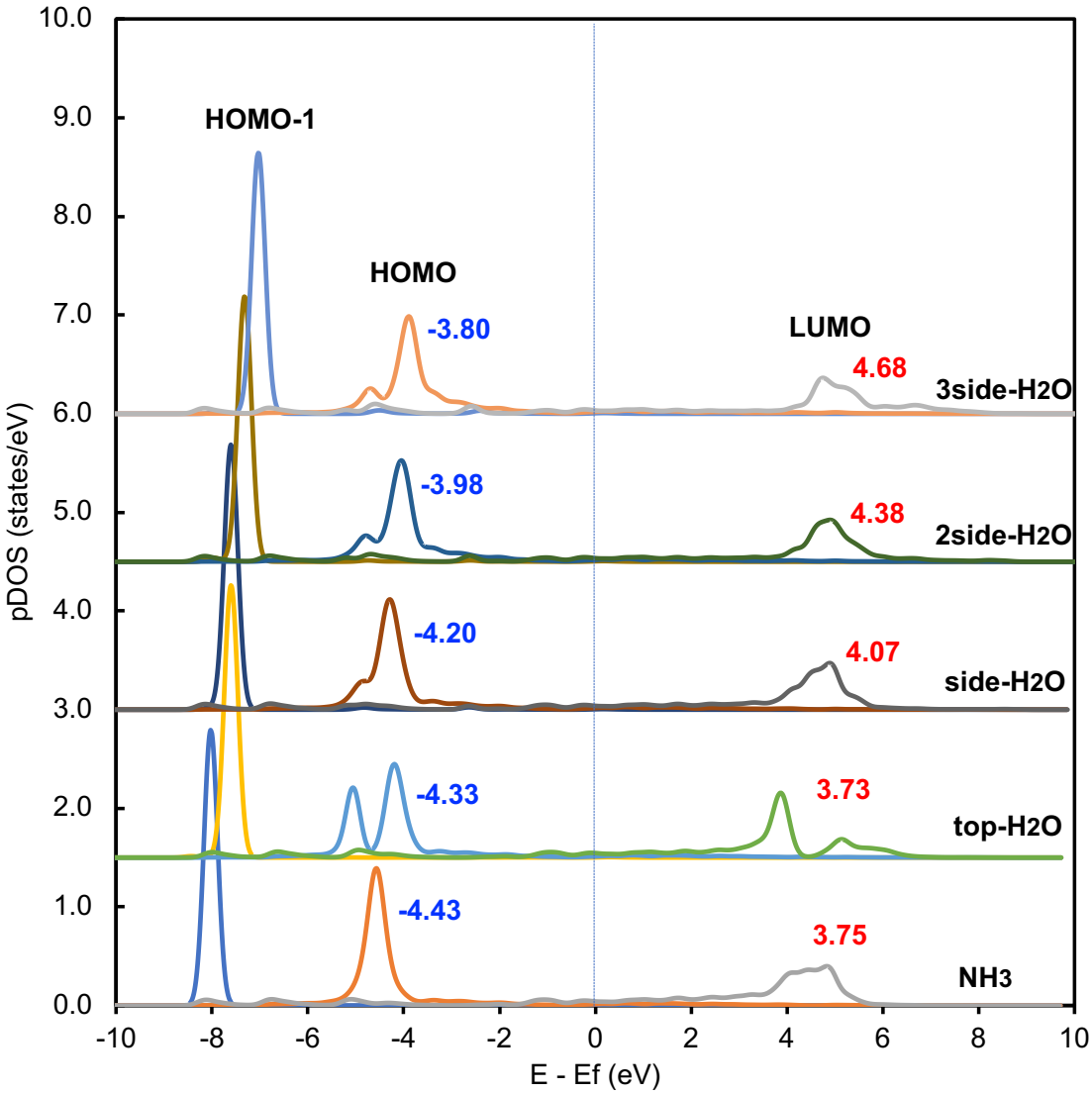


Figure 5.2 *Density of states projected on adsorbed NH_3 when only NH_3 adsorbed on $RuCu_{83}$ (and NH_3 with H_2O. The center of the HOMO and LUMO of NH_3 are shown above the main peak.*

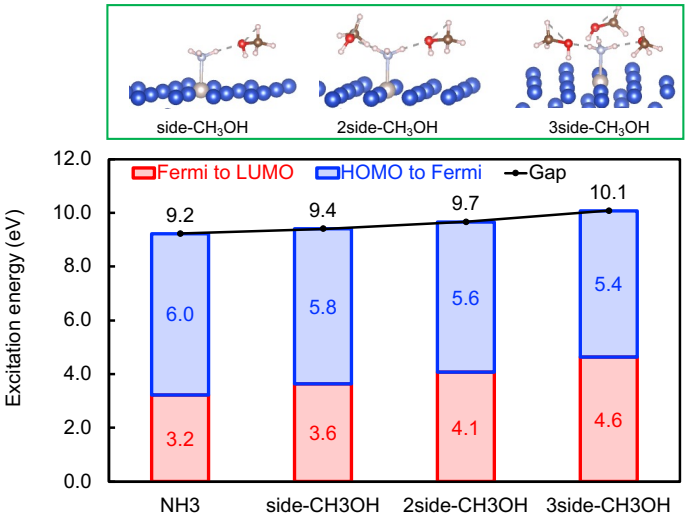


Figure 5.3 *The effect of CH_3OH. The excitation energy to excite electron from HOMO of NH_3 to Fermi level (blue), excite electron from Fermi level to LUMO of NH_3 (red), and the HOMO-LUMO gap (black). Optimized configuration of NH_3 only (Base case, black), NH_3 with CH_3OH (Green) on $RuCu_{83}$ are shown in the top channel.*

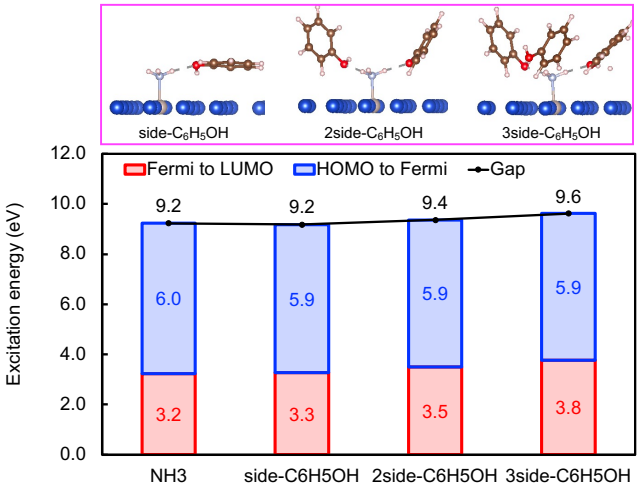


Figure 5.4 *The effect of C_6H_5OH. The excitation energy to excite electron from HOMO of NH_3 to Fermi level (blue), excite electron from Fermi level to LUMO of NH_3 (red), and the HOMO-LUMO gap (black). Optimized configuration of NH_3 only (Base case, black), NH_3 with CH_3OH (Green) on $RuCu_{83}$ are shown in the top channel.*

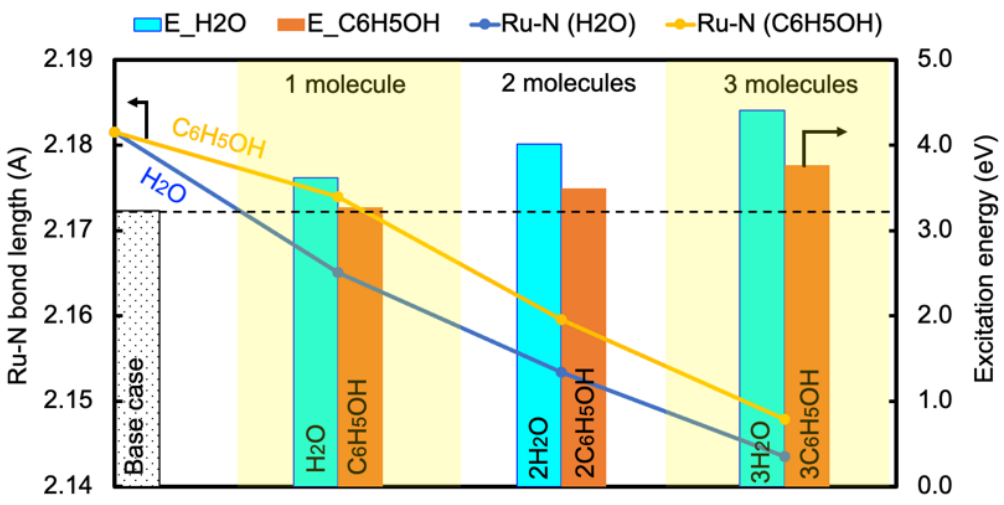


Figure 5.5 *The changing of the excitation energy to excite electron from Fermi level to LUMO of NH_3 and the Ru-N bond length as the number of H_2O/C_6H_5OH molecules increased*

Conclusion

By analyzing the excitation energy of an electron from adsorbate HOMO to Fermi level of the adsorbate/metal, and from this Fermi level to LUMO of adsorbed molecules using linear expansion ΔSCF method, we show that the H-bond between reactants and solvent could affect the interfacial charge transfer and the energy transfer between catalyst surface and reactants. While the presence of water, methanol or phenol nearby ammonia can inhibit the electron transfer process from metal to ammonia, it can facilitate the hole transfer process between them. The higher the ß of solvents, the stronger inhibition to the electron transfer process. The solvent also could alter the HOMO-LUMO gap of the adsorbate, which also can impact the plasmonic catalysis if the reaction follows the energy transfer mechanism. Our results provide the insight understanding how solvent could impact the plasmonic catalysis, and how to tune the reaction environment to enhance the efficiency of photocatalyst.

Chapter 6: Summary and Future Directions

6.1 Dissertation Summary

This work focused on the understanding of how the non-equilibrium affects chemical reactions on the hybrid plasmonic catalyst between the plasmonic metal and different components, including the semiconductor Cu_2O, Lewis acid zeolite, and transition metal Ru. In addition, the effect of solvent on the excitation energy of the hybrid plasmonic catalyst also is included.

First, by performing DFT calculations of oxide-catalyzed reaction on the hybrid plasmonic between metal and oxide Cu_2O, we have shown the importance of the interaction of Cu_2O with CO_2 to the accessibility of antibonding states of the adsorbed CO_2 in the range of visible light. Under photon excitation, the effective reaction barrier of CO_2 dissociation could reduce to a third of its intrinsic activation barrier at the ground state. These findings provide an explanation for the visible-light-induced direct CO_2 dissociation at low temperatures and under ambient pressure, even in the absence of H_2.

Secondly, to increase the probability of CO_2 dissociation induced by non-equilibrium electrons, the defective Cu_2O surface is considered. We found that the oxygen vacancy changes the thermodynamics of the CO_2 dissociation to less endothermic on the oxygen-deficient surface than the perfect surface, leading to a lower activation barrier at the ground state. This barrier can further decrease at the excited state due to the significant population of non-equilibrium electrons at the antibonding states. We also found that the oxygen vacancy is relatively easy to form by H_2 on Cu_2O surface, especially within the proximity of hydroxyl groups, independent of the presence of energetic electrons. As a result, a change in the reaction order with respect to H_2 and CO_2, corresponding to different rate-determining steps, with and without plasmonic excitation, may

occur. Our findings suggested maximizing the (111-VCu) surface for plasmonic catalyst applications in CO_2 conversion due to lower excitation energy and CO desorption energy.

Thirdly, we investigated the effects of energized carriers on acid-catalyzed reaction over the hybrid plasmonic catalyst of zeolite and have shown that the non-equilibrium charge carriers can tune the interaction between molecules and the Lewis acid zeolite. Furthermore, we found that replacing Si atoms in the zeolite framework with Ti and Sn could enable visible light to excite electrons from the plasmonic metal into zeolites. Our results also revealed the significant impact of the energized electrons on the molecules/catalyst interaction when the mid-gap states can be generated in zeolites. This concept can be used to manipulate molecular adsorption, product desorption, or zeolite activity for acid-catalyzed reactions. We further show that the non-equilibrium electrons can influence the intrinsic activation energy at the excited state of the propylene epoxidation, especially at high-doped concentrations of Ti atoms in the zeolite.

Finally, we found that the H-bond between reactants and solvents could affect the interfacial charge transfer and the energy transfer between catalyst surface and reactants due to the shift of LUMO and HOMO level. The H-bond increases the excitation energy, which can inhibit the interfacial charge transfer of an electron from the Ru-doped Cu surface to ammonia, whereas it can promote the hole transfer process between them. The stronger H-bond, the more significant effect on the electron transfer process. The results shed light on the significant role of solvents in the plasmonic catalysis.

6.2. Future directions

The results obtained from the ΔSCF method, such as estimating the excitation energy, the probability of excited state relaxation along the reaction pathway from an excited-state potential energy surface (PES) to the ground-state PES, i.e., the relaxation of the excited state when the bond stretching approach the transition state are useful. However, this approach cannot describe the real dynamics of how hot electrons can be decayed. Hence, a further study to perform TDDFT would be valuable and give more understanding of how chemical reactions are induced by excited electrons.

As can be seen from Chapter 3, it is challenging to distinguish the interfacial charge transfer mechanism and energy transfer mechanism in plasmonic catalysis in both experimental and modeling. The direct charge transfer and indirect charge transfer are also difficult to identify which one is the domain mechanism. Moreover, the electron can originally be excited from the metal, but the process of whether these electrons transfer tunning through the semiconductor to the reactive or transfer to the semiconductor and then to the reactive interface remains unclear. In some cases, the non-radiative decay can even transfer energy through an insulating spacer layer, so the excited electron can probably transfer ballistically through the semiconductor to the reactive interface. Further investigation to study the exact electron transfer pathway, such as via TDDFT could bring a more insightful understanding of this process.

Take the advantages of the zeolite plasmon-modulated Lewis acid catalysis, as shown in Chapter 4, and further studies to investigate how highly energetic carriers generated in plasmonic metal can be used for other acid-catalyzed reactions on zeolite. Especially, it is interesting to examine how the excited carrier interplay with the different confinement environment due to the different pore size/framework, the different acid density, the identify of hetero atoms dopped into

zeolite framework, the extra-framework, and/or the moieties/solvents for chemical transformations occurs at the active sites.

In addition to the acid-catalyzed in Chapter 4, the effect of non-equilibrium charge carriers on base-catalyzed reaction should be studied in the future. For example, the base-catalyzed self-condensation of acetone on MgO. In this case, the aldol condensation follows a nucleophilic addition mechanism, in which the first step is the generation of an enolate intermediate by deprotonation of α position. The second step is C-C formation by the nucleophilic attack of carbonyl, followed by the proton transfer and dehydration steps. Consequently, this reaction highly depends on the charge transfer between the catalyst and the 1st acetone molecule and the charge transfer between the 2nd acetone molecule and the enolate intermediate. Since the MgO has a large bandgap (~ 7.8 eV), we expect that the excited electron or hole is most likely localized at acetone molecules; therefore, it is possible to manipulate this reaction kinetic by non-equilibrium charge carriers.

In Chapter 5, only the excitation energy of ammonia orbitals in the presence of solvents such as water, methanol, or phenol was considered. However, if the orbitals of solvents and orbitals of reactants significantly overlap, the excited electron could be populated into the solvents' orbitals instead of reactants, which may lead to the shift of selectivity. Further studies investigating the excited electron on the selectivity in the presence of solvents could bring more insight and guidelines for the plasmonic catalyst in the liquid phase. In addition to solvents, the reactant's coverage also plays a critical role in the heterogeneous catalyst, but the interplay of the non-equilibrium charge carrier with the reactant's coverage remains to explore. Future research focusing on the role of the coverage should give more valuable information to this field.

Appendix A1: Supporting information for Chapter 3.1

Plasmonic Energetic Electrons Drive CO_2 Reduction on the pristine Cu_2O surface

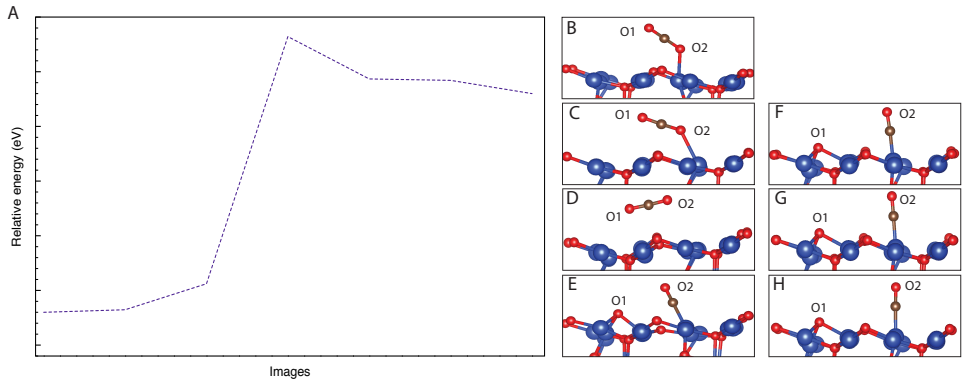


Figure A1.1 *The NEB calculation results (A) and the represented configurations along reaction pathway after running about 1,000 steps (B-H). Based on NEB, the transition state and activation energy were calculated further by applying the dimmer method. We also tried to calculate the NEB calculation for breaking the C-O2 bond with O2 remains at unsaturated Cu and the C-O1 travelling to the nearby unsaturated Cu. However, the calculation cannot be converged.*

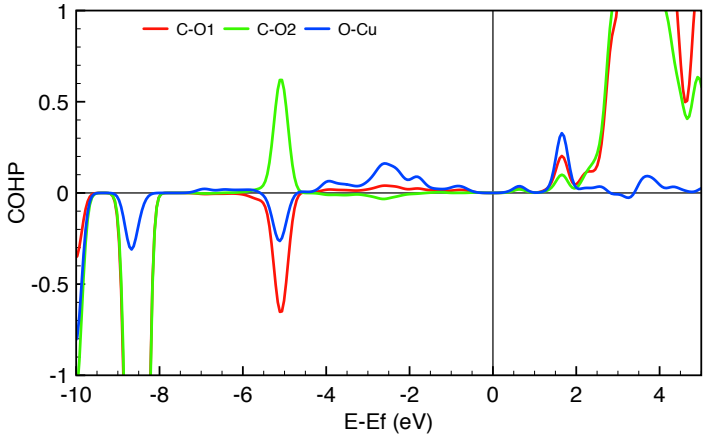


Figure A1.2 *Crystal orbital Hamilton population (COHP)* [138] *of absorbed CO_2 on Cu_2O (111) surface at the initial state*

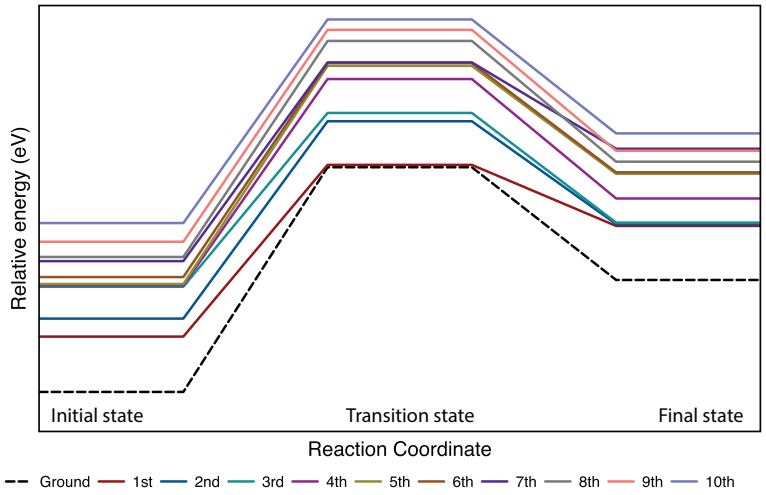


Figure A1.3 *Ground state and excited state energies (eV) along reaction pathway predicted by the PBE+U functional combined with the ΔSCF approach. Each colored line represents a reaction profile mapping from the initial state to the final state by manipulating electronic occupation at different electronic states above the Fermi level and a hole at Fermi level*

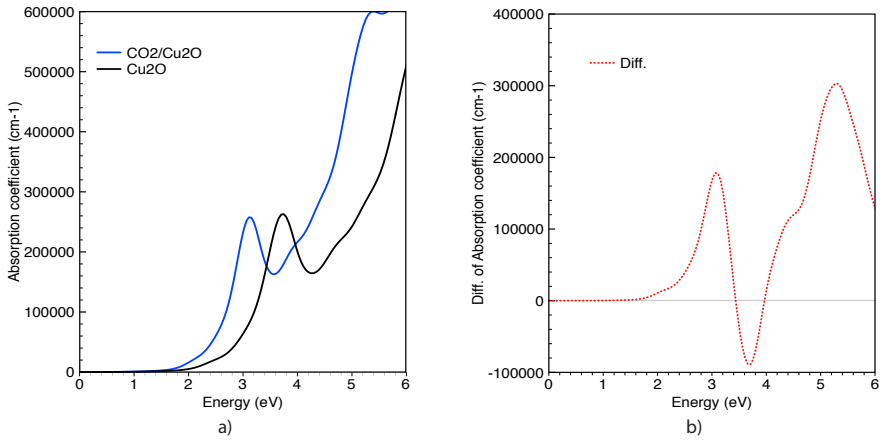


Figure A1.4 *a) The absorption coefficient of Cu_2O (black) and Cu_2O with adsorbed CO_2 (blue); b) The difference of absorption coefficient between the two structures with and without adsorbed CO_2 on Cu_2O. Both calculations were performed using the HSE06 functional. For the Cu_2O result plotted in the figure, we removed the CO_2 while keeping the other atoms fixed at their positions.*

The absorption coefficient is calculated by the following relation[139]:

$$\alpha = \frac{4\pi\kappa}{\lambda} = \frac{2\sqrt{2}\pi E}{hc}\left((\epsilon_1^2 + \epsilon_2^2)^{\frac{1}{2}} - \epsilon_1\right)^{\frac{1}{2}}$$

Where ϵ_1 and ϵ_2 are the calculated real and imaginary part of the dielectric constant using the HSE functional.

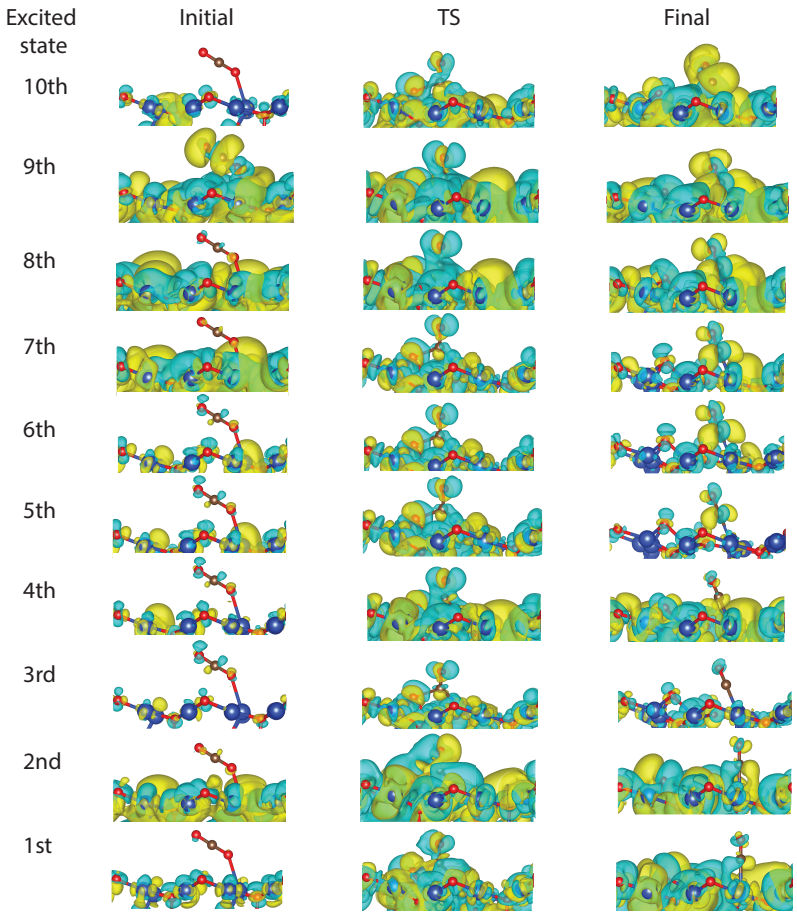


Figure A1.5 *The charge density difference between the excited states (which has an added electron into unoccupied KS orbital and a hole at Fermi level) with the ground state. Cyan color represents for removed electron and yellow color represents for added electron. An isosurface value of 0.00067 e/Å³ is used.*

Table A1.1 *The difference of the Bader charge between the excited states (which has only an added electron into unoccupied KS orbital) and the ground state*

Initial	**1st**	**2nd**	**3rd**	**4th**	**5th**	**6th**	**7th**	**8th**	**9th**	**10th**
Diff-C	-0.02	-0.02	-0.02	-0.02	-0.02	-0.02	-0.02	-0.02	-0.01	-0.02
Diff-O1	0.00	0.01	0.00	0.00	0.00	0.01	0.01	0.01	0.02	0.01
Diff-O2	-0.06	-0.06	-0.06	-0.06	-0.06	-0.06	-0.06	-0.06	-0.06	-0.06
Diff-(C and O2)	-0.08	-0.08	-0.08	-0.08	-0.08	-0.08	-0.08	-0.08	-0.06	-0.08
Diff-(C, O1 and O2)	-0.08	-0.07	-0.08	-0.08	-0.08	-0.08	-0.08	-0.08	-0.05	-0.08

Transition state	**1st**	**2nd**	**3rd**	**4th**	**5th**	**6th**	**7th**	**8th**	**9th**	**10th**
Diff-C	-0.20	-0.20	-0.20	-0.19	-0.20	-0.20	-0.20	-0.20	-0.20	-0.19
Diff-O1	0.18	0.18	0.18	0.18	0.18	0.18	0.18	0.18	0.18	0.18
Diff-O2	0.12	0.12	0.12	0.12	0.12	0.12	0.11	0.11	0.11	0.12
Diff-(C and O2)	-0.07	-0.09	-0.08	-0.08	-0.08	-0.08	-0.08	-0.08	-0.09	-0.07
Diff-(C, O1 and O2)	0.11	0.10	0.10	0.11	0.10	0.10	0.10	0.10	0.09	0.11

Final	**1st**	**2nd**	**3rd**	**4th**	**5th**	**6th**	**7th**	**8th**	**9th**	**10th**
Diff-C	0.01	0.01	0.01	0.01	0.04	0.05	0.06	0.05	0.09	0.14
Diff-O1	0.04	0.04	0.02	0.02	0.02	0.02	0.02	0.02	0.02	0.02

Diff-O2	-0.11	0.03	0.02	0.03	0.05	0.03	0.02	0.04	0.04	0.06
Diff-(C and O2)	-0.10	0.03	0.03	0.04	0.09	0.08	0.08	0.08	0.13	0.20
Diff-(C, O1 and O2)	-0.06	0.08	0.05	0.06	0.11	0.09	0.10	0.10	0.15	0.22

Table A1.2 *The difference of the Bader charge between the excited states (which has an added electron into unoccupied KS orbital and a hole at Fermi level) and the ground state*

Initial	**1st**	**2nd**	**3rd**	**4th**	**5th**	**6th**	**7th**	**8th**	**9th**	**10th**
Diff-C	-0.03	-0.03	-0.03	-0.03	-0.03	-0.03	-0.03	-0.03	-0.02	-0.03
Diff-O1	-0.01	-0.01	-0.01	-0.01	-0.01	-0.01	-0.01	-0.01	0.00	-0.01
Diff-O2	-0.05	-0.05	-0.05	-0.05	-0.05	-0.05	-0.06	-0.05	-0.05	-0.05
Diff-(C and O2)	-0.08	-0.08	-0.08	-0.08	-0.08	-0.08	-0.08	-0.08	-0.07	-0.08
Diff-(C, O1 and O2)	-0.09	-0.09	-0.09	-0.09	-0.09	-0.09	-0.09	-0.09	-0.07	-0.09

Transition state	**1st**	**2nd**	**3rd**	**4th**	**5th**	**6th**	**7th**	**8th**	**9th**	**10th**
Diff-C	-0.21	-0.21	-0.20	-0.20	-0.20	-0.20	-0.20	-0.20	-0.21	-0.20
Diff-O1	0.29	0.15	0.16	0.14	0.16	0.16	0.16	0.14	0.14	0.16
Diff-O2	0.08	0.08	0.08	0.08	0.08	0.08	0.08	0.07	0.07	0.09
Diff-(C and O2)	-0.13	-0.13	-0.12	-0.12	-0.12	-0.12	-0.12	-0.13	-0.13	-0.11
Diff-(C, O1 and O2)	0.16	0.02	0.04	0.02	0.04	0.04	0.04	0.01	0.00	0.05

Final	**1st**	**2nd**	**3rd**	**4th**	**5th**	**6th**	**7th**	**8th**	**9th**	**10th**
Diff-C	0.00	0.00	0.00	0.00	0.01	0.02	0.02	0.02	0.06	0.13
Diff-O1	0.02	0.01	0.00	0.00	0.00	0.00	-0.02	0.00	0.00	0.00
Diff-O2	0.00	0.00	0.00	0.00	0.00	0.00	0.00	0.00	0.01	0.03
Diff-(C and O2)	0.00	0.00	0.00	0.00	0.01	0.01	0.02	0.03	0.07	0.16
Diff-(C, O1 and O2)	0.02	0.01	0.00	0.00	0.01	0.01	0.00	0.03	0.06	0.16

Appendix A2: Supporting information for Chapter 3.2

Plasmonic Energetic Electrons Drive CO_2 Reduction on Defected Cu_2O

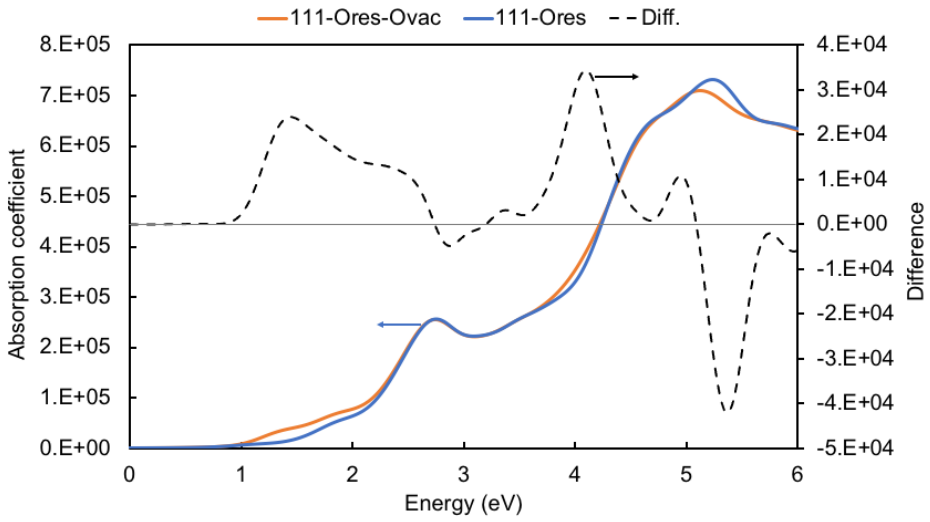


Figure A2.1 *Optical absorption coefficient of the (111-Ores) surface with and without oxygen vacancy. Unit:* cm^{-1}.

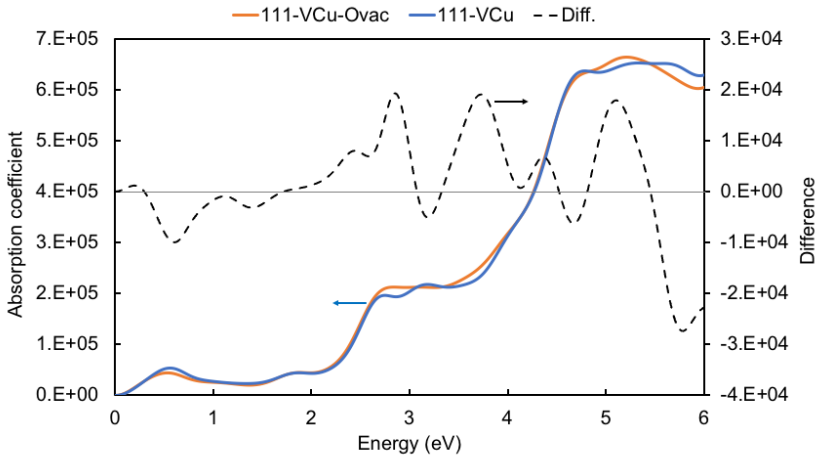


Figure A2.2 *Absorption coefficient of the (111-VCu) surface with and without oxygen vacancy. Unit:* cm^{-1}.

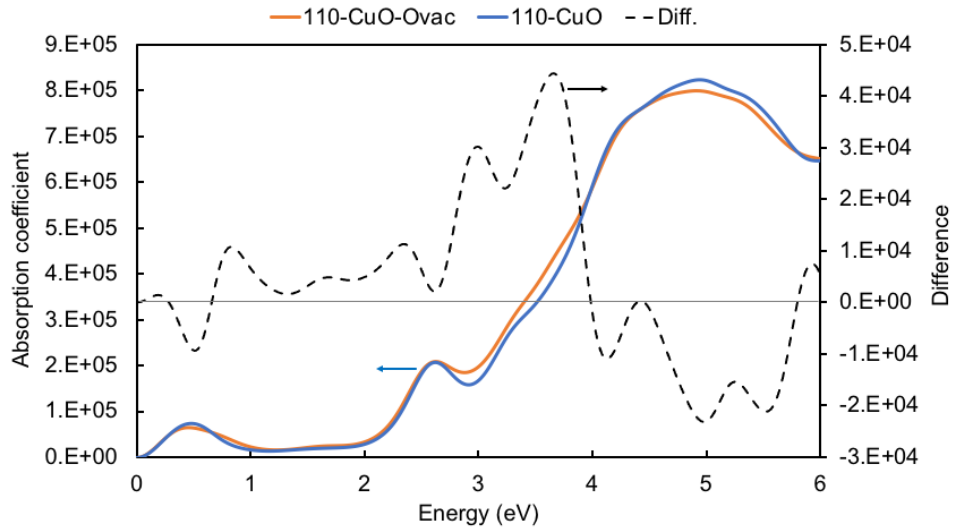


Figure A2.3 *Absorption coefficient of the (110-CuO) surface with and without oxygen vacancy. Unit: cm^{-1}.*

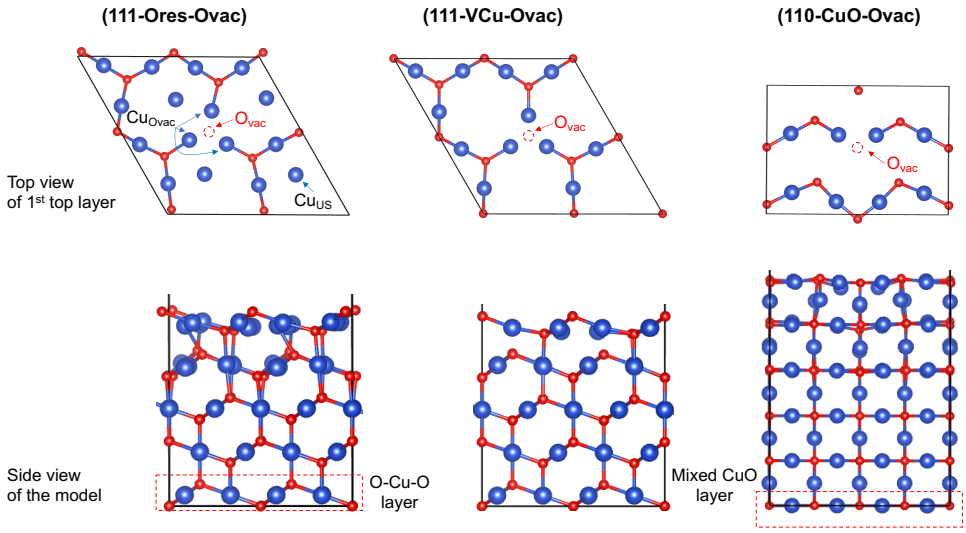


Figure A2.4 The model of the oxygen-deficient surfaces of Cu_2O. *The blue and red balls denote for Cu and O atoms respectively.*

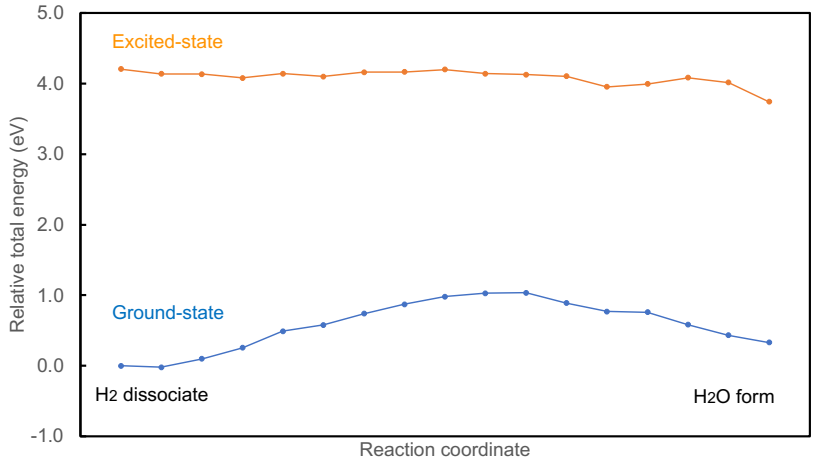


Figure A2.5 *The ground- and excited-state energy profile of the oxygen vacancy formation step when one electron is added into the LUMO of H_2O by GPAW.*

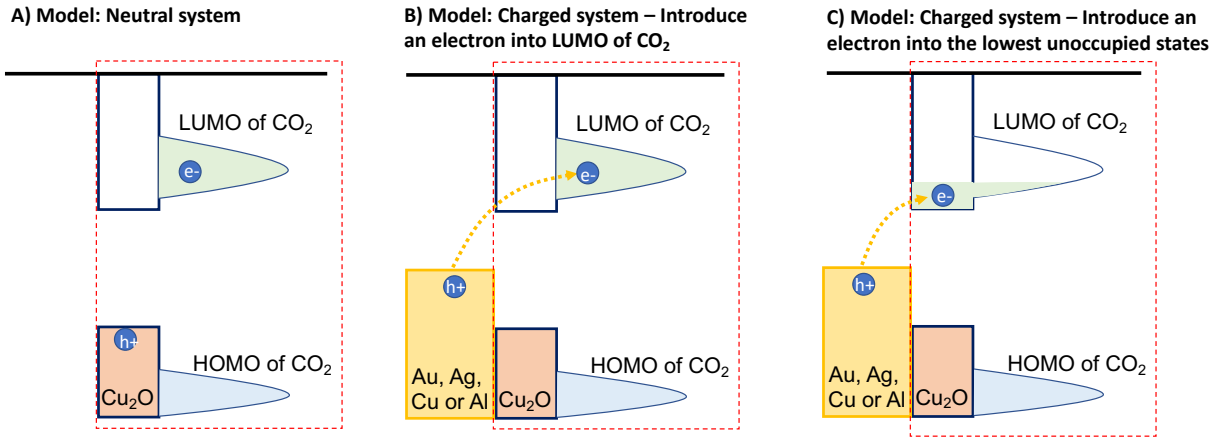


Figure A2.6 Scheme to illustrate how photo-excited electron is modelled in our study. *The model is shown in the red rectangle.* ***(A)*** *The model of the neutral system.* ***(B)*** *The model of the charged system (one additional electron is added into the neutral system) when an electron is added into the project LUMO of the adsorbed molecule (green area).* ***(C)*** *The model of the charged system when an electron is added into the lowest unoccupied states of the system (green area).*

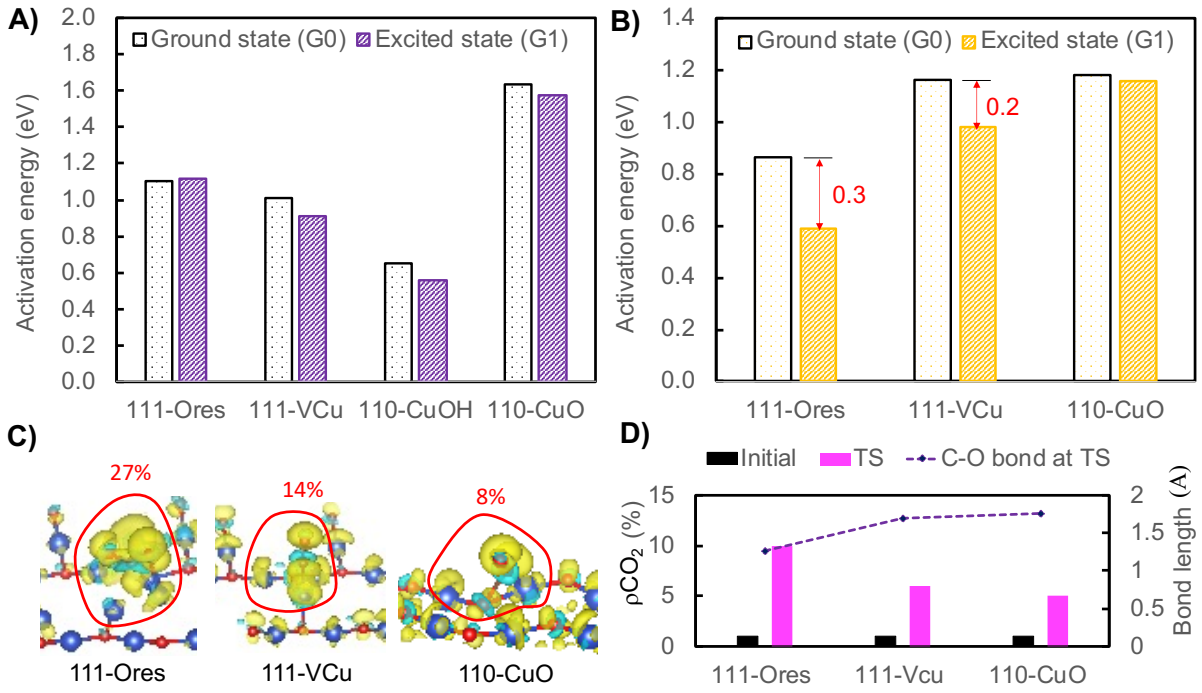


Figure A2.7 DFT results when one additional electron is added into the lowest unoccupied states of the charged system by VASP. (A) *The intrinsic activation energy at the ground- and excited state of the oxygen vacancy formation step.* ***(B)*** *The intrinsic activation energy at the ground- and excited-state of the CO_2 dissociation step.* ***(C)*** *The charge density difference projected on CO_2 and under-coordinate Cu atoms at the transition state between the ground- and excited-PES.* ***(D)*** *The relationship between charge density localized on CO_2 at the initial state and the transition state, and the C-O bond length at the transition state.*

The CO_2 dissociation barrier reduces by 0.3 eV for the (111-Ores-Ovac) surface (Fig. S7B). Decrease of this barrier for the (111-VCu-Ovac) surface is 0.2 eV, but a negligible change was obtained for the (110-CuO-Ovac) surface. We find that there is a correlation between the reduction of the activation energy with the charge localized at the adsorbed CO_2; the higher the localized charge is, the larger the gap between the intrinsic activation energy at the ground state and the excited state (Figure S7C). The C-O bond length in CO_2 at the transition state, can also indicate

the effect of the photo-excited electron (Figure S7D). A longer C-O bond indicates a later transition state and a more pronounced electron transfer from the vacancy to CO_2 at the transition state. Therefore, a greater change for CO_2 dissociation was obtained on (111-Ores-Ovac) than the other two facets. Meanwhile, the added electron is delocalized on the Cu_2O surface, resulting in no significant for vacancy formation (Figure S7A).

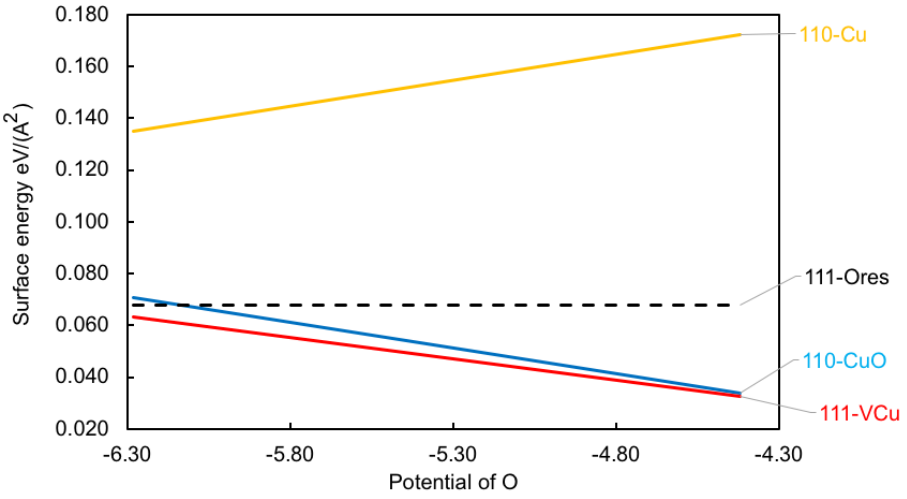


Figure A2.8 The surface energy of Cu_2O. *The O-terminated Cu_2O (111) surface (111-Ores, black), the O-terminated Cu_2O (111) surface with Cu vacancy (111-VCu, red), the mixed CuO-terminated (110) surface (110-CuO, blue) and the Cu-terminated (110) surface (110-Cu, orange).*

Appendix A3: Supporting information for Chapter 4.1

A first-principles study of the interaction between molecules and Lewis acid zeolites manipulated by injection of energized charge

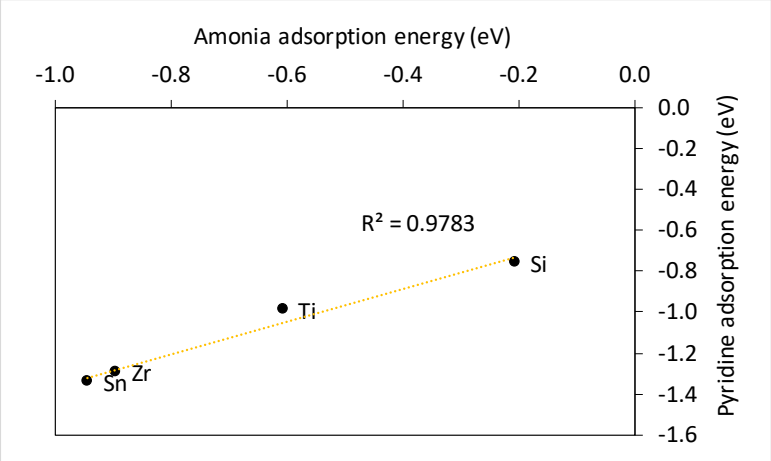


Figure A3.1 *Relationship between NH_3 and pyridine adsorption energy on M-BEA.*

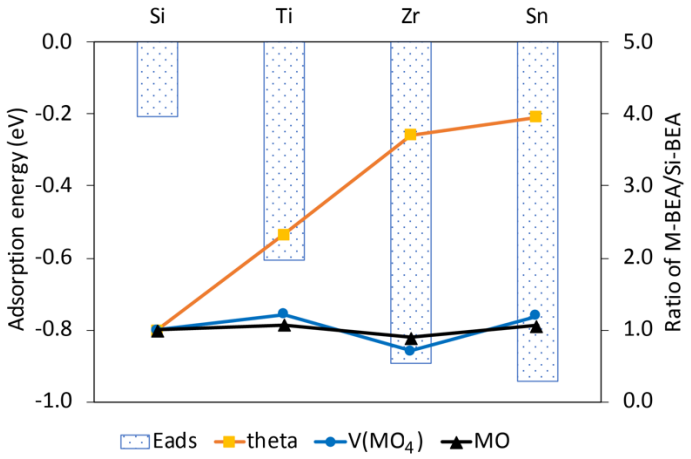


Figure A3.2 *Relationship between NH_3 adsorption energy on M-BEA with the mean square deviation from regular tetrahedron angle (O-M-O angle) (theta, θ), the volume of tetrahedral (V_{MO_4}) and the average bond M-O bond length with the four oxygen nearby metal center.*

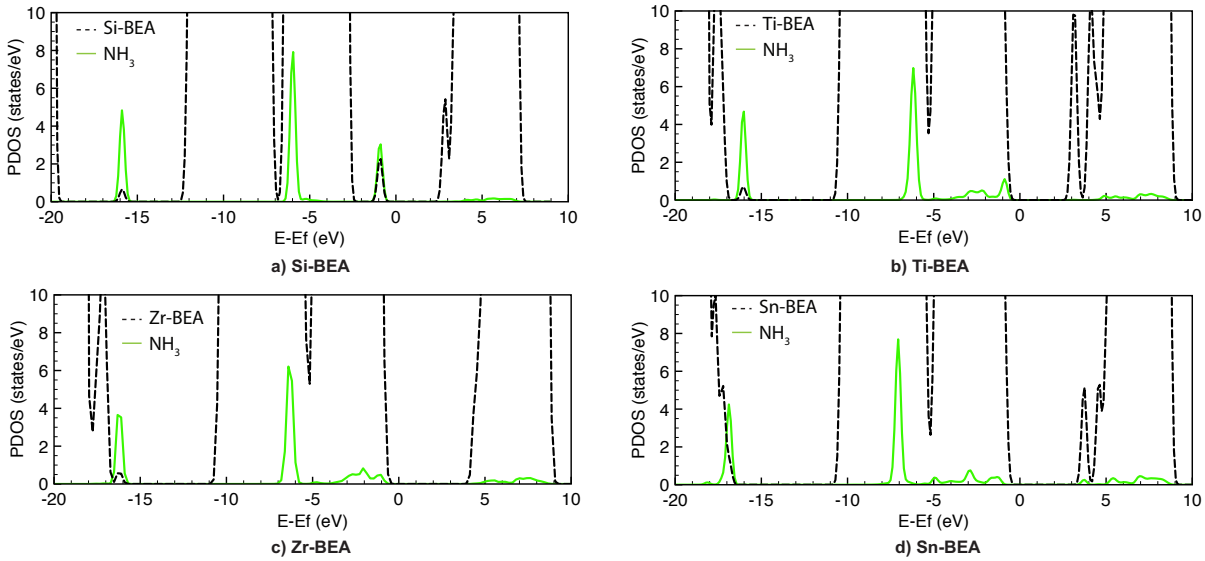


Figure A3.3 *PDOS of adsorbed NH_3 (green) on M-BEA (black): a) Si-BEA b) Ti-BEA c) Zr-BEA d) Sn-BEA*

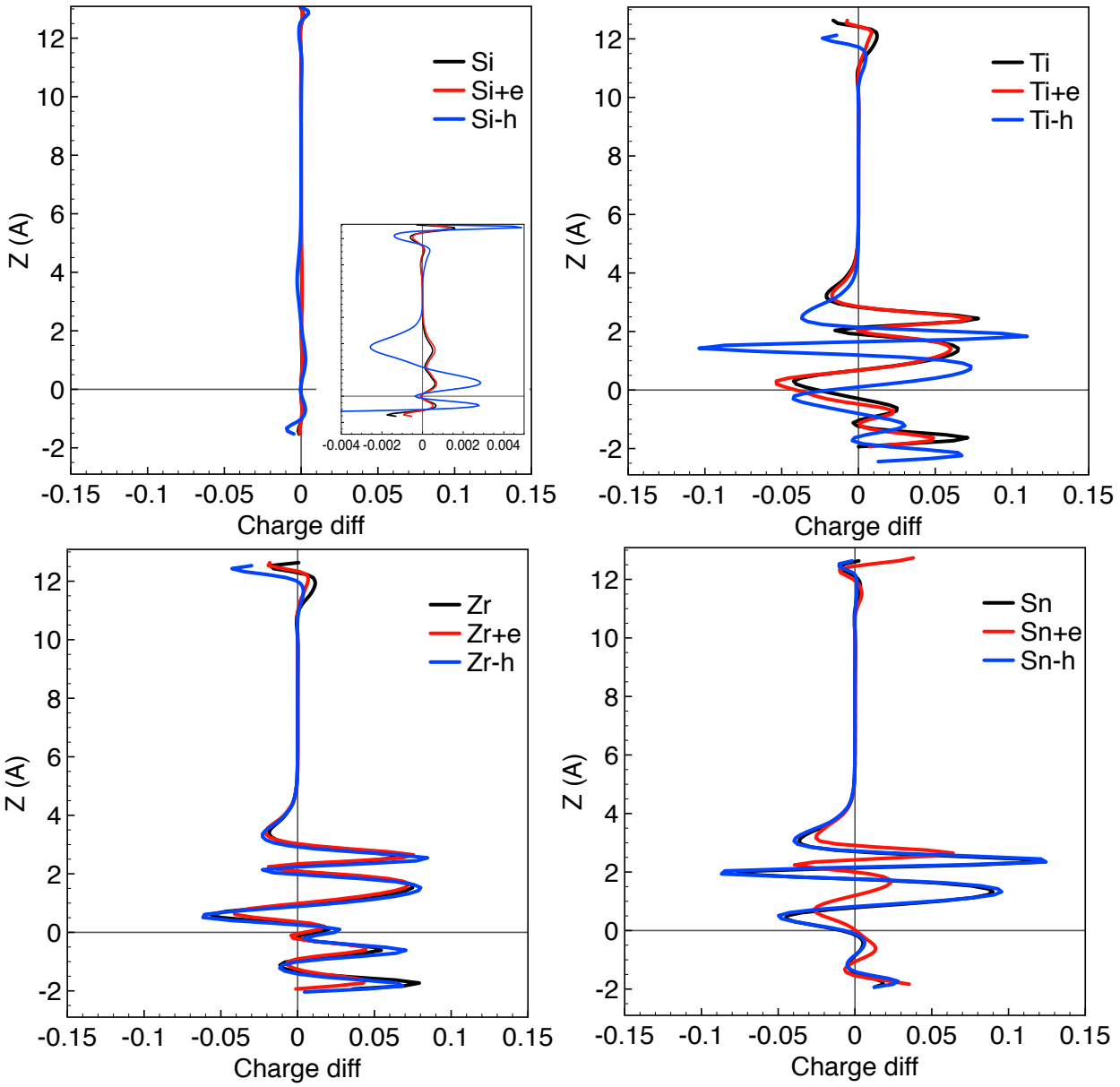


Figure A3.4 *(duplicated from Figure 4 of the main text): Charge redistribution at the interface between the Lewis acid (M-BEA) and NH_3 in the z direction at the ground state (back color), at excited states with an energized electron (red color) and at excited states with an energized hole (blue color).*

Table A3.1 *The mean square deviation from regular tetrahedron angle (O-M-O angle) of M-BEA at the ground state, at excited states with an energized electron and excited states with an energized hole.*

M-BEA	**Ground state**	**Excited state with energized electron**	**Excited state with energized hole**
Si	1.1	1.2	1.1
Ti	2.6	5.0	2.6
Zr	4.1	4.4	4.2
Sn	4.4	13.8	4.4

Table A3.2 *The adsorption energy of NH_3 on the open site of Sn-BEA ($(OSi)_3SnOH$) under the effect of the energized electron or hole.*

	$(OSi)_3SnOH$	**$(OSi)_3SnOH$ + e**	**$(OSi)_3SnOH$ - h**
Eads (eV)	-0.9	-0.3	-1.0
N-Sn bond length (Å)	2.38	2.71	2.35

Table A3.3 *Bader charge analysis on Sn and OH groups of Sn-BEA shown in Figure 4.1.5 at the ground state, at excited states with an energized electron and excited states with an energized hole.*

Bader charge of M-BEA	**Ground state**	**Excited state with energized electron**	**Excited state with energized hole**

Sn	1.67	2.16	1.67
O	7.42	7.38	7.42
O (Silanol)	7.33	7.33	7.30
H (Silanol)	0.26	0.34	0.25
H	0.30	0.36	0.25

Table A3.4 *HSE06 calculation results (unit: eV)*

M-BEA	**HSE06**					**PBE**	
	IP	**EA**	**Bandgap**	**ΔEads with 1 added electron**	**ΔEads with 1 removed electron**	**ΔEads with 1 added electron**	**ΔEads with 1 removed electron**
Si-BEA	4.1	-3.4	7.4	0.0	-0.6	0.0	-0.5
Sn-BEA	4.0	-2.1	6.2	0.6	-0.1	0.6	-0.1

Appendix A4: Supporting Information for Chapter 5

Local enviroment effect induced by solvent on the plasmonic catalysis

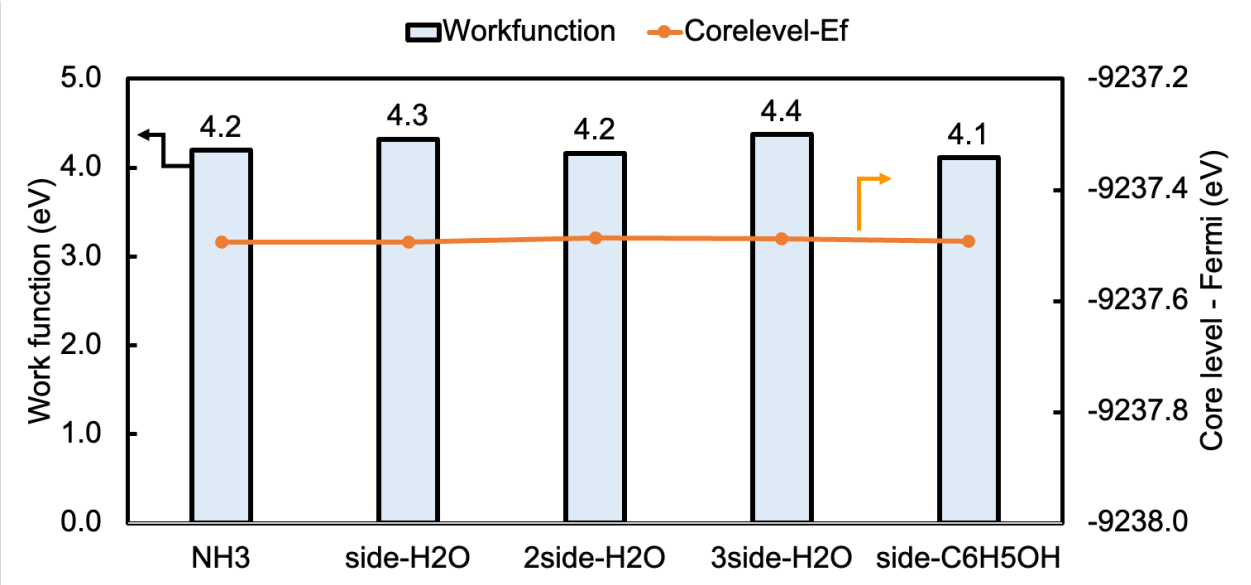


Figure A4.1 *The changing of wavefunction and the energy difference between core level of Cu 1s with respect to Fermi level as the number of* H_2O/C_6H_5OH *molecules increased*

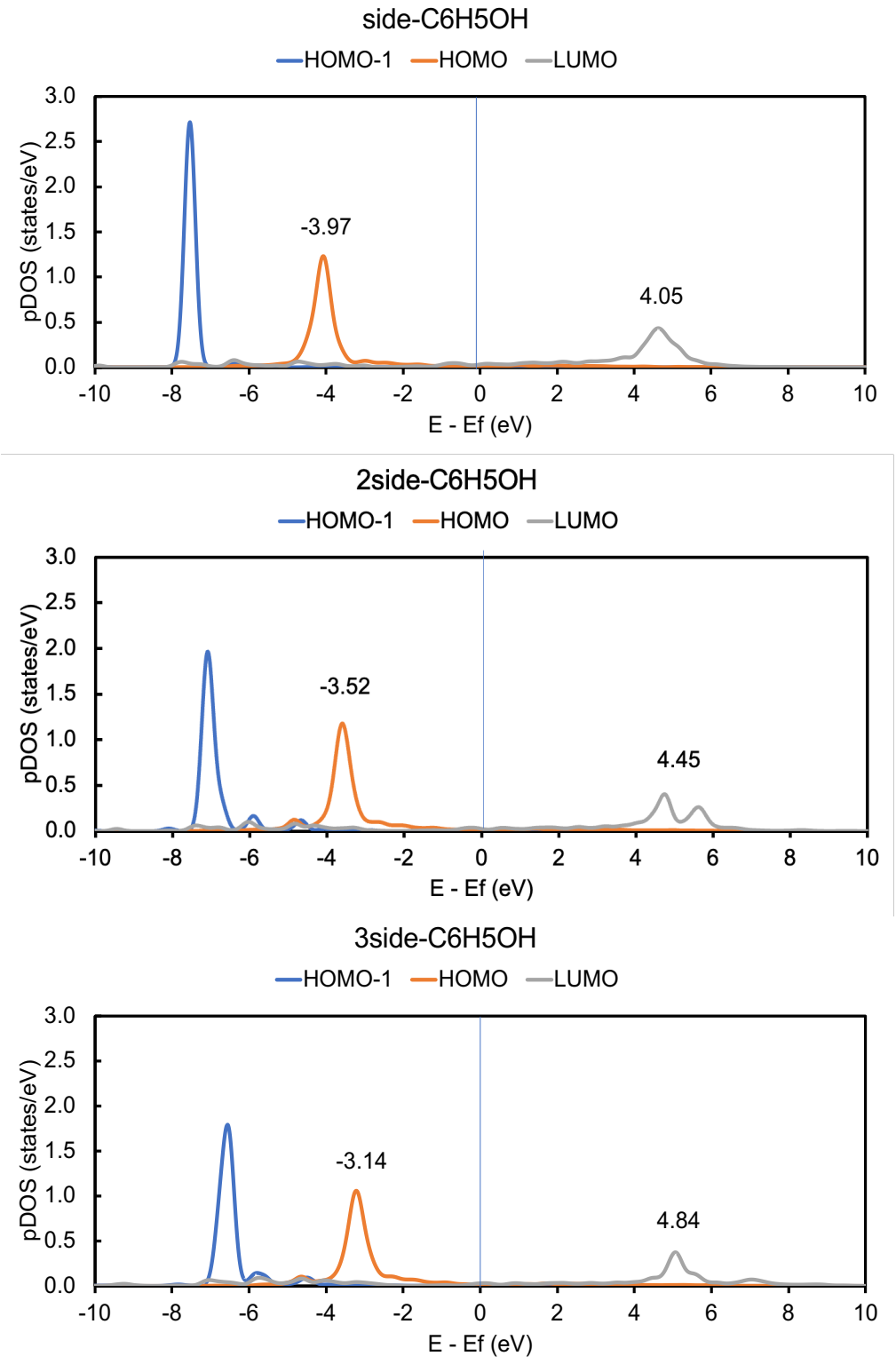


Figure A4.2 *Density of states projected on adsorbed NH_3 when it is surrounding by C_6H_5OH. The center of the HOMO and LUMO of NH_3 are shown above the main peak.*

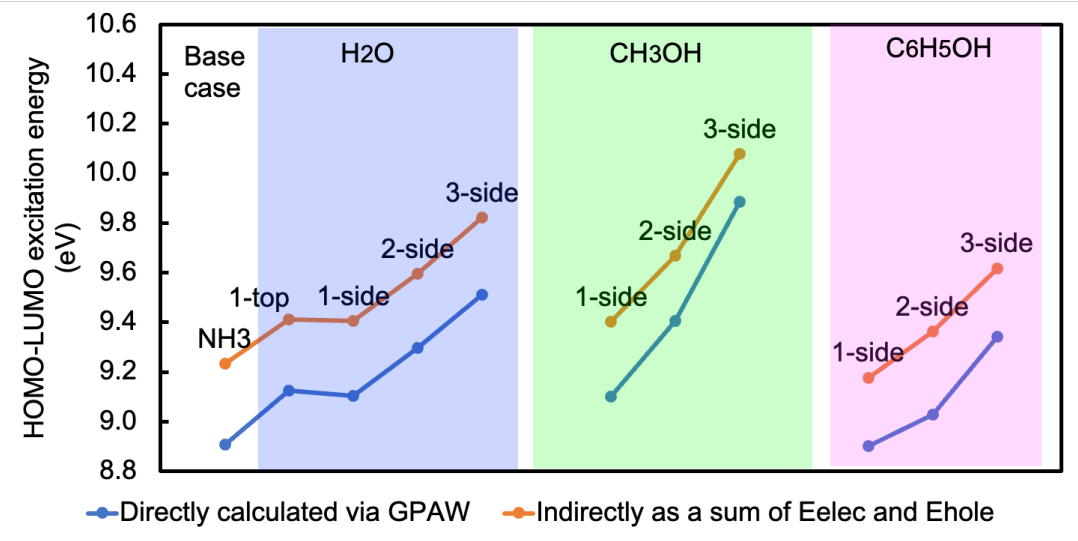


Figure A4.3 *Comparison of the HOMO-LUMO gap when it is directly calculated via GPAW versus when it is indirectly calculated as a sum of* E_{elec} *and* E_{hole}.

Table A4.1 *The adsorption energy of* NH_3 *on the Ru-doped Cu surface (*$RuCu_{83}$*) vs Cu surface (*Cu_{84}*). Unit: eV*

	NH_3	**topH_2O**	**side-H_2O**	**2side-H_2O**	**3side-H_2O**
$RuCu_{83}$	-1.40	-1.61	-2.02	-2.59	-3.12
Cu_{84}	-0.88	-1.07	-1.51	-2.11	-2.68

Table A4.2 *The excitation energy of an electron from Fermi level to LUMO of* NH_3 *of the Cu surface (*Cu_{84}*). Unit: eV*

Cu_{84}	**NH_3**	**topH_2O**	**side-H_2O**	**2side-H_2O**	**3side-H_2O**
Fermi level to LUMO	3.21	3.29	3.57	3.93	4.33

References

(1) Zhang, Y.; He, S.; Guo, W.; Hu, Y.; Huang, J.; Mulcahy, J. R.; Wei, W. D. Surface-plasmon-driven hot electron photochemistry. *Chemical Reviews* **2018**, *118* (6), 2927-2954.
(2) Cortés, E.; Camargo, P. H. *Plasmonic Catalysis: From Fundamentals to Applications*; John Wiley & Sons, 2021.
(3) Brongersma, M. L.; Halas, N. J.; Nordlander, P. Plasmon-induced hot carrier science and technology. *Nature nanotechnology* **2015**, *10* (1), 25-34.
(4) Linic, S.; Chavez, S.; Elias, R. Flow and extraction of energy and charge carriers in hybrid plasmonic nanostructures. *Nature Materials* **2021**, *20* (7), 916-924.
(5) Ezendam, S.; Herran, M.; Nan, L.; Gruber, C.; Kang, Y.; Gröbmeyer, F.; Lin, R.; Gargiulo, J.; Sousa-Castillo, A.; Cortés, E. Hybrid Plasmonic Nanomaterials for Hydrogen Generation and Carbon Dioxide Reduction. *ACS Energy Letters* **2022**, *7*, 778-815.
(6) Ni, M.; Leung, M. K.; Leung, D. Y.; Sumathy, K. A review and recent developments in photocatalytic water-splitting using TiO2 for hydrogen production. *Renewable and Sustainable Energy Reviews* **2007**, *11* (3), 401-425.
(7) Hariharan, C. Photocatalytic degradation of organic contaminants in water by ZnO nanoparticles: Revisited. *Applied Catalysis A: General* **2006**, *304*, 55-61.
(8) Aslam, U.; Rao, V. G.; Chavez, S.; Linic, S. Catalytic conversion of solar to chemical energy on plasmonic metal nanostructures. *Nature Catalysis* **2018**, *1* (9), 656-665.
(9) Christopher, P.; Xin, H.; Linic, S. Visible-light-enhanced catalytic oxidation reactions on plasmonic silver nanostructures. *Nature Chemistry* **2011**, *3* (6), 467-472.
(10) Peiris, E.; Hanauer, S.; Le, T.; Wang, J.; Salavati-fard, T.; Brasseur, P.; Formo, E. V.; Wang, B.; Camargo, P. H. C. Controlling Selectivity in Plasmonic Catalysis: Switching Reaction Pathway from Hydrogenation to Homocoupling Under Visible-Light Irradiation. *Angewandte Chemie International Edition* **2022**, *n/a* (n/a), e202216398, https://doi.org/10.1002/anie.202216398. (acccessed 2022/12/28).
(11) Salavati-fard, T.; Wang, B. Plasmon-Assisted Direct Interfacial Charge Transfer Enables Molecular Photodissociation on Metal Surfaces. *ACS Catalysis* **2022**, *12* (20), 12869-12878.
(12) Gavnholt, J.; Olsen, T.; Engelund, M.; Schiøtz, J. Δ self-consistent field method to obtain potential energy surfaces of excited molecules on surfaces. *Physical Review B* **2008**, *78* (7), 075441.
(13) Olsen, T.; Gavnholt, J.; Schiøtz, J. Hot-electron-mediated desorption rates calculated from excited-state potential energy surfaces. *Physical Review B* **2009**, *79* (3), 035403.
(14) Kresse, G.; Furthmüller, J. Efficient iterative schemes for ab initio total-energy calculations using a plane-wave basis set. *Physical review B* **1996**, *54* (16), 11169.
(15) Mortensen, J. J.; Hansen, L. B.; Jacobsen, K. W. Real-space grid implementation of the projector augmented wave method. *Physical review B* **2005**, *71* (3), 035109.
(16) Enkovaara, J.; Rostgaard, C.; Mortensen, J. J.; Chen, J.; Dułak, M.; Ferrighi, L.; Gavnholt, J.; Glinsvad, C.; Haikola, V.; Hansen, H. Electronic structure calculations with GPAW: a real-space implementation of the projector augmented-wave method. *Journal of physics: Condensed matter* **2010**, *22* (25), 253202.
(17) Kale, M. J.; Avanesian, T.; Xin, H.; Yan, J.; Christopher, P. Controlling catalytic selectivity on metal nanoparticles by direct photoexcitation of adsorbate–metal bonds. *Nano letters* **2014**, *14* (9), 5405-5412.

(18) Mukherjee, S.; Libisch, F.; Large, N.; Neumann, O.; Brown, L. V.; Cheng, J.; Lassiter, J. B.; Carter, E. A.; Nordlander, P.; Halas, N. J. Hot Electrons Do the Impossible: Plasmon-Induced Dissociation of H2 on Au. *Nano Letters* **2013**, *13* (1), 240-247.
(19) Zhou, L.; Martirez, J. M. P.; Finzel, J.; Zhang, C.; Swearer, D. F.; Tian, S.; Robatjazi, H.; Lou, M.; Dong, L.; Henderson, L.; et al. Light-driven methane dry reforming with single atomic site antenna-reactor plasmonic photocatalysts. *Nature Energy* **2020**, *5* (1), 61-70.
(20) Quiroz, J.; Barbosa, E. C. M.; Araujo, T. P.; Fiorio, J. L.; Wang, Y.-C.; Zou, Y.-C.; Mou, T.; Alves, T. V.; de Oliveira, D. C.; Wang, B. Controlling reaction selectivity over hybrid plasmonic nanocatalysts. *Nano letters* **2018**, *18* (11), 7289-7297.
(21) Marimuthu, A.; Zhang, J.; Linic, S. Tuning selectivity in propylene epoxidation by plasmon mediated photo-switching of Cu oxidation state. *Science* **2013**, *339* (6127), 1590-1593.
(22) Robatjazi, H.; Zhao, H.; Swearer, D. F.; Hogan, N. J.; Zhou, L.; Alabastri, A.; McClain, M. J.; Nordlander, P.; Halas, N. J. Plasmon-induced selective carbon dioxide conversion on earth-abundant aluminum-cuprous oxide antenna-reactor nanoparticles. *Nature Communications* **2017**, *8* (1), 27.
(23) Linic, S.; Aslam, U.; Boerigter, C.; Morabito, M. Photochemical transformations on plasmonic metal nanoparticles (vol 14, pg 567, 2015). *Nature Materials* **2015**, *14* (7), 744-744.
(24) Wilson, A. J.; Mohan, V.; Jain, P. K. Mechanistic Understanding of Plasmon-Enhanced Electrochemistry. *J Phys Chem C* **2019**, *123* (48), 29360-29369.
(25) Resasco, D. E.; Wang, B.; Sabatini, D. Distributed processes for biomass conversion could aid UN Sustainable Development Goals. *Nature Catalysis* **2018**, *1* (10), 731-735.
(26) Barbosa, E. C. M.; Fiorio, J. L.; Mou, T.; Wang, B.; Rossi, L. M.; Camargo, P. H. C. Reaction Pathway Dependence in Plasmonic Catalysis: Hydrogenation as a Model Molecular Transformation. *Chem-Eur J* **2018**, *24* (47), 12330-12339.
(27) Cortés, E.; Xie, W.; Cambiasso, J.; Jermyn, A. S.; Sundararaman, R.; Narang, P.; Schlücker, S.; Maier, S. A. Plasmonic hot electron transport drives nano-localized chemistry. *Nature communications* **2017**, *8* (1), 1-10.
(28) Kumari, G.; Zhang, X. Q.; Devasia, D.; Heo, J.; Jain, P. K. Watching Visible Light-Driven CO2 Reduction on a Plasmonic Nanoparticle Catalyst. *Acs Nano* **2018**, *12* (8), 8330-8340.
(29) Therrien, A. J.; Kale, M. J.; Yuan, L.; Zhang, C.; Halas, N. J.; Christopher, P. Impact of chemical interface damping on surface plasmon dephasing. *Faraday Discussions* **2019**, *214* (0), 59-72, 10.1039/C8FD00151K.
(30) Chavez, S.; Rao, V. G.; Linic, S. Unearthing the factors governing site specific rates of electronic excitations in multicomponent plasmonic systems and catalysts. *Faraday Discussions* **2019**, *214*, 441-453.
(31) Aslam, U.; Chavez, S.; Linic, S. Controlling energy flow in multimetallic nanostructures for plasmonic catalysis. *Nature Nanotechnology* **2017**, *12* (10), 1000-1005.
(32) Swearer, D. F.; Zhao, H. Q.; Zhou, L. N.; Zhang, C.; Robatjazi, H.; Martirez, J. M. P.; Krauter, C. M.; Yazdi, S.; McClain, M. J.; Ringe, E.; et al. Heterometallic antenna-reactor complexes for photocatalysis. *P Natl Acad Sci USA* **2016**, *113* (32), 8916-8920.
(33) Wang, J.; Heo, J.; Chen, C. Q.; Wilson, A. J.; Jain, P. K. Ammonia Oxidation Enhanced by Photopotential Generated by Plasmonic Excitation of a Bimetallic Electrocatalyst. *Angew Chem Int Edit* **2020**, *59* (42), 18430-18434.
(34) Martirez, J. M. P.; Carter, E. A. Excited-State N2 Dissociation Pathway on Fe-Functionalized Au. *Journal of the American Chemical Society* **2017**, *139* (12), 4390-4398.

(35) Martirez, J. M. P.; Carter, E. A. Prediction of a low-temperature N₂ dissociation catalyst exploiting near-IR–to–visible light nanoplasmonics. *Science Advances* **2017**, *3* (12), eaao4710.
(36) Zhou, L.; Swearer, D. F.; Zhang, C.; Robatjazi, H.; Zhao, H.; Henderson, L.; Dong, L.; Christopher, P.; Carter, E. A.; Nordlander, P. Quantifying hot carrier and thermal contributions in plasmonic photocatalysis. *Science* **2018**, *362* (6410), 69-72.
(37) Spata, V. A.; Carter, E. A. Mechanistic Insights into Photocatalyzed Hydrogen Desorption from Palladium Surfaces Assisted by Localized Surface Plasmon Resonances. *Acs Nano* **2018**, *12* (4), 3512-3522.
(38) Mishra, A. K.; de Leeuw, N. H. Mechanistic insights into the Cu(I) oxide-catalyzed conversion of CO2 to fuels and chemicals: A DFT approach. *Journal of CO2 Utilization* **2016**, *15*, 96-106.
(39) Perdew, J. P.; Burke, K.; Ernzerhof, M. Generalized gradient approximation made simple. *Physical review letters* **1996**, *77* (18), 3865.
(40) Dudarev, S. L.; Botton, G. A.; Savrasov, S. Y.; Humphreys, C.; Sutton, A. P. Electron-energy-loss spectra and the structural stability of nickel oxide: An LSDA+ U study. *Physical Review B* **1998**, *57* (3), 1505.
(41) Grimme, S.; Ehrlich, S.; Goerigk, L. Effect of the damping function in dispersion corrected density functional theory. *Journal of computational chemistry* **2011**, *32* (7), 1456-1465.
(42) Bendavid, L. I.; Carter, E. A. First-Principles Predictions of the Structure, Stability, and Photocatalytic Potential of Cu2O Surfaces. *The Journal of Physical Chemistry B* **2013**, *117* (49), 15750-15760.
(43) Bendavid, L. I.; Carter, E. A. CO2 Adsorption on Cu2O(111): A DFT+U and DFT-D Study. *The Journal of Physical Chemistry C* **2013**, *117* (49), 26048-26059.
(44) Isseroff, L. Y.; Carter, E. A. Importance of reference Hamiltonians containing exact exchange for accurate one-shot GW calculations of Cu${}_{2}$O. *Physical Review B* **2012**, *85* (23), 235142.
(45) Henkelman, G.; Uberuaga, B. P.; Jónsson, H. A climbing image nudged elastic band method for finding saddle points and minimum energy paths. *The Journal of Chemical Physics* **2000**, *113* (22), 9901-9904. (acccessed 2020/07/20).
(46) Heyden, A.; Bell, A. T.; Keil, F. J. Efficient methods for finding transition states in chemical reactions: Comparison of improved dimer method and partitioned rational function optimization method. *The Journal of Chemical Physics* **2005**, *123* (22), 224101. (acccessed 2020/07/20).
(47) Cohen, A. J.; Mori-Sánchez, P.; Yang, W. Insights into Current Limitations of Density Functional Theory. *Science* **2008**, *321* (5890), 792.
(48) Gumidyala, A.; Wang, B.; Crossley, S. Direct carbon-carbon coupling of furanics with acetic acid over Bronsted zeolites. *Science Advances* **2016**, *2* (9), e160107.
(49) Hellman, A.; Razaznejad, B.; Lundqvist, B. I. Potential-energy surfaces for excited states in extended systems. *The Journal of chemical physics* **2004**, *120* (10), 4593-4602.
(50) Jones, R. O.; Gunnarsson, O. The density functional formalism, its applications and prospects. *Reviews of Modern Physics* **1989**, *61* (3), 689.
(51) Tang, W.; Sanville, E.; Henkelman, G. A grid-based Bader analysis algorithm without lattice bias. *Journal of Physics: Condensed Matter* **2009**, *21* (8), 084204.
(52) Mishra, A. K.; Roldan, A.; de Leeuw, N. H. A density functional theory study of the adsorption behaviour of CO2 on Cu2O surfaces. *The Journal of Chemical Physics* **2016**, *145* (4), 044709.

(53) Peng, C.; Reid, G.; Wang, H.; Hu, P. Perspective: Photocatalytic reduction of CO2 to solar fuels over semiconductors. *The Journal of Chemical Physics* **2017**, *147* (3), 030901.
(54) Bao, J. L.; Carter, E. A. Surface-Plasmon-Induced Ammonia Decomposition on Copper: Excited-State Reaction Pathways Revealed by Embedded Correlated Wavefunction Theory. *Acs Nano* **2019**, *13* (9), 9944-9957.
(55) Li, J.; Cushing, S. K.; Meng, F.; Senty, T. R.; Bristow, A. D.; Wu, N. Plasmon-induced resonance energy transfer for solar energy conversion. *Nature Photonics* **2015**, *9* (9), 601-607.
(56) Eastment, R.; Mee, C. Work function measurements on (100),(110) and (111) surfaces of aluminium. *Journal of Physics F: Metal Physics* **1973**, *3* (9), 1738.
(57) Kramm, B.; Laufer, A.; Reppin, D.; Kronenberger, A.; Hering, P.; Polity, A.; Meyer, B. The band alignment of Cu2O/ZnO and Cu2O/GaN heterostructures. *Applied Physics Letters* **2012**, *100* (9), 094102.
(58) Sachtler, W.; Dorgelo, G.; Holscher, A. The work function of gold. *Surface Science* **1966**, *5* (2), 221-229.
(59) Chelvayohan, M.; Mee, C. Work function measurements on (110),(100) and (111) surfaces of silver. *Journal of Physics C: Solid State Physics* **1982**, *15* (10), 2305.
(60) He, J.; Janáky, C. Recent advances in solar-driven carbon dioxide conversion: expectations versus reality. *ACS energy letters* **2020**, *5* (6), 1996-2014.
(61) Li, X.; Yu, J.; Jaroniec, M.; Chen, X. Cocatalysts for selective photoreduction of CO2 into solar fuels. *Chemical reviews* **2019**, *119* (6), 3962-4179.
(62) Ramakrishnan, S. B.; Mohammadparast, F.; Dadgar, A. P.; Mou, T.; Le, T.; Wang, B.; Jain, P. K.; Andiappan, M. Photoinduced Electron and Energy Transfer Pathways and Photocatalytic Mechanisms in Hybrid Plasmonic Photocatalysis. *Advanced Optical Materials* **2021**, *9* (22), 2101128.
(63) Wu, J.; Huang, Y.; Ye, W.; Li, Y. CO2 reduction: from the electrochemical to photochemical approach. *Advanced Science* **2017**, *4* (11), 1700194.
(64) Loh, J. Y.; Kherani, N. P.; Ozin, G. A. Persistent CO2 photocatalysis for solar fuels in the dark. *Nature Sustainability* **2021**, *4* (6), 466-473.
(65) Rej, S.; Bisetto, M.; Naldoni, A.; Fornasiero, P. Well-defined Cu2O photocatalysts for solar fuels and chemicals. *Journal of Materials Chemistry A* **2021**, *9* (10), 5915-5951, 10.1039/D0TA10181H.
(66) Jia, H.; Li, F.; Chow, T. H.; Liu, X.; Zhang, H.; Lu, Y.; Wang, J.; Zhang, C.-y. Construction of Spatially Separated Gold Nanocrystal/Cuprous Oxide Architecture for Plasmon-Driven CO2 Reduction. *Nano Letters* **2022**, *22* (17), 7268-7274.
(67) Zhang, F.; Li, Y.-H.; Qi, M.-Y.; Tang, Z.-R.; Xu, Y.-J. Boosting the activity and stability of Ag-Cu2O/ZnO nanorods for photocatalytic CO2 reduction. *Applied Catalysis B: Environmental* **2020**, *268*, 118380.
(68) Zhou, C.; Wang, S.; Zhao, Z.; Shi, Z.; Yan, S.; Zou, Z. A Facet-Dependent Schottky-Junction Electron Shuttle in a BiVO4 {010}–Au–Cu2O Z-Scheme Photocatalyst for Efficient Charge Separation. *Advanced Functional Materials* **2018**, *28* (31), 1801214.
(69) Xiong, Z.; Lei, Z.; Kuang, C.-C.; Chen, X.; Gong, B.; Zhao, Y.; Zhang, J.; Zheng, C.; Wu, J. C. Selective photocatalytic reduction of CO2 into CH4 over Pt-Cu2O TiO2 nanocrystals: The interaction between Pt and Cu2O cocatalysts. *Applied Catalysis B: Environmental* **2017**, *202*, 695-703.

(70) Wang, H.; Rong, H.; Wang, D.; Li, X.; Zhang, E.; Wan, X.; Bai, B.; Xu, M.; Liu, J.; Liu, J. Highly selective photoreduction of CO2 with suppressing H2 evolution by plasmonic Au/CdSe–Cu2O hierarchical nanostructures under visible light. *Small* **2020**, *16* (18), 2000426.
(71) Wang, W.; Deng, C.; Xie, S.; Li, Y.; Zhang, W.; Sheng, H.; Chen, C.; Zhao, J. Photocatalytic c–c coupling from carbon dioxide reduction on copper oxide with mixed-valence copper (I)/copper (II). *Journal of the American Chemical Society* **2021**, *143* (7), 2984-2993.
(72) Zhai, Q.; Xie, S.; Fan, W.; Zhang, Q.; Wang, Y.; Deng, W.; Wang, Y. Photocatalytic conversion of carbon dioxide with water into methane: platinum and copper (I) oxide co-catalysts with a core–shell structure. *Angewandte Chemie* **2013**, *125* (22), 5888-5891.
(73) Wan, L.; Zhou, Q.; Wang, X.; Wood, T. E.; Wang, L.; Duchesne, P. N.; Guo, J.; Yan, X.; Xia, M.; Li, Y. F. Cu2O nanocubes with mixed oxidation-state facets for (photo) catalytic hydrogenation of carbon dioxide. *Nature Catalysis* **2019**, *2* (10), 889-898.
(74) Wu, Y. A.; McNulty, I.; Liu, C.; Lau, K. C.; Liu, Q.; Paulikas, A. P.; Sun, C.-J.; Cai, Z.; Guest, J. R.; Ren, Y. Facet-dependent active sites of a single Cu2O particle photocatalyst for CO2 reduction to methanol. *Nature Energy* **2019**, *4* (11), 957-968.
(75) Le, T.; Shao, Y.; Wang, B. Plasmon-Induced CO2 Conversion on Al@ Cu2O: A DFT Study. *The Journal of Physical Chemistry C* **2021**, *125* (11), 6108-6115.
(76) Li, L.; Zhang, R.; Vinson, J.; Shirley, E. L.; Greeley, J. P.; Guest, J. R.; Chan, M. K. Imaging catalytic activation of CO2 on Cu2O (110): a first-principles study. *Chemistry of Materials* **2018**, *30* (6), 1912-1923.
(77) Huang, W.-C.; Lyu, L.-M.; Yang, Y.-C.; Huang, M. H. Synthesis of Cu2O nanocrystals from cubic to rhombic dodecahedral structures and their comparative photocatalytic activity. *Journal of the American Chemical Society* **2012**, *134* (2), 1261-1267.
(78) Celaya, C. A.; Delesma, C.; Torres-Arellano, S.; Sebastian, P.; Muñiz, J. Understanding CO2 conversion into hydrocarbons via a photoreductive process supported on the Cu2O (1 0 0),(1 1 0) and (1 1 1) surface facets: A first principles study. *Fuel* **2021**, *306*, 121643.
(79) Shen, M.; Zhang, L.; Shi, J. Defect engineering of photocatalysts towards elevated CO2 reduction performance. *ChemSusChem* **2021**, *14* (13), 2635-2654.
(80) Ji, Y.; Luo, Y. New mechanism for photocatalytic reduction of CO2 on the anatase TiO2 (101) surface: the essential role of oxygen vacancy. *Journal of the American Chemical Society* **2016**, *138* (49), 15896-15902.
(81) Wu, H.; Zhang, N.; Wang, H.; Hong, S. Adsorption of CO2 on Cu2O (1 1 1) oxygen-vacancy surface: First-principles study. *Chemical Physics Letters* **2013**, *568*, 84-89.
(82) Ricca, C.; Grad, L.; Hengsberger, M.; Osterwalder, J.; Aschauer, U. Importance of surface oxygen vacancies for ultrafast hot carrier relaxation and transport in Cu 2 O. *Physical review research* **2021**, *3* (4), 043219.
(83) Yu, X.; Zhang, X.; Wang, H.; Wang, Z.; Feng, G. High-coverage H2 adsorption on the reconstructed Cu2O (111) surface. *The Journal of Physical Chemistry C* **2017**, *121* (40), 22081-22091.
(84) Wang, H.; Cheng, S.; Cai, X.; Cheng, L.; Zhou, R.; Hou, T.; Li, Y. Photocatalytic CO2 reduction to HCOOH over core-shell Cu@ Cu2O catalysts. *Catalysis Communications* **2022**, *162*, 106372.
(85) Isseroff, L. Y.; Carter, E. A. Electronic structure of pure and doped cuprous oxide with copper vacancies: suppression of trap states. *Chemistry of Materials* **2013**, *25* (3), 253-265.

(86) Onsten, A.; Weissenrieder, J.; Stoltz, D.; Yu, S.; Göthelid, M.; Karlsson, U. O. Role of defects in surface chemistry on Cu2O (111). *The Journal of Physical Chemistry C* **2013**, *117* (38), 19357-19364.
(87) Le, T.; Wang, B. First-Principles Study of Interaction between Molecules and Lewis Acid Zeolites Manipulated by Injection of Energized Charge Carriers. *Industrial & Engineering Chemistry Research* **2021**, *60* (39), 14124-14133.
(88) Fox, M. Optical Properties of Solids: Oxford University Press. *New York* **2010**.
(89) Harris, J. W.; Bates, J. S.; Bukowski, B. C.; Greeley, J.; Gounder, R. Opportunities in Catalysis over Metal-Zeotypes Enabled by Descriptions of Active Centers Beyond Their Binding Site. *ACS Catalysis* **2020**, *10* (16), 9476-9495.
(90) Clatworthy, E. B.; Konnov, S. V.; Dubray, F.; Nesterenko, N.; Gilson, J. p.; Mintova, S. Emphasis on the properties of metal-containing zeolites operating outside the comfort zone of current heterogeneous catalytic reactions. *Angewandte Chemie* **2020**, *132* (44), 19582-19600.
(91) Peeters, E.; Pomalaza, G.; Khalil, I.; Detaille, A.; Debecker, D. P.; Douvalis, A. P.; Dusselier, M.; Sels, B. F. Highly Dispersed Sn-beta Zeolites as Active Catalysts for Baeyer–Villiger Oxidation: The Role of Mobile, In Situ Sn (II) O Species in Solid-State Stannation. *ACS Catalysis* **2021**, *11* (10), 5984-5998.
(92) Luo, H. Y.; Lewis, J. D.; Román-Leshkov, Y. Lewis acid zeolites for biomass conversion: Perspectives and challenges on reactivity, synthesis, and stability. *Annual review of chemical and biomolecular engineering* **2016**, *7*, 663-692.
(93) Ennaert, T.; Van Aelst, J.; Dijkmans, J.; De Clercq, R.; Schutyser, W.; Dusselier, M.; Verboekend, D.; Sels, B. F. Potential and challenges of zeolite chemistry in the catalytic conversion of biomass. *Chemical Society Reviews* **2016**, *45* (3), 584-611.
(94) Lewis, J. D.; Van de Vyver, S.; Román-Leshkov, Y. Acid–base pairs in Lewis acidic zeolites promote direct aldol reactions by soft enolization. *Angewandte Chemie* **2015**, *127* (34), 9973-9976.
(95) Román-Leshkov, Y.; Davis, M. E. Activation of carbonyl-containing molecules with solid Lewis acids in aqueous media. *Acs Catalysis* **2011**, *1* (11), 1566-1580.
(96) Resasco, D. E.; Wang, B.; Crossley, S. Zeolite-catalysed C–C bond forming reactions for biomass conversion to fuels and chemicals. *Catalysis Science & Technology* **2016**, *6* (8), 2543-2559.
(97) Ayla, E. Z.; Potts, D. S.; Bregante, D. T.; Flaherty, D. W. Alkene Epoxidations with H2O2 over Groups 4–6 Metal-Substituted BEA Zeolites: Reactive Intermediates, Reaction Pathways, and Linear Free-Energy Relationships. *ACS Catalysis* **2020**, *11*, 139-154.
(98) Medford, A. J.; Vojvodic, A.; Hummelshøj, J. S.; Voss, J.; Abild-Pedersen, F.; Studt, F.; Bligaard, T.; Nilsson, A.; Nørskov, J. K. From the Sabatier principle to a predictive theory of transition-metal heterogeneous catalysis. *Journal of Catalysis* **2015**, *328*, 36-42.
(99) Palagin, D.; Sushkevich, V. L.; Ivanova, I. I. C–C Coupling Catalyzed by Zeolites: Is Enolization the Only Possible Pathway for Aldol Condensation? *The Journal of Physical Chemistry C* **2016**, *120* (41), 23566-23575.
(100) Moliner, M.; Román-Leshkov, Y.; Davis, M. E. Tin-containing zeolites are highly active catalysts for the isomerization of glucose in water. *Proceedings of the National Academy of Sciences* **2010**, *107* (14), 6164-6168.
(101) Corma, A.; Nemeth, L. T.; Renz, M.; Valencia, S. Sn-zeolite beta as a heterogeneous chemoselective catalyst for Baeyer–Villiger oxidations. *Nature* **2001**, *412* (6845), 423-425.
(102) Boronat, M.; Corma, A.; Renz, M.; Viruela, P. M. Predicting the activity of single isolated Lewis acid sites in solid catalysts. *Chemistry–A European Journal* **2006**, *12* (27), 7067-7077.

(103) Shetty, S.; Kulkarni, B. S.; Kanhere, D. G.; Goursot, A.; Pal, S. A comparative study of structural, acidic and hydrophilic properties of Sn− BEA with Ti− BEA using periodic density functional theory. *The Journal of Physical Chemistry B* **2008**, *112* (9), 2573-2579.
(104) Gordon, C. P.; Engler, H.; Tragl, A. S.; Plodinec, M.; Lunkenbein, T.; Berkessel, A.; Teles, J. H.; Parvulescu, A.-N.; Copéret, C. Efficient epoxidation over dinuclear sites in titanium silicalite-1. *Nature* **2020**, *586* (7831), 708-713.
(105) Gunther, W. R.; Michaelis, V. K.; Griffin, R. G.; Román-Leshkov, Y. Interrogating the Lewis acidity of metal sites in beta zeolites with 15N pyridine adsorption coupled with MAS NMR spectroscopy. *The Journal of Physical Chemistry C* **2016**, *120* (50), 28533-28544.
(106) Bregante, D. T.; Flaherty, D. W. Periodic trends in olefin epoxidation over group IV and V framework-substituted zeolite catalysts: a kinetic and spectroscopic study. *Journal of the American Chemical Society* **2017**, *139* (20), 6888-6898.
(107) Mateo, D.; Cerrillo, J. L.; Durini, S.; Gascon, J. Fundamentals and applications of photo-thermal catalysis. *Chemical Society Reviews* **2021**, *50*, 2173-2210.
(108) Zhang, F.; Li, Y.-H.; Qi, M.-Y.; Yamada, Y. M.; Anpo, M.; Tang, Z.-R.; Xu, Y.-J. Photothermal catalytic CO2 reduction over nanomaterials. *Chem Catalysis* **2021**, *1* (2), 272-297.
(109) Dhiman, M. Plasmonic nanocatalysis for solar energy harvesting and sustainable chemistry. *Journal of Materials Chemistry A* **2020**, *8* (20), 10074-10095.
(110) Martirez, J. M. P.; Bao, J. L.; Carter, E. A. First-Principles Insights into Plasmon-Induced Catalysis. *Annual Review of Physical Chemistry* **2021**, *72*, 99-119.
(111) Ramakrishnan, S. B.; Tirumala, R. T. A.; Mohammadparast, F.; Mou, T.; Le, T.; Wang, B.; Andiappan, M. Plasmonic photocatalysis. In *Catalysis: Volume 33*, Vol. 33; The Royal Society of Chemistry, 2021; pp 38-86.
(112) Coutino-Gonzalez, E.; Roeffaers, M. B.; Dieu, B.; De Cremer, G.; Leyre, S.; Hanselaer, P.; Fyen, W.; Sels, B.; Hofkens, J. Determination and optimization of the luminescence external quantum efficiency of silver-clusters zeolite composites. *The Journal of Physical Chemistry C* **2013**, *117* (14), 6998-7004.
(113) Fenwick, O.; Coutiño-Gonzalez, E.; Grandjean, D.; Baekelant, W.; Richard, F.; Bonacchi, S.; De Vos, D.; Lievens, P.; Roeffaers, M.; Hofkens, J. Tuning the energetics and tailoring the optical properties of silver clusters confined in zeolites. *Nature materials* **2016**, *15* (9), 1017-1022.
(114) Grandjean, D.; Coutiño-Gonzalez, E.; Cuong, N. T.; Fron, E.; Baekelant, W.; Aghakhani, S.; Schlexer, P.; D'Acapito, F.; Banerjee, D.; Roeffaers, M. B. Origin of the bright photoluminescence of few-atom silver clusters confined in LTA zeolites. *Science* **2018**, *361* (6403), 686-690.
(115) Lee, W.-S.; Lai, L.-C.; Akatay, M. C.; Stach, E. A.; Ribeiro, F. H.; Delgass, W. N. Probing the gold active sites in Au/TS-1 for gas-phase epoxidation of propylene in the presence of hydrogen and oxygen. *Journal of catalysis* **2012**, *296*, 31-42.
(116) Huang, J.; Lima, E.; Akita, T.; Guzmán, A.; Qi, C.; Takei, T.; Haruta, M. Propene epoxidation with O2 and H2: identification of the most active gold clusters. *Journal of Catalysis* **2011**, *278* (1), 8-15.
(117) Alberti, A.; Cruciani, G.; Galli, E.; Millini, R.; Zanardi, S. In situ X-ray single-crystal study on the dehydration mechanism in the monoclinic polytype of Tschernichite, the mineral analog of zeolite beta. *The Journal of Physical Chemistry C* **2007**, *111* (12), 4503-4511.
(118) Yang, G.; Zhou, L.; Han, X. Lewis and Brönsted acidic sites in M4+-doped zeolites (M= Ti, Zr, Ge, Sn, Pb) as well as interactions with probe molecules: A DFT study. *Journal of Molecular Catalysis A: Chemical* **2012**, *363*, 371-379.

(119) Yang, G.; Pidko, E. A.; Hensen, E. J. Structure, stability, and Lewis acidity of mono and double Ti, Zr, and Sn framework substitutions in BEA zeolites: a periodic density functional theory study. *The Journal of Physical Chemistry C* **2013**, *117* (8), 3976-3986.
(120) Hattori, Y.; Meng, J.; Zheng, K.; Meier de Andrade, A.; Kullgren, J.; Broqvist, P.; Nordlander, P.; Sá, J. Phonon-Assisted Hot Carrier Generation in Plasmonic Semiconductor Systems. *Nano letters* **2021**, *21* (2), 1083-1089.
(121) Boronat, M.; Corma, A.; Renz, M. Mechanism of the Meerwein− Ponndorf− Verley− Oppenauer (MPVO) redox equilibrium on Sn− and Zr− beta zeolite catalysts. *The journal of physical chemistry B* **2006**, *110* (42), 21168-21174.
(122) Li, Y.-P.; Head-Gordon, M.; Bell, A. T. Analysis of the reaction mechanism and catalytic activity of metal-substituted beta zeolite for the isomerization of glucose to fructose. *Acs Catalysis* **2014**, *4* (5), 1537-1545.
(123) Li, G.; Pidko, E. A.; Hensen, E. J. Synergy between Lewis acid sites and hydroxyl groups for the isomerization of glucose to fructose over Sn-containing zeolites: a theoretical perspective. *Catalysis science & technology* **2014**, *4* (8), 2241-2250.
(124) Hendon, C. H.; Butler, K. T.; Ganose, A. M.; Román-Leshkov, Y.; Scanlon, D. O.; Ozin, G. A.; Walsh, A. Electroactive nanoporous metal oxides and chalcogenides by chemical design. *Chemistry of materials* **2017**, *29* (8), 3663-3670.
(125) Vega-Vila, J. C.; Harris, J. W.; Gounder, R. Controlled insertion of tin atoms into zeolite framework vacancies and consequences for glucose isomerization catalysis. *Journal of Catalysis* **2016**, *344*, 108-120.
(126) Seemala, B.; Therrien, A. J.; Lou, M.; Li, K.; Finzel, J. P.; Qi, J.; Nordlander, P.; Christopher, P. Plasmon-mediated catalytic O2 dissociation on Ag nanostructures: Hot electrons or near fields? *ACS Energy Letters* **2019**, *4* (8), 1803-1809.
(127) Wells Jr, D. H.; Delgass Jr, W. N.; Thomson, K. T. Evidence of defect-promoted reactivity for epoxidation of propylene in titanosilicate (TS-1) catalysts: a DFT study. *Journal of the American Chemical Society* **2004**, *126* (9), 2956-2962.
(128) Sayed, M.; Yu, J.; Liu, G.; Jaroniec, M. Non-noble plasmonic metal-based photocatalysts. *Chemical Reviews* **2022**, *122* (11), 10484-10537.
(129) Rice, K. P.; Walker Jr, E. J.; Stoykovich, M. P.; Saunders, A. E. Solvent-dependent surface plasmon response and oxidation of copper nanocrystals. *The Journal of Physical Chemistry C* **2011**, *115* (5), 1793-1799.
(130) Sanchez-Gonzalez, A.; Corni, S.; Mennucci, B. Surface-enhanced fluorescence within a metal nanoparticle array: the role of solvent and plasmon couplings. *The Journal of Physical Chemistry C* **2011**, *115* (13), 5450-5460.
(131) Nemykin, V. N.; Hadt, R. G.; Belosludov, R. V.; Mizuseki, H.; Kawazoe, Y. Influence of molecular geometry, exchange-correlation functional, and solvent effects in the modeling of vertical excitation energies in phthalocyanines using time-dependent density functional theory (TDDFT) and polarized continuum model TDDFT methods: can modern computational chemistry methods explain experimental controversies? *The Journal of Physical Chemistry A* **2007**, *111* (50), 12901-12913.
(132) Neugebauer, J.; Curutchet, C.; Munoz-Losa, A.; Mennucci, B. A subsystem TDDFT approach for solvent screening effects on excitation energy transfer couplings. *Journal of Chemical Theory and Computation* **2010**, *6* (6), 1843-1851.

(133) Moskowitz, J.; Sindi, R.; Geddes, C. D. Plasmonic Electricity II: The Effect of Particle Size, Solvent Permittivity, Applied Voltage, and Temperature on Fluorophore-Induced Plasmonic Current. *The Journal of Physical Chemistry C* **2020**, *124* (10), 5780-5788.
(134) Ghosh, S. K.; Nath, S.; Kundu, S.; Esumi, K.; Pal, T. Solvent and ligand effects on the localized surface plasmon resonance (LSPR) of gold colloids. *The Journal of Physical Chemistry B* **2004**, *108* (37), 13963-13971.
(135) Lee, S. W.; Kim, H.; Park, J. Y. How Hot Electron Generation at the Solid–Liquid Interface Is Different from the Solid–Gas Interface. *Nano Letters* **2023**.
(136) Bao, J. L.; Carter, E. A. Rationalizing the hot-carrier-mediated reaction mechanisms and kinetics for ammonia decomposition on ruthenium-doped copper nanoparticles. *Journal of the American Chemical Society* **2019**, *141* (34), 13320-13323.
(137) Yuan, Y.; Zhou, L.; Robatjazi, H.; Bao, J. L.; Zhou, J.; Bayles, A.; Yuan, L.; Lou, M.; Lou, M.; Khatiwada, S. Earth-abundant photocatalyst for H2 generation from NH3 with light-emitting diode illumination. *Science* **2022**, *378* (6622), 889-893.
(138) Deringer, V. L.; Tchougréeff, A. L.; Dronskowski, R. Crystal orbital Hamilton population (COHP) analysis as projected from plane-wave basis sets. *The journal of physical chemistry A* **2011**, *115* (21), 5461-5466.
(139) Fox, M. Optical properties of solids. American Association of Physics Teachers: 2002.